Title
Refining Constraints on Seismic Discontinuities and Elastic Structure in the Earth's Upper Mantle

Author
Zheng, Zhao

Publication Date
2014

Peer reviewed|Thesis/dissertation

Refining Constraints on Seismic Discontinuities and Elastic Structure in the Earth's Upper Mantle

by

Zhao Zheng

A dissertation submitted in partial satisfaction of the

requirement for the degree of

Doctor of Philosophy

in

Earth and Planetary Science

in the

Graduate Division

of the

University of California, Berkeley

Committee in charge:

Professor Barbara Romanowicz, Chair
Professor Douglas Dreger
Professor Michael Manga
Professor James Demmel

Spring 2014

Refining Constraints on Seismic Discontinuities and Elastic Structure in the Earth's Upper Mantle

by

Zhao Zheng

Abstract

Refining Constraints on Seismic Discontinuities and Elastic Structure in the Earth's Upper Mantle

by

Zhao Zheng

Doctor of Philosophy in Geophysics

University of California, Berkeley

Professor Barbara Romanowicz, Chair

We propose a modification to the Non-linear Asymptotic Coupling Theory (NACT), a normal mode coupling method used for synthesizing seismograms and computing sensitivity kernels in 3D Earth. The modification is aimed to meet the computational challenges for NACT when approaching higher frequencies, which is required for obtaining finer scale images of the Earth's upper mantle. The new scheme is numerically validated.

We present new constraints on the topography of the 410 and 660, two important seismic discontinuities in the Earth's upper mantle. The data used are the *SS* precursors recorded by the US Transportable Array. We first demonstrate a case of 3D mantle heterogeneity interplaying with discontinuity depth. We show observations from one event for which a large scale heterogeneity away from the *SS* precursor bounce point region produces an artificial "precursor". This new discovery raises a caution for identifying and interpreting *SS* (and perhaps *PP*) precursors.

We then present high resolution maps of 410 and 660 discontinuity topography across a large area of the Pacific Ocean, derived from *SS* precursors. A new filtering tool called the Local Slant-Stack Filtered (LSSF) is employed to successfully clean up the *SS* precursor record sections, leading to robust precursor travel time measurements with increased spatial resolution. Good agreements are observed between our discontinuity images and a very recent upper mantle tomography model *SEMum2*.

Besides the new constraints on the discontinuities, we also work on refining the elastic structure of the Earth's upper mantle in the context of regional/continental scale full-waveform tomography. We propose a framework for a hybrid adjoint tomography, in

which the gradient of the misfit function is numerically computed using the adjoint method with the highly accurate Regional Spectral Element Method (RegSEM) code, while the Hessian is computed approximately using NACT. We present results from tests on a dataset for imaging the North American continent.

Finally, we study the infra-gravity wave induced long-period noise on an ocean bottom broadband seismometer, MOBB, deployed offshore in the Monterey Bay, California, using ~10 years' continuous recording data. Strong correlation between the vertical component seismogram and the pressure record is observed. We define and calculate the transfer function between the two channels, and demonstrate that the transfer function is stable over time. We then utilize the average transfer function to remove pressure-correlated noise from the vertical component seismogram, and show that the cleaned MOBB waveforms help to better constrain the moment tensors for regional near-shore earthquakes on the San Andreas Fault system in Northern California.

Contents

List of Figures

List of Tables

Chapter 1

Introduction

The interior structure of our planet Earth is largely one-dimensional (1D), namely, the Earth's physical properties, such as seismic velocity and density, perhaps anisotropy and attenuation as well, are primarily a function of the Earth's radius. The physical meaning of this 1D dependence is that the medium is layered. This implies the composition and temperature of the Earth is largely 1D as well. The *Preliminary Reference Earth Model* (*PREM; Dziewonski* and *Anderson*, 1981), for example, even after more than two decades, still stands as a reasonably good reference 1D seismic model for our planet. On the other hand, it is well known that the interior of the Earth is convective, therefore deviating from 1D. One piece of direct evidence comes from the movement of tectonic plates at the surface of the Earth. In addition, seismic tomography, by making use of seismic waves penetrating into the interior of the Earth, has revealed the existence of subducting slabs (higher seismic velocity, suggesting they are colder and/or denser) and upwellings (lower seismic velocity, warmer) in the Earth's mantle, presenting compelling evidence for a convective mantle, meanwhile providing physical explanations for the surface tectonics observed. Mantle convection is not of surprise from the theoretical point of view, given the few thousand degree temperature contrast between the two thermal boundaries: the very hot core mantle boundary at the bottom (temperature constrained by the melting point of the liquid iron outer core), and the cool surface at the top. Geodynamicists have been able to construct analytical and numerical convection models that reproduce images that mimic what is seen by seismic tomography. These geodynamical models can be further played back in time to infer the history of our planet on geological time scales. The anchor point of geodynamics, however, has to be the present time snapshot of the Earth's interior provided by seismology.

In the past two decades, our understandings about the 3D structure of the Earth have greatly advanced, owing to improvement in the resolution of global mantle tomography. For instance, *SEMum2* (*French et al.*, 2013), a most recent generation shear velocity model, has shown capability of revealing 3D heterogeneities at the length scale of a few hundred kilometers in the upper mantle, which has important geodynamical implications. In addition to global tomography, our understanding about the Earth's interior can be refined in several other aspects. Here in this dissertation, we focus on two of these aspects. One of them has to do with imaging the upper mantle discontinuities, primarily

the “410” and the “660”. These are two globally present lateral discontinuities (abrupt jump in seismic wave speed and density with increasing depth), caused by phase transition of mantle minerals (primarily olivine) at approximate depths of 410 and 660 km, respectively, hence the names (Figure 1.1). They delineate the mantle transition zone, which separates the upper and lower mantle. Due to their phase transformation nature, they serve as proxies for the temperature and composition of the mantle. They are also of geodynamical significance, in that how material (down-going slabs and uprising plumes) transfer across these boundaries helps to determine whether the mantle convection is of whole-mantle scale or is layered (confined within the upper and lower mantle, respectively), or a combination of the two. The tomographic dataset has very poor constraints on these discontinuities; they are sensitive to the volumetric properties instead. Therefore, in this study, we collect a supplementary data type called the *SS* precursors (shear-shear wave reflected off these discontinuities; see Figure 1.2), which are suitable for the purpose of imaging the discontinuities (e.g. *Shearer*, 1991). We present high resolution images of the 410 and the 660 discontinuities measured from *SS* precursors, and discuss the geophysical and geodynamical implications. One challenge of the *SS* precursor study is the rapid increase of computational cost as one approaches higher frequency in the forward modeling of seismic waveforms and/or the computation of sensitivity kernels necessary for inversion. The shortest period of the *SS* precursor data is at 10~15 sec, which is much shorter than the current shortest period of data used for global tomography (e.g. 60 sec for constructing the *SEMum2* model). Therefore, part of this dissertation is devoted to exploring ways to improve the computational efficiency of the existing 3D forward modeling method.

The second aspect of refinement has to do with improving the resolution of seismic tomography in certain regions of the world, where enhanced coverage is made available by the deployment of denser regional seismic arrays. One such region is North America, where the US Transportable Array (TA) was deployed since 2004, resulting in ~1700 stations in total covering the entire conterminous U.S. on a nearly regular grid with an average station spacing of ~70 km. Such a dense array has allowed for unprecedented coverage in North America. In Berkeley, a series of studies (*Yuan* and *Romanowicz*, 2010; *Yuan et al.*, 2011; *Yuan et al.*, 2013) have been carried out utilizing waveform data from the TA and other available seismic stations to image the mantle beneath the North American continent and surrounding regions. Among these studies, the earlier ones are based on the Non-linear Asymptotic Coupling Theory (NACT; *Li* and *Romanowicz*, 1995; 1996), which is a semi-analytical method for 3D simulation based on normal mode coupling and asymptotic approximation theory. In the last study, the authors introduce RegSEM (Regional Spectral Element Method; *Cupillard et al.*, 2012), a fully numerical method, to improve the accuracy of the forward modeling part of the inverse problem. Here we take one more step forward. We present a framework of hybrid adjoint tomography, in which the gradient of the misfit function is computed fully numerically

using RegSEM, based on the adjoint method, while the (approximate) Hessian is still computed using NACT. We present preliminary test results using real earthquakes and stations from our North American tomography dataset.

In Chapter 2 of this dissertation, we explore ways to improve the computational efficiency of NACT, a 3D forward modeling tool based on normal mode coupling theory, in order to make it applicable to the higher frequency *SS* precursor study. The computational cost of NACT roughly increases as $(f_{max})^4$, where f_{max} is the maximum frequency (or the inverse of shortest period). This makes its application to forward modeling the *SS* precursors very challenging. Here we propose a modification to the mode coupling scheme in NACT, which reduces the frequency dependency to $(f_{max})^2$, and therefore meets the numerical challenge at higher frequencies. We present numerical tests to validate the new scheme.

Chapter 3 and 4 present observations of *SS* precursors. In Chapter 3, we discuss the "double 660 discontinuities" phenomenon observed in previous studies. In certain regions of the globe, in addition to the globally present 660-discontinuity, an additional deeper discontinuity at depths of ~720-800 km has been observed, which is often explained as local mineralogical complexity in the precursor bounce point region -- specifically the phase transformation in garnet, a minor mantle mineral besides the dominant olivine. Here we demonstrate a case of *SS* precursor observation, in which large-scale heterogeneities in the mantle away from the precursor bounce point region can generate an artificial "precursor" corresponding to an additional discontinuity in the above-mentioned depth range. This implies that caution must be taken when trying to interpret the "double discontinuity" observations in terms of complex mineralogy, which is a valuable piece of information for *SS* precursor studies in general. This work has been published in *Geophysical Journal International* under *Zheng* and *Romanowicz* (2012).

In Chapter 4, we present high resolution upper mantle discontinuity images across a large area of the Pacific Ocean, derived from an *SS* precursor dataset recorded by the US Transportable Array. In order to improve the spatial resolution, we apply a new processing tool called the Local Slant-Stack Filters (LSSF) to clean up the *SS* precursor record sections, which yields robust precursor travel time measurements on much finer scales than previous studies. We present images of 410 and 660 discontinuity topography and mantle transition zone thickness for the study region, and discuss their geophysical and geodynamical implications. We also discuss the connections observed between a few fine-scale anomalies in our discontinuity images and the volumetric heterogeneities observed by tomography.

In Chapter 5, we switch gears to regional tomography for North America. We present the theoretical framework for a hybrid adjoint tomography, and present preliminary test

results using real earthquakes and stations in the current North American tomography dataset.

Chapter 6 is a stand-alone study on the long-period noise reduction for MOBB, a broadband ocean-bottom seismometer deployed offshore of North California, and its application to improve moment tensor inversion for regional earthquakes on the San Andreas Fault system. This work has been published in *Bulletin of Seismological Society of America* under *Taira*, *Zheng* and *Romanowicz* (2014).

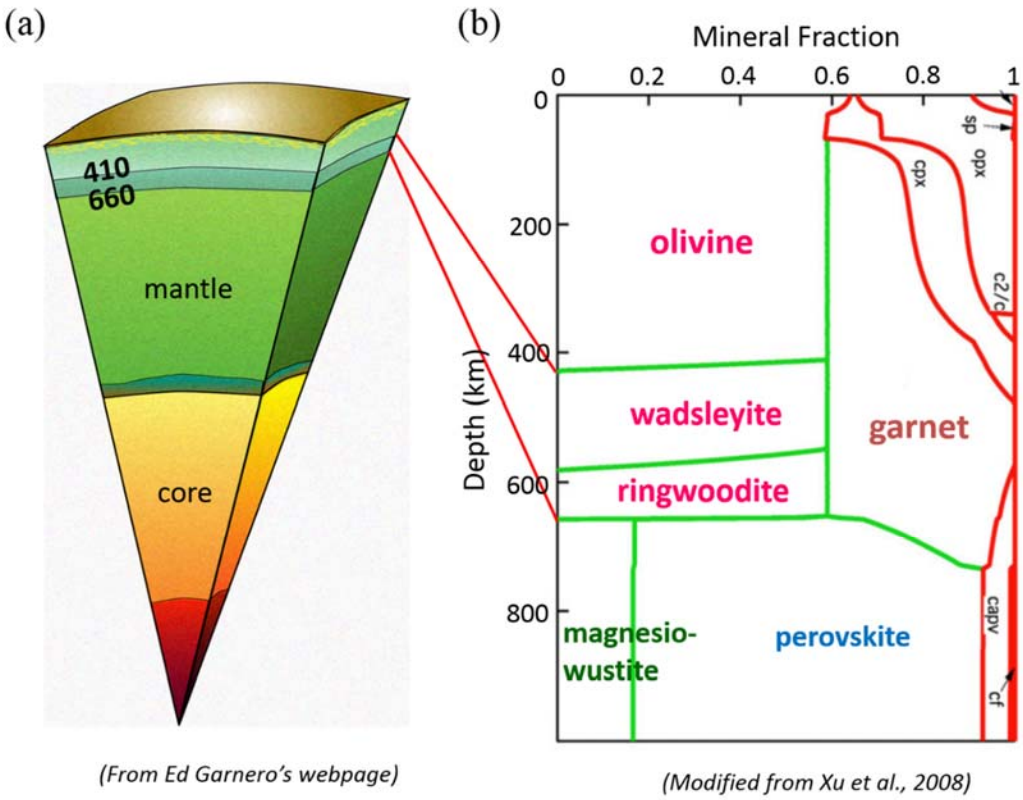

Figure 1.1. (a) The 410 and 660 discontinuities are globally present in the Earth's mantle. They delineate the mantle transition zone, which separates the upper and lower mantle. (b) Phase diagram of mantle minerals. The 410 and 660 are generally agreed to be caused by phase transformations of olivine.

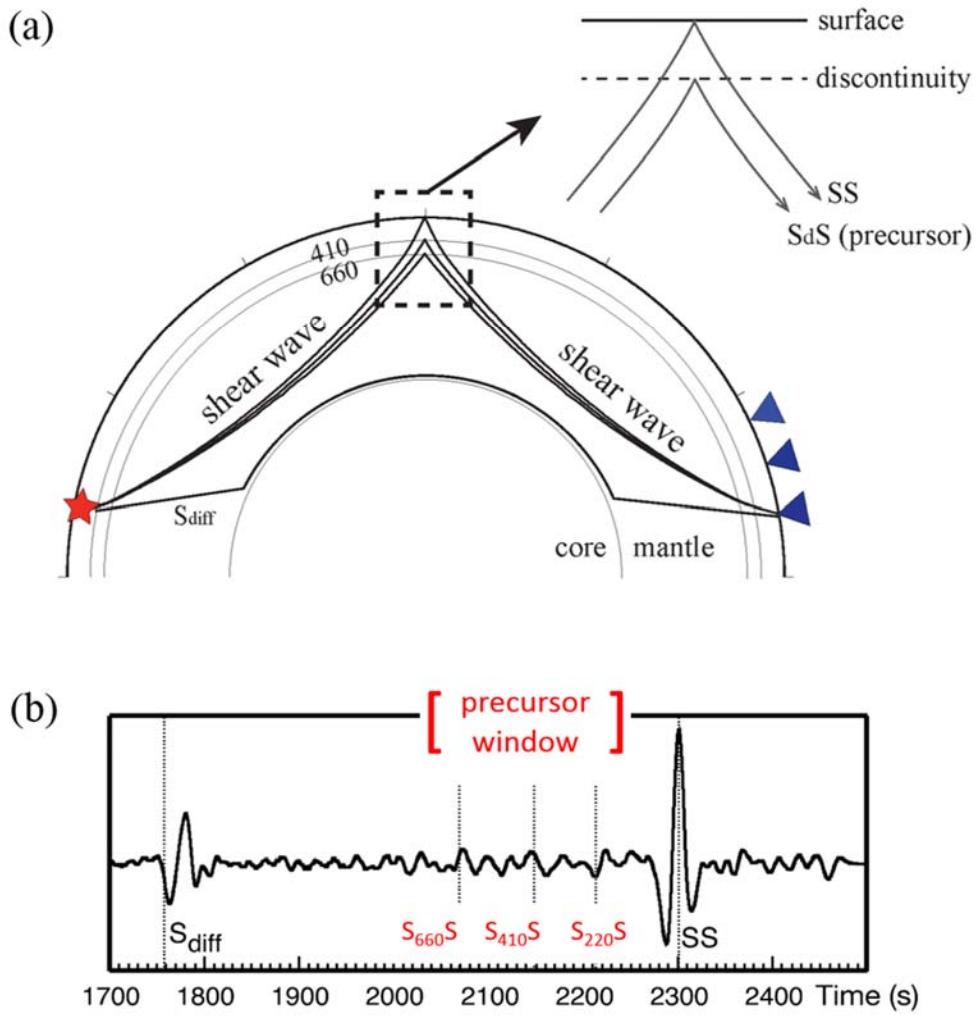

Figure 1.2. (a) The ray paths of SS precursors. An SS precursor is a seismic wave reflected off the bottom side of an upper mantle discontinuity (e.g. 410, or 660) at the midpoint between the seismic source (red star) and the receiver (blue triangles). (b) A typical transverse component seismogram containing the SS main phase and the precursors.

Chapter 2

Efficient Computation of 3D Synthetic Seismograms at Higher Frequencies Based on NACT

2.1 Introduction

The Berkeley Global Seismology group has developed several generations of global mantle tomographic models (*Li* and *Romanowicz*, 1996; *Megnin* and *Romanowicz*, 2000; *Panning* and *Romanowicz*, 2006; *Lekic* and *Romanowicz*, 2011; *French et al.*, 2013) by inverting a gradually expanding (both in terms of quantity and frequency content) dataset of surface and body waveforms. A normal mode coupling method known as the Non-linear Asymptotic Coupling Theory (NACT; *Li* and *Romanowicz*, 1995) has been used for computing 3D synthetic seismograms (except in *Lekic* and *Romanowicz*, 2011 and *French et al.*, 2013) and sensitivity kernels, which are two essential pieces for the inversion problem. NACT is an approximate approach which collapses sensitivity over the whole volume onto the vertical plane containing source and receiver. By taking into account the depth variation of sensitivity, NACT is able to bring out the ray character of body waves as well as the finite-frequency behavior of sensitivity kernels, therefore it is much better than 1D kernels based on the Path Average Approximation (PAVA; *Woodhouse* and *Dziewonski*, 1984) which is only valid for surface waves and not for body waves. On the other hand, as an approximate approach, NACT is computationally much faster than purely numerical methods such as the Spectral Element Method (SEM; *Komatitsch* and *Tromp*, 2002a,b). These merits make NACT a successful tool for handling a large inverse problem such as the global waveform tomography.

However, the NACT method is numerically challenged as we approach higher frequencies to forward model the waveforms of *SS* precursors, the shortest period of which is at 10~15 sec, much shorter than the data used for global tomography (e.g. 60 sec for constructing the *SEMum2* model). In the past, most SS precursor studies have been measuring the travel times of the precursors and translating that to discontinuity depth. To further constrain the sharpness of the discontinuity, the velocity gradients above and

below, and other detailed features, one has to use 3D waveform information of the precursors (e.g. *Cammarano et al.*, 2009). Computing SS precursor waveforms is challenging for the NACT method, which roughly increases as $(f_{max})^4$, determined by the normal mode coupling scheme, where f_{max} is the maximum cutoff frequency. Here we propose a modification to mode coupling scheme, which reduces the frequency scaling to $(f_{max})^2$, therefore meets the numerical challenge at higher frequencies.

2.2 A brief review of NACT

Here we give a brief summary of how NACT uses normal mode coupling to compute synthetic seismograms for a 3D Earth model. For more details, the readers are referred to *Li* and *Tanimoto* (1993), *Li* and *Romanowicz* (1995) and *Romanowicz et al.* (2008).

2.2.1 Theoretical framework

In normal mode theory, any seismic wavefield in a 1D spherical reference Earth can be expressed as a summation over the Earth's normal modes. For a 3D Earth model that slightly deviates from the 1D reference, the perturbed wavefield can be expressed as a double summation over mode pairs coupled due to the heterogeneity.

In *Li* and *Tanimoto* (1993), a work preceding the NACT formalism proposed by *Li* and *Romanowicz* (1995), the perturbed seismic wavefield in a heterogeneous Earth model is expressed as:

$$u(t) = u_0(t) + u_1(t) \tag{2.1}$$

The first term

$$u_0(t) = \sum_k A_k \exp(i\omega_k t) \tag{2.2}$$

is the unperturbed wavefield in the spherically symmetric reference Earth expressed as a superposition of normal modes. Here $k = (n, l)$ is the index of normal mode expressed in terms of spherical harmonics, where n is the radial order and l the angular order; ω_k is the angular eigen-frequency of mode k, and A_k is the excitation amplitude of that mode. In practice the summation over modes is truncated at some highest cutoff frequency $f_{\max}$. One basic fact is that for a given $f_{\max}$, the number of modes with eigen-frequencies below $f_{\max}$ is roughly proportional to $f_{\max}^2$, because both indices n and l roughly scale with $f_{\max}$ (Figure 2.1).

The second term on the right-hand side of Eq. (2.1) is

$$u_1(t) = \sum_k \sum_{k'} A_{kk'} \frac{\exp(i\omega_k t) - \exp(i\omega_{k'} t)}{{\omega_k}^2 - {\omega_{k'}}^2} \tag{2.3}$$

which is the wavefield perturbation due to heterogeneity, through a double summation of the couplings between mode pair *k* and *k'*. The coupling amplitude (or coupling strength) $A_{kk'}$ is:

$$A_{kk'} = \sum_m \sum_{m'} R_k^m H_{kk'}^{mm'} S_{k'}^{m'} \tag{2.4}$$

where $S_{k'}^{m'}$ and R_k^m (*m* being the azimuthal order of spherical harmonics) are the so called source and receiver terms as defined in *Woodhouse* and *Girnius* (1982), and the coupling matrix $H_{kk'}$ is linearly related to the heterogeneity (here only considering a perturbation in the elastic tensor, $\delta\boldsymbol{C}$ is considered; similar formulae exist for other types of heterogeneity, such as a density anomaly $\delta\rho$) through a 3D integral over the entire Earth volume:

$$H_{kk'}^{mm'} = \int_V \boldsymbol{\varepsilon}_k^{m*}(\boldsymbol{r}; \boldsymbol{r}_R) : \delta\boldsymbol{C}(\boldsymbol{r}) : \boldsymbol{\varepsilon}_{k'}^{m'}(\boldsymbol{r}; \boldsymbol{r}_S)\, dV \tag{2.5}$$

where $\boldsymbol{\varepsilon}_k^m$ is the strain of mode (*k*, *m*); $\boldsymbol{r}_S$ and $\boldsymbol{r}_R$ and $\boldsymbol{r}$ are the locations of seismic source, receiver and scatterer, respectively; "*" denotes complex conjugate, and "**:**" double dot product.

The physical meaning of Eq. (2.3)-(2.5) is very clear. The perturbation to the wavefield due to a single heterogeneity scatterer is a convolution of three terms: a propagation term from the source to the scatterer, a coupling term at the scatterer, and a propagation term from the scatterer to the receiver (Figure 2.2). The contributions from all scatterers are then integrated to obtain the total perturbation, assuming linearity. This is therefore a single forward scattering approximation (a.k.a. the Born approximation), and it is linear.

In *Li* and *Tanimoto* (1993), the asymptotic approximation for spherical harmonics is then applied to collapse the 3D integral over the volume unto a 2D integral in the great circle plane containing the seismic source and the receiver (Figure 2.2), in order to reduce the cost of computing $A_{kk'}$. The asymptotic approximation is valid for large *l* (the angular order of spherical harmonics), or in other words for higher frequencies. Its physical

meaning is that at higher frequencies, the sensitivity kernel is narrowed to the vicinity of the great circle plane.

Li and *Romanowicz* (1995) proposed an improvement to the linear formula in *Li* and *Tanimoto* (1993). The terms u_0 and u_1 in Eq. (2.1) are replaced by:

$$u_0(t) = \sum_k A_k \exp(i\widehat{\omega}_k t) \tag{2.6}$$

and

$$u_1(t) = -\sum_k it\delta\omega_k A_k \exp(i\widehat{\omega}_k t) + \sum_k \sum_{k' \in \Gamma_k} E_{kk'} \frac{\exp(i\widehat{\omega}_k t) - \exp(i\widehat{\omega}_{k'} t)}{(\omega_k + \omega_{k'})(\widehat{\omega}_k - \widehat{\omega}_{k'})} \tag{2.7}$$

with

$$\widehat{\omega}_k = \omega_k + \delta\omega_k \tag{2.8}$$

being a perturbed mode eigen-frequency due to heterogeneity, Γ_k being the set of modes whose eigen-frequencies are higher than or equal to ω_k, and $E_{kk'}$ the coupling amplitude of similar expression as the $A_{kk'}$ in Eq. (2.3).

The new recipe (Eq. (2.6) and (2.7)) resembles the old recipe (Eq. (2.2) and (2.3)) in the appearance, but they differ in several aspects. Most importantly, the new recipe is non-linear and includes multiple forward scattering. In the old recipe, heterogeneity only affects (linearly) the coupling amplitude, but not the phase of the seismogram. This is physically unrealistic, for example, in the case where an elongated velocity anomaly aligns with the seismic ray path between the source and the receiver (*Romanowicz et al.*, 2008). In this case, as the wave propagates along the anomaly, the phase shift will accumulate, and a finite amount of phase delay (or advance) will be observed at the receiver. For such cases, the new recipe performs much better by introducing the shifted eigen-frequency $\widehat{\omega}_k$ to replace ω_k. In the new recipe, the wavefield perturbation depends non-linearly on model perturbation, hence the name Non-linear Asymptotic Coupling Theory (NACT).

Li and *Romanowicz* (1995; 1996) pointed out the relation between NACT and the Path Average Approximation (PAVA; *Woodhouse* and *Dziewonski*, 1984) which was widely used for global waveform tomography before NACT was developed. PAVA only contains 1D sensitivity along the great circle path connecting the seismic source and receiver (Figure 2.3, left panels), and is valid for surface waves but not body waves. From the perspective of normal mode coupling, PAVA is equivalent to considering only the "along-branch" (namely, only modes with the same radial order n; see Figure 2.1 for the mode branches) coupling terms. In contrast, NACT includes the PAVA term as well as the "across-branch" coupling terms, therefore it provides 2D sensitivity that features body waves (Figure 2.3, right panels), making it a powerful tool for global mantle tomography.

2.2.2 The computational cost of NACT

In NACT, the computational cost for synthesizing one seismogram is dominated by the double summation over coupling mode pairs (Eq. (2.3), or the second term in Eq. (2.7)). In reality, the summation is truncated at some cutoff frequency f_{max}. Since the number of modes with eigen-frequencies below a certain cutoff frequency is roughly proportional to f_{max}^2 (see Figure 2.1), the number of mode pairs scales as f_{max}^4, and so does the cost of computing one seismogram. In the case of multiple sources and receivers, the cost scales as $(N_S * N_R) * f_{max}^4$, where N_S and N_S are the number of sources and receivers, respectively.

In the practice of NACT, the across-branch coupling is restricted to some maximum coupling width s_{max} such that $|l' - l| \leq s_{max}$, where l is the angular order of modes. If s_{max} is fixed, then the computational cost of the double summation scales as f_{max}^3 instead of f_{max}^4. The coupling width s_{max} is a measure of the scale of heterogeneity in the model. In reality s_{max} increases with f_{max}, but not proportionally, so the computational cost of the NACT lies somewhere between f_{max}^3 and f_{max}^4.

2.3 A modified NACT scheme

Now we present a modification to the mode coupling scheme of NACT, inspired by the idea of *Capdeville* (2005). The modification is applied only to the across-branch coupling part of NACT, which is linearized under the Born approximation, and not to the PAVA part. Picking up from Eq. (2.3), but working in the frequency domain instead of time domain, the Born perturbation to the seismogram can be written as (*Tanimoto*, 1984):

$$\delta u(\omega) = \sum_{k} \sum_{k'} A_{kk'} \frac{1}{i\omega(\omega^2 - {\omega_k}^2)(\omega^2 - {\omega_{k'}}^2)} \tag{2.9}$$

in which the amplitude term $A_{kk'}$ is the same as given by Eq. (2.3).

Upon inserting (2.4) and (2.5) into (2.9) and separating the terms indexed by (k, m) and those indexed by (k', m'), one finds

$$\delta u(\omega) = \int_V \boldsymbol{R}(\boldsymbol{r}, \omega; \boldsymbol{r}_R) : \delta \boldsymbol{C}(\boldsymbol{r}) : \boldsymbol{S}(\boldsymbol{r}, \omega; \boldsymbol{r}_S)\, dV \tag{2.10}$$

with

$$\boldsymbol{R}(\boldsymbol{r}, \omega; \boldsymbol{r}_R) = \sum_k \Big(\sum_m R_k^m \boldsymbol{e}_k^{m*} \Big) \frac{1}{(\omega^2 - {\omega_k}^2)} \tag{2.11}$$

$$\boldsymbol{S}(\boldsymbol{r}, \omega; \boldsymbol{r}_R) = \sum_{k'} \Big(\sum_{m'} S_{k'}^{m'} \boldsymbol{e}_{k'}^{m'} \Big) \frac{1}{i\omega(\omega^2 - {\omega_{k'}}^2)} \tag{2.12}$$

accounting for the scatterer-to-receiver and the source-to-scatterer contributions, respectively. Returning to time domain, one can write

$$\delta u(t) = \int_V \boldsymbol{R}(\boldsymbol{r}, t; \boldsymbol{r}_R) : \delta \boldsymbol{C}(\boldsymbol{r}) *: \boldsymbol{S}(\boldsymbol{r}, t; \boldsymbol{r}_S)\, dV \tag{2.13}$$

with the "$*$"denoting convolution in time domain, and

$$\boldsymbol{R}(\boldsymbol{r}, t; \boldsymbol{r}_R) = \sum_k \Big(\sum_m R_k^m \boldsymbol{e}_k^{m*} \Big) \frac{\sin(\omega_k t)}{\omega_k} \tag{2.14}$$

$$\boldsymbol{S}(\boldsymbol{r}, t; \boldsymbol{r}_R) = \sum_{k'} \Big(\sum_{m'} S_{k'}^{m'} \boldsymbol{e}_{k'}^{m'} \Big) \frac{1 - \cos(\omega_{k'} t)}{{\omega_{k'}}^2} \tag{2.15}$$

Notice that after the above rearrangement, the double summation over pairs of modes is now split into two single summations in Eq. (2.14) and (2.15), which can be computed simultaneously. The computational cost of the new scheme scales then as $f_{\max}^2$, instead of $f_{\max}^4$ in the original NACT scheme. In the case of multiple sources and receivers, the cost is $(N_S+N_R)* f_{\max}^2$, instead of $(N_S*N_R)* f_{\max}^4$. We further note that the receiver term in Eq. (2.14) can be pre-computed and stored for a given set of receivers, therefore further reducing the computational cost. The asymptotic approximation employed in the original NACT to collapse the 3D volume integral to the 2D great-circle plane integral still applies here.

2.4 Numerical validation

Figure 2.4 shows a numerical test designed to validate the new scheme. Synthetic seismograms are computed down to a shortest period of 30 sec using the original and

modified scheme, respectively, for a cylindrical heterogeneity located between the source and the receiver. The comparison shows very good agreement between the two sets of synthetics both in phase and amplitude. Both the surface wave and the body waves agree well.

Table 2.1 shows a comparison of the time costs for computing a single synthetic seismogram using the two schemes, respectively, for several different cutoff frequencies. The time cost of the new scheme scales roughly as f_{max}^2, whereas the original NACT does f_{max}^3 (rather than f_{max}^4, because in this series of tests a fixed coupling width s_{max} is used. See discussion in the last part of Section 2.2.2). The new scheme outperforms the original scheme by a factor of 2 at 30 sec (as a reminder, the shortest period of data used for constructing a most recent whole global tomography model (*French*, 2014) is 32 sec), and a factor of 6 at 10 sec (relevant for *SS* precursor study). Notice that the comparison in Table 2.1 is for synthesizing only one seismogram. In reality when multiple source and receivers are used, an even larger saving factor will be achieved for the reasons discussed in the previous section.

2.5 Conclusions

We present a modification to the normal mode coupling scheme in NACT, which allows NACT to meet the challenges when approaching higher frequencies. The new scheme is even more advantageous in the case of many sources and receivers, which is the reality of seismic tomography.

So far we have presented the application of the modified scheme to computing synthetic seismograms. It can also be used to compute sensitivity kernels for 3D Earth model, which is the next step forward.

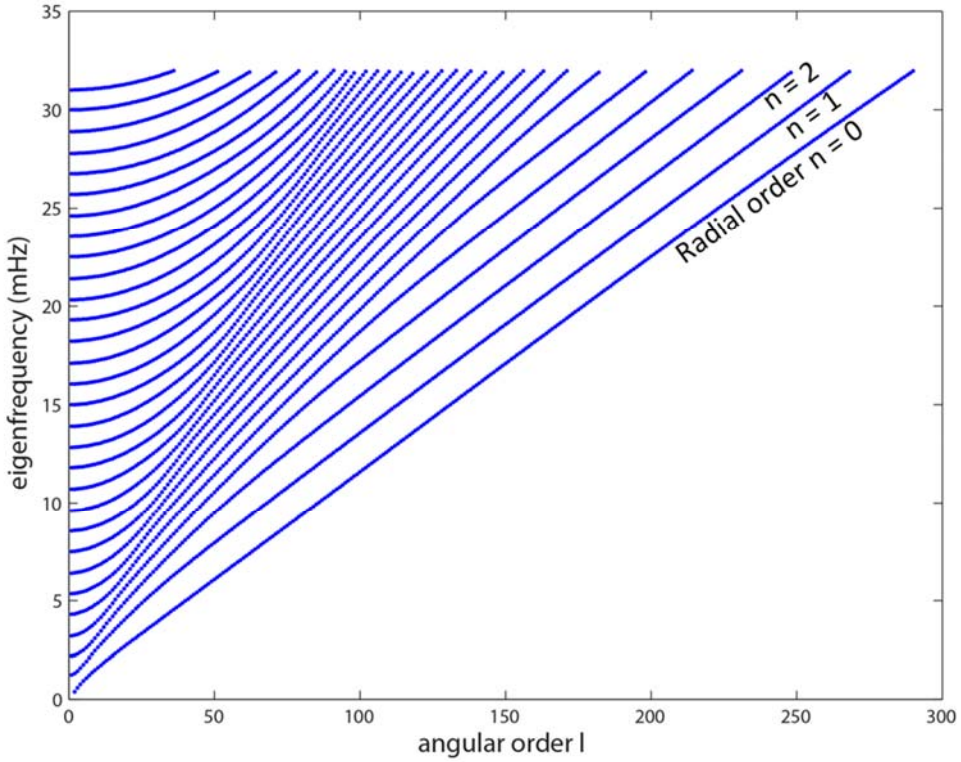

Figure 2.1. Eigen-frequencies of toroidal normal modes computed for the 1D Earth model *PREM* (*Dziewonski* and *Anderson*, 1981), with a maximum cutoff frequency at 32 mHz. Each dot represents one mode. The number of modes for a given cutoff frequency f_{max} roughly scales as $(f_{max})^2$.

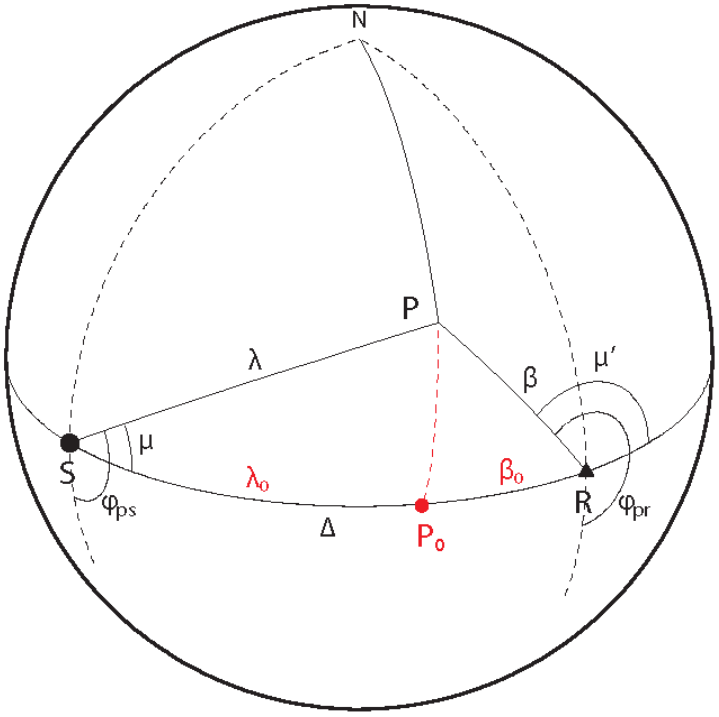

Figure 2.2. Source-scatterer-receiver geometry projected on the unit sphere for which the great circle path is rotated to the equator. Points S, R and P represent the projected seismic source, receiver and scatterer, respectively; Point N is the north pole of the unit sphere; Point P_0 is the projection of P onto the equator. Δ is the angular epicentral distance between S and R; λ the distance between S and P, and β that between P and R. φ_{PS} and φ_{PR} are the azimuth angles looking from S (or R) to P, counted counter-clockwise from south.

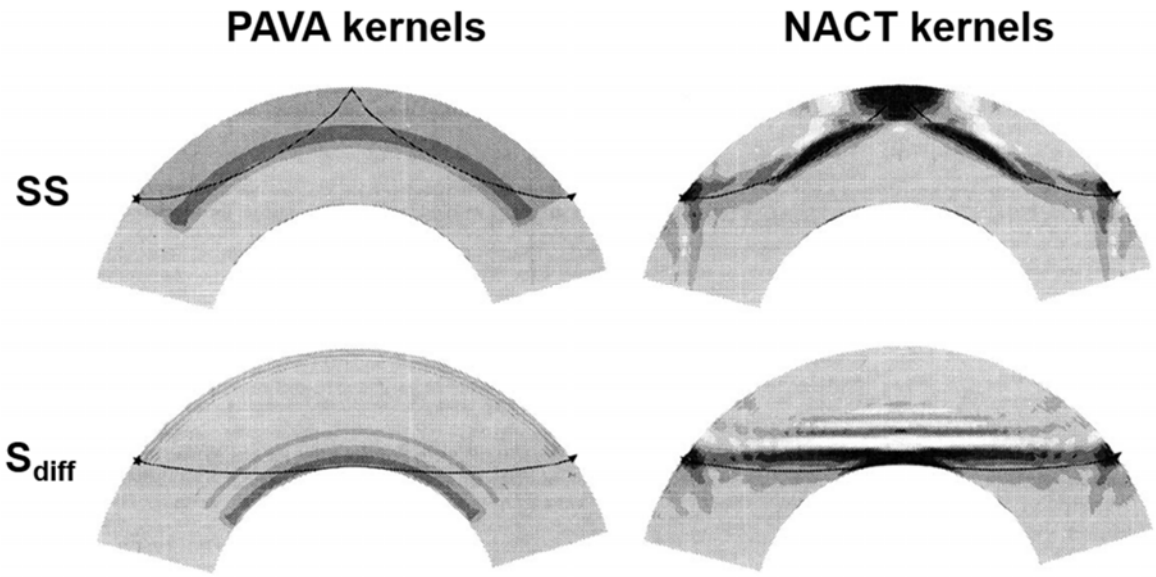

Figure 2.3. (Modified from *Li* and *Romanowicz*, 1995). Examples of sensitivity kernels computed for (top) the *SS* phase and (bottom) the S_{diff} phase, based on (left) the Path Average Approximation (PAVA; *Woodhouse* and *Dziewonski*, 1984) and (right) the Non-linear Asymptotic Coupling Theory (NACT; *Li* and *Romanowicz*, 1995; 1996). Infinite frequency rays are also shown for comparison.

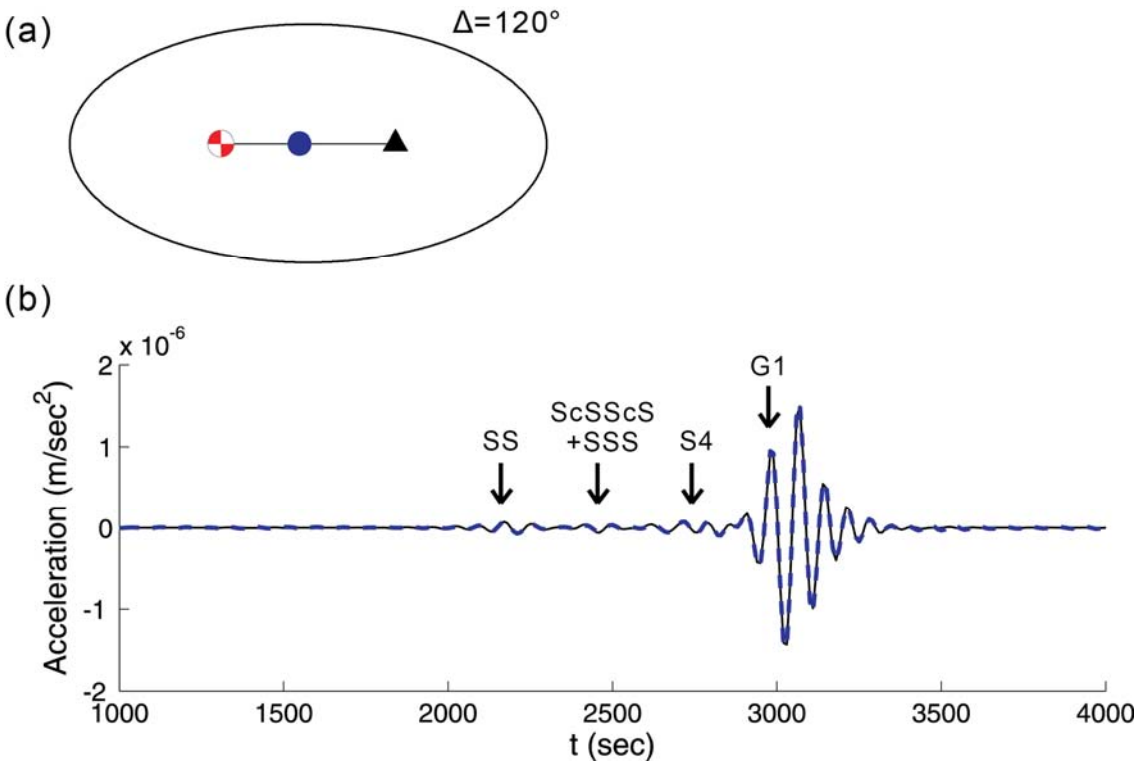

Figure 2.4. (a) Path geometry of the numerical test in map view. A cylindrical velocity anomaly (blue filled circle) in 0-1000 km depth range, with shear velocity 2% faster than *PREM*, is located halfway between the seismic source (focal mechanism shown in red beach ball) and the receiver (black triangle). (b) Transverse component synthetic seismogram down to period of 30 sec computed with the original NACT (black solid line) versus the new formalism (blue dashed line). Main seismic phases are labeled on the seismogram.

Table 2.1: Time cost for computing one synthetic seismogram on a 1GHz single CPU.

Cutoff period ($1/f_{max}$)	Original NACT	Modified NACT
60 sec	7 min	8 min
30 sec	56 min	28 min
10 sec	25 hr	4.5 hr

Chapter 3

Complexity in *SS* Precursor Observations Caused by Mantle Heterogeneities -- Do Double "*SS* precursors" Mean Double Discontinuities?

This chapter has been published in *Geophysical Journal International* under *Zheng* and *Romanowicz* (2012) with the title 'Do double "*SS* precursors" mean double discontinuities?'

3.1 Introduction

Two discontinuities, at 410 and 660 km depths approximately, delineate the Earth's mantle transition zone, which separates the upper and the lower mantle. These discontinuities are widely observed seismically on a global scale and are prominent features in 1D reference models such as *PREM* (*Dziewonski and Anderson*, 1981). There is general agreement that they are caused by phase transitions in mantle minerals, in particular olivine to wadsleyite at the 410 km and ringwoodite to perovskite and magnesiowustite at the 660 km discontinuities (*Ringwood*, 1975; *Ito and Takahasi*, 1989; *Ita and Stixrude*, 1992). The garnet to perovskite transition also plays a role at the 660 discontinuity (*Vacher et al.*, 1998). The depths of the discontinuities serve in principle as a "thermometer" to measure the transition zone temperature anomalies (*Bina and Helffrich*, 1994). The Clapeyron slopes of the olivine transitions predict a shallower 410 and deeper 660 in colder (e.g. subduction zone) regions, and the reverse in warmer (e.g. mantle plume) regions. On the other hand, the garnet transition at the 660, though minor, has an opposite sign (*Ito et al.*, 1990) to the olivine transition, sometimes complicating the prediction (*Weidner and Wang*, 1998; *Herzberg and Gasparik, 1991*). Detailed characteristics of the discontinuities are crucial for understanding the temperature, composition and dynamics of the mantle. For example, it still remains debatable whether mantle convection is confined to layers or is of whole-mantle scale (*Hofmann*, 1997; *Schubert et al.*, 2001). Tomographic studies (e.g. *Li et al.*, 2008) have observed stagnant slabs in the transition zone in particular regions such as the northwest Pacific, suggesting that the 660 discontinuity acts as a barrier for material transfer across it (*Ringwood*, 1994), while at some other locations such as Sumatra and Peru, the slabs appear to penetrate through the transition zone and dive directly into lower mantle (*Fukao et al.*, 2009). Study of the discontinuities will help to put constraints on such hypotheses.

Seismic constraints on the discontinuities first came from array studies of triplications (e.g. *Niazi and Anderson*, 1965) and converted phases (e.g. *Vinnik*, 1977). Later, receiver functions (e.g. *Simmons and Gurrola*, 2000) and multiple ScS reverberations (e.g. *Revenaugh and Jordan*, 1991) were also employed for detecting the discontinuities. Such data types, however, are restricted by station distribution and usually confined to regional scales. In contrast, the *SS* (and *PP*) precursors, which are reflections from the bottom-side of the discontinuities (Figure 3.1), are able to provide a significant global coverage even for oceanic regions, as their sensitivity is concentrated at the mid-point between the earthquake and the seismic station. Since the ray paths of *SS* and its precursors are nearly identical outside the bounce point region, common practice has been to measure the differential travel time between a precursor and the main phase and then translate it to the discontinuity depth at the bounce point. Crust and upper mantle velocity models are assumed for static travel time corrections. The amplitudes of the precursors are generally small (5-10% of the main phase), at or below the noise level. Stacking is therefore

necessary to enhance the signal. Mid-point stacking over geographical bins with radius of 10º has been common. Pioneered by *Shearer* (1991), many studies (e.g. *Flanagan and Shearer*, 1998; *Deuss and Woodhouse*, 2002; *Gu and Dziewonski*, 2002; *Houser et al.*, 2008; *Lawrence and Shearer*, 2008) have employed *SS* precursor travel times to map discontinuity topography and transition zone thickness on the global scale. These results agree on very long wavelength features, however, considerable discrepancies exist on smaller scales (for a review, see *Deuss*, 2009). In addition to 410 and 660 which are present globally, other discontinuities are observed at 220, 300-350, 520, 800-900 km depths for various regions. On regional scales, the precursor method has also been applied to a few locations where denser coverage allows higher resolution. Such regions include the central Pacific around Hawaii (*Schmerr and Garnero*, 2006; *Cao et al.*, 2010; *Cao et al.*, 2011), south America (*Schmerr and Garnero*, 2007; *Contenti et al.*, 2012), eastern Asia (*Heit et al.*, 2010), Japan and Kurile (*Schmerr and Thomas*, 2011) and northwestern Pacific (*Gu et al.*, 2012). In addition to *SS* and *PP* precursors, *P'P'* (*PKPPKP*) precursors are sometimes observed (e.g. *Le Stunff et al.*, 1995), however strict requirements on ray path geometry confines their application to very few regions.

3.2 Data

The deployment of the US Transportable Array (TA) brings new opportunities to try and resolve finer scale discontinuity characteristics for much broader regions. As a rule of thumb, given the average inter-station distance of 70 km, the spacing between bounce points is half of that, i.e. 35 km. Here we present an observation of *SS* precursors from an m_b 6.7 earthquake (May 2010; depth 38 km) occurring in northern Sumatra and recorded at the US Transportable Array (Figure 3.2). The magnitude of this event is optimal in that the precursor signals are strong enough, while the source duration is relatively short (~10 seconds) compared to the frequency content of the precursor energy (~30-40 seconds). The source time function is fairly simple as revealed by the waveforms of main phases. A shallow depth is chosen to avoid interference between one precursor's depth phase and the next precursor, as is common practice in precursor studies. The event has a radiation pattern that favors *SS* on the transverse component. All available stations from the Transportable Array at the time of the event are used. The epicentral distances fall in the range between 120 and 150º, which is very suitable for an *SS* precursor study. We consider the transverse component displacement seismograms band-pass filtered in the range 20-100 seconds (shorter periods are also tested). Later we also take into account the radial component.

In this particular case, the precursor signals are well above noise level on most individual traces throughout the entire array, exempting us from the need of stacking. Figure 3.3(a) shows a record section of one particular azimuth range (20~23º). The traces are arranged according to epicentral distance. Two signals around the theoretical $S_{660}S$ arrival time

(dots) can be tracked down coherently across the profile. Their amplitudes are anomalously strong compared to PREM prediction (Figure 3.3b). Vespagram analysis (Figure 3.4) reveals that both signals have a slowness that is close to the theoretical value for *SS* precursors. In conventional interpretation, the double precursors would imply two discontinuity reflectors in the bounce point region. One would further estimate their depths to be around 660 and 810 km, respectively, based on their travel times.

3.3 One-dimensional and three-dimensional modeling

We attempt to fit the observations with both 1D and 3D modeling. For the 1D case, synthetics are computed for the *PREM* model using normal mode summation. The synthetics are band-pass filtered between 20 and 100 seconds (same as that applied to the observed waveforms). The eigenfunctions for mode summation are complete down to 10 seconds, which is sufficient for the frequency band we study. A record section of 1D synthetics is shown in Figure 3.3(b). As expected, only one $S_{660}S$ precursor is present, as there is only one 660-discontinuity in the *PREM* model.

We then conduct 3D modeling using a tomographic global mantle shear velocity model *S362ANI* (*Kustowski et al.*, 2008) in combination with *CRUST2.0* (*Bassin et al.*, 2000). The Spectral Element Method (*Komatitsch* and *Tromp,* 2002a,b) is employed for computing synthetics that are accurate at periods >17 seconds. They are then band-pass filtered between 20 and 100 seconds, in the same way as applied to the data and 1D synthetics. The corresponding record section of 3D synthetics is shown in Figure 3.3(c). A close inspection of the precursor waveforms (Figure 3.5) and the amplitude measurements (Figure 3.6) shows that the 3D synthetics fit the observations much better than the 1D synthetics. Surprisingly, the 3D model is capable of producing the double $S_{660}S$ precursors, even though only a single 660-discontinuity is present in the model. This implies that the apparent "double precursors" seen on the 3D synthetics are produced by heterogeneity rather than double discontinuities at the bounce point. In order to rule out the possibility of artifacts due to numerical implementation of the 3D crust, we have replaced CRUST2.0 with a 1D layered crust in the simulation, and we find the key features in the synthetics do not change. We have also validated our 3D synthetics by comparison against those provided by the Global ShakeMovie project (http://global.shakemovie.princeton.edu; *Tromp et al.*, 2010), and they agree perfectly.

It is also noteworthy that the 1D synthetics fail by far to fit the anomalously large $S_{660}S$ amplitudes as observed, whereas the 3D model is able to reproduce the amplitudes of both precursors considerably better. As Figure 3.6 shows, the 1D synthetics fail completely (an order of magnitude difference) to predict the amplitudes of the precursor #1, and for #2, the amplitude discrepancy between the observed and the 1D synthetics is a factor of 2 (a difference of 0.3 on the log_{10} scale) on average and up to 4 at the

maximum. On the other hand, the 3D synthetics are able to fit the observed amplitudes for both precursors, as well as the pattern (i.e. how amplitude vary with epicentral distance) to a certain degree. In order to improve the 1D fit, we have tried other 1D models with extremely large impedance contrast across the 660-discontinuity, however they do little to improve the amplitude fits.

In the next step, we test the effect of discontinuity topography (*Chaljub and Tarantola*, 1997), as it is present in the 3D model *S362ANI*. We run one more simulation with the same 3D model except the topographies on the 410- and 660-discontinuities are removed. The synthetics are compared to the model with discontinuity topography for several traces (Figure 3.7). The two sets of synthetics look almost identical. In other words, the (long wavelength) undulations of discontinuities have negligible impact on the precursor amplitudes and waveforms at least for the 3D model considered.

3.4 Not because of bounce point structure?

In the next stage of modeling, we try to pinpoint the structure that is responsible for the "double precursors" seen on the 3D synthetics. The most probable candidate is certainly the bounce point region. In Figure 3.8, a few depth slices of V_{SH} (horizontally polarized shear wave speed) perturbations from the 3D mantle model *S362ANI* are shown. The subducted Pacific slab appears to split into two pieces as it dives below 300 km depth. The two pieces pond in the transition zone above the 660 discontinuity, and a "slab hole" is seen in between. The southern piece further extends down to depths greater than 700 km. Based on these images, we conjectured a simple hypothesis (Figure 3.9) to explain the double precursors on the 3D synthetics. In this conceptual model, the specular reflection generates the second (later arrival) $S_{660}S$ precursor, which is also present on 1D synthetics, while the reflection at the bottom of the high velocity slab pieces constitutes the first precursor, which is present on 3D synthetics and observed traces but not on 1D synthetics. In more detail, due to the different size and shape of the two slab pieces, their underside reflections are expected to arrive at slightly different times, which would explain the slight split of the first precursor seen on the 3D synthetics (Figure 3.6).

To test this hypothesis, in the next simulation, only the 3D structure in the vicinity of the precursor bounce point region is preserved (Figure 3.10a). In particular, we define a column centered at the approximate centroid of the bounce points, and with a radius of 25 degrees. We keep the velocity perturbations inside the column while we remove the perturbations everywhere outside. A cosine taper is applied at the edge of the column to avoid artifacts due to abrupt cutoff. The synthetics corresponding to this model are shown in Figure 3.10(b). To our surprise, the "double precursor" phenomenon disappears. We try to vary the radius of the column as well as the smoothness of the taper, but there is

always only one $S_{660}S$ precursor present. The amplitudes of the precursor are also small. Overall, this set of synthetics has very similar characteristics as in 1D.

Since bounce point structure is not capable of reproducing the double precursors, we turned to the receiver side. Figure 3.10(c) shows a slice (depth at 125 km) of the 3D model *S362ANI* in North America. Indeed, a sharp contrast between the fast craton east of the Rocky Mountain Front and the slower western US is present in the North American upper mantle, a prominent feature also seen in numerous continental scale tomography studies (e.g. *van der Lee* and *Frederiksen*, 2005; *Marone et al.*, 2007; *Nettles* and *Dziewonski*, 2008; *Yuan et al.*, 2011) although a more detailed geometry of the boundary is resolved in the regional models due to higher resolution. Moreover, the boundary between the fast and slow regions is sub-parallel to the great circle paths for the event studied here. In the following simulation, we preserve only the receiver side upper mantle structure in the 3D model (Figure 3.10c), and the corresponding synthetics are shown in Figure 3.10(d). This set of synthetics turns out to be capable of reproducing the "double precursors". In order to confirm that the apparent "double precursors" are indeed associated with the velocity boundary, we constructed another model (Figure 3.10e) in which the boundary is significantly shifted eastwards while its orientation still tracks the great circle ray path direction. In this simulation we also expanded the array of virtual receivers to the entire US in order to cover a broad range of azimuths across the boundary. The locations of the receivers are taken from the Transportable Array stations, past, present and future. The synthetics from this simulation are shown in Figure 3.10(f), arranged by increasing azimuth (from east to west roughly). It is seen that for receivers far away from the boundary (azimuth <8º or >20º) there is only one precursor (the later one); whereas the other wiggle (the earlier one) picks up when the receivers approach the boundary (azimuth around 14º). These experiments imply that apparent "double precursors" do not necessarily require double discontinuities or even any complex structure at the bounce point, as commonly assumed by previous precursor studies. Mantle heterogeneities away from the bounce point region are able to generate similar features, which could be very misleading if care is not taken.

We note that we also tested a source-side model in a similar way, but it fails to produce double precursors.

3.5 Not SS precursors?

So far we have focused our analysis on the transverse component. We here consider the radial component. As shown in Figure 3.11, on the radial component, both "precursors" are present with much larger amplitudes than the transverse (a factor of >4), while the *SS* main phase has amplitudes that are smaller than those on the transverse component. This disproportionality suggests the possibility that the two "precursors" (previously identified

by arrival times and slownesses, which is common practice in precursor studies) are in fact not precursors.

In order to explain these observations, we consider possible body wave phases that have similar travel times. In Figure 3.12, the theoretical arrivals of *PPS*, *PPPS*, *PPPPS* and *PPPPPS* phases (referred to as *P*(n)*S* hereafter) are marked. They fit the arrival times of the "precursors" on the radial component reasonably well. These are supposedly *SV* energy and should not be expected on the transverse component (indeed they are not present on the 1D synthetics). In this particular setting, however, as the ray paths graze the velocity boundary, due to off-great-circle reflection and refraction, some *SV* energy could possibly leak to the transverse component, thus generating the apparent "precursors". The arrival times and slownesses of these *P*(n)*S* phases are close enough to the *SS* precursors, leading to the phase misidentification. This is not to say an $S_{660}S$ precursor is not present, but the real precursor (there should be only one, because only one 660-discontinuity is present in the 3D models) is strongly contaminated or buried by the interfering energy. In fact, the high similarity between the radial and transverse component waveforms in the precursor time window (see Figure 3.11) seems to suggest that the energy leaked from the radial component is dominant over the real precursor on the transverse component. The phases arriving ~40 seconds after the expected *SS* on the radial component can be understood similarly as *P*(n)*SS*.

Particle motion analysis (Figure 3.13) of the "precursors" further confirms our inference that they are artifacts associated with the velocity boundary. As shown by Figure 3.13(a), the particle motions of the 1D synthetics (top row) appear to be radially polarized (i.e. no or near zero motion on the T component) for all the azimuth bins, whereas the trajectories of the observed traces (middle row) and 3D synthetics (bottom row) both show a "tilt" (i.e. non-zero motions on both R and T components). Figure 3.13(b) shows the particle motion of the 3D synthetics from the modified receiver-side 3D model (Figure 3.10e). The effect of the velocity boundary (located at azimuth = 14º) is demonstrated by how the particle motion pattern changes with the azimuth. The "tilt" of the particle motion pattern appears, peaks and disappears as the receivers approach, pass and leave the velocity boundary. These particle motion trajectories show no or minimal ellipticity, which suggests that anisotropy does not play an important role compared to the effect of the boundary.

3.6 Discussion

Unlike the 410, the 660 discontinuity has been known to exhibit a higher level of complexity (see *Deuss*, 2009 for a review). Multiple discontinuities around and deeper than 660 km depth have been observed at several locations by various data types and methods. For instance,) from *P* to *S* receiver functions (0.3 Hz), *Simmons and Gurrola*

(2000) discovered a laterally continuous discontinuity at ~720-750 km depths beneath southern California, which they inferred to be garnet to perovskite transformation. *Andrews and Deuss* (2008) assembled a global dataset of *P* to *S* receiver functions (0.01-0.02 Hz; 0.02-0.5 Hz), in which about half of the stations show a complex 660 signal, either a broadened single peak or a main 660 accompanied by a smaller, deeper peak in the depth range 710-860 km. They modeled the observations with a combination of a sharp discontinuity representing the olivine dissociation and velocity gradients from the garnet tranformation. *Deuss et al.* (2006) collected a global *PP* precursor dataset and discovered double peaks at 660 and 720 km , for a few locations (such as Canada), when the *PP* stack is filtered at shorter periods (8-75 sec). Using migration of high frequency *PP* precursors, *Thomas and Billen* (2009) detected a split 660 in Molucca Sea region with the deeper discontinuity at 690-710 km. Using a similar method, *Schmerr and Thomas* (2011) detected an intermittent secondary reflector at >800 km depth at certain locations in the Kurile subduction zone. In a review paper, *Deuss* (2009) provided depth histograms of reflectors detected by global *SS* and *PP* precursors. The histogram of *SS* shows a local maximum at around 800 km depth. Indeed, stacks for a variety of regions show robust reflectors at this or slightly greater depths. For example, the stack for Asia shows a strong reflector at 850 km (from *SS*) or 820 km (from *PP*), and the one for the Indian Ocean has a strong reflector at 800 km from SS precursor analysis, but its amplitude is much weaker from *PP* precursors.

While the split 660 (additional discontinuity with depth up to 720 km) has often been interpreted as due to a phase transition in garnet, the additional discontinuities at greater depths (800-850 km) lack a good explanation (*Deuss*, 2009). The mechanism revealed by this study provides a possible way to understand at least some of these observations. It is noteworthy that the artificial $S_{660}S$ (the earlier one of the double "precursors") in this study translates to a discontinuity at approximately 810 km depth. It would have been interesting to examine the *PP* precursors for this same event, since they are relatively unlikely to be affected by the artifact mechanism proposed. However, given the epicentral distances considered, the *PP* precursors are severely interfered with other phases of much larger amplitudes, making the observations of *PP* precursors not possible.

In addition to the event studied here, we have also analyzed a few more events at nearby locations (within 2 degrees away from this event). Due to their either smaller (therefore lower signal-to-noise ratio) or larger (therefore longer and more complicated source time function as well as more signal-generated noise) magnitudes, it is not possible to identify precursors on individual traces across the array as done for this event. Nevertheless we have looked at the noise free 3D synthetics made available from the Global ShakeMovie project, and the synthetics indeed exhibit a very similar feature of apparent "double precursors" as seen for this event.

This study suggests that one should be cautious in the interpretation of conventional *SS* precursor travel time studies. The observation of apparent "double precursors" may not necessarily require double discontinuities at the bounce point. In fact, it may not even indicate any complex structure in the bounce point region. Mantle heterogeneities away from the bounce point region are able to generate artificial "precursors" systematically across a vast area, which can be very misleading if care is not taken when interpreting them. Such artifacts could not be remedied by a static travel time correction in stacking (Figure 3.14). In addition to multi-pathing as shown in this study, other mechanisms such as upper mantle anisotropy could also play a similar role in leaking energy to the transverse component.

In the past, a few studies (*Zhao and Chevrot*, 2003; *Lawrence and Shearer*, 2008; *Bai et al.*, 2012) have attempted to address the importance of 3D heterogeneities, however, the focus has been on how much the 3D structures would perturb the precursor travel time measurement, but no attention has been paid to precursor phase identification itself. Moreover, in these studies, the effect of 3D structure on the precursor travel times have been studied and presented in a statistical framework, therefore it was not clear exactly which part of the 3D heterogeneities affect the behavior of the precursors, and how. Our study provides a new perspective.

Admittedly, the case considered in this study corresponds to a specific ray path geometry that is subparallel to the orientation of the heterogeneity boundary. Nevertheless, it constitutes a valid warning concerning the usage of array data such as from USArray. For regions such as the one in this study (Okhotsk Sea), other data types (receiver functions, triplications, *P'P'* precursors, etc.) are not available due to sparsity of seismic stations, so that *SS*/*PP* precursors would be the main tool for studying mantle discontinuities. Due to an overwhelming number of stations, the USArray could dominate the *SS* precursor stack and possibly lead to erroneous conclusions about the transition zone and slab structure in the region. As much as the USArray provides hope for improving resolution of precursor studies, attention must be given to contamination by upper mantle effects on the station side. The same applies to studies based on other regional arrays. One fact worth pointing out is that when smaller seismic arrays are designed, they oftentimes follow local geology in order to enhance signal coherency (e.g. the Grafenberg array), which might potentially give rise to artifacts as described in this study.

SS precursor studies prior to the days of USArray might also suffer from the described problem, to some degree. Global studies are probably less affected, owing to more or less even azimuthal coverage in many regions (see Figure 3.15).

3.7 Conclusions

We present observations of *SS* precursors (reflections off the bottom side of upper mantle discontinuities at midpoint) from an m_b 6.7 earthquake recorded at the US Transportable Array. In this particular case, we observe apparent "double $S_{660}S$ precursors", both strong enough to be visible on individual seismograms coherently across the array. We compute 1D and 3D synthetic seismograms, and find that the 3D synthetics fit the observations significantly better than the 1D synthetics. We discover that the "double precursors" are seen on the 3D synthetics, even though only one 660-discontinuity is present in the earth model. Through further modeling, we confirm that the "double precursors" on the synthetics are not generated due to double discontinuities at the bounce point, but rather by scattering at a sharp velocity boundary on the receiver-side with an orientation sub-parallel to the great circle ray paths. We also find that neither are "*SS* precursors", but most likely *SV* energy leaked from the radial component due to heterogeneity. The real $S_{660}S$ precursor is buried in the second apparent "precursor".

Through numerical 3D modeling of the precursor waveforms, we have found that apparent *SS* precursors may not necessarily reflect the characteristics of mantle discontinuities in the bounce point region, as often assumed by conventional precursor travel time studies. Heterogeneities away from the bounce point region are able to generate artificial "precursors" in a coherent and therefore misleading way. This raises a caution for identifying and interpreting *SS* (and perhaps *PP*) precursors.

We note that this analysis has only been possible because of the possibility of computing highly accurate numerical synthetics in a 3D Earth model, a recent development in global seismology (*Komatitsch* and *Vilotte*, 1998; *Komatitsch* and *Tromp,* 2002a,b). We also note that, even though current global tomographic models are still relatively smooth, they are accurate enough to reproduce some of the effects of structural boundaries on seismic body wave propagation. Finally, we recognize that the USArray allows unprecedented density of ray coverage both in azimuth and distance, albeit in limited ranges.

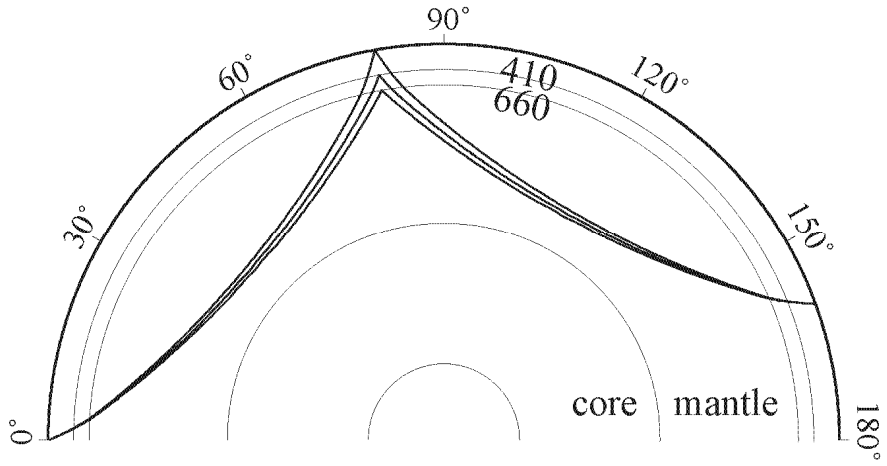

Figure 3.1. Ray paths of *SS* and its precursors. The precursors are the underside reflections off the upper mantle discontinuities of the Earth. They travel very similar but slightly shorter paths than the main phase *SS* and therefore arrive earlier on seismograms, hence the name "precursors". They are named according to the associated discontinuities, for example $S_{410}S$ and $S_{660}S$.

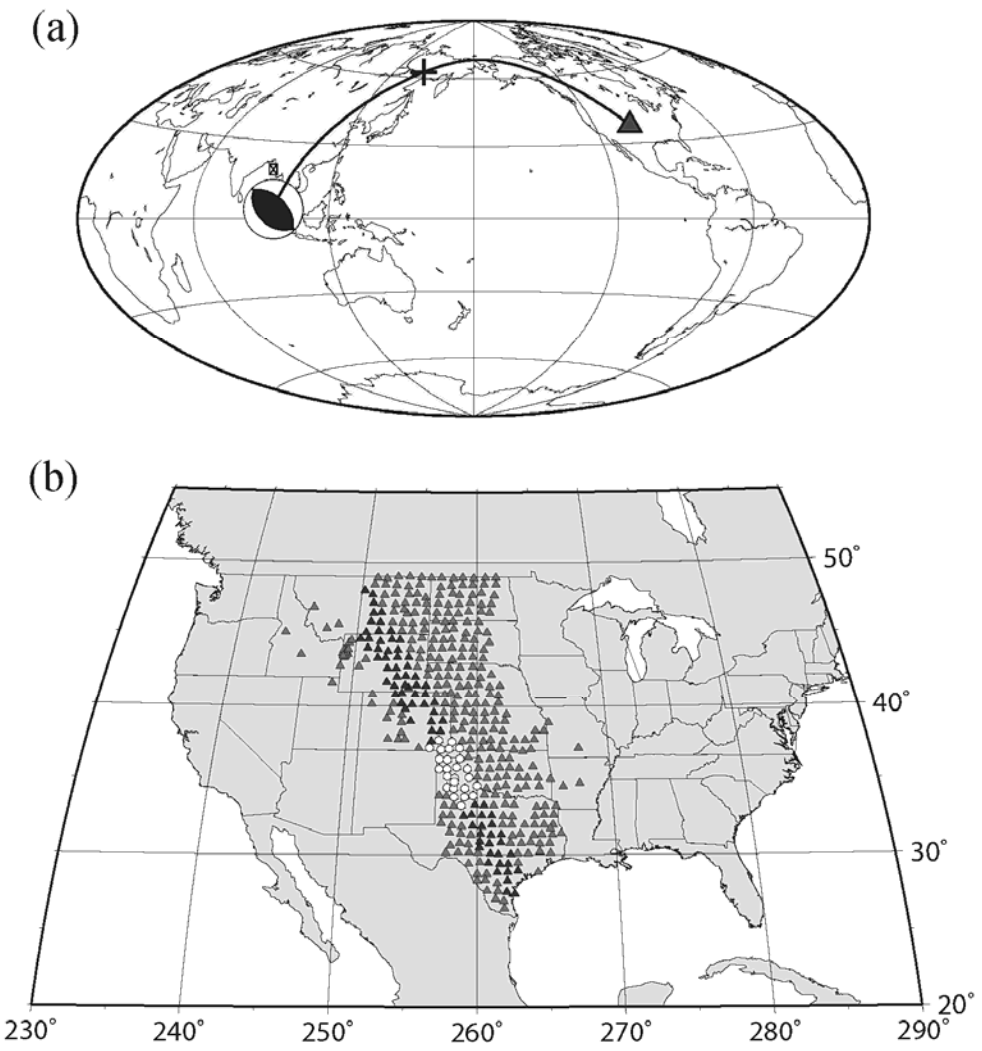

Figure 3.2. (a) A representative *SS* ray path from the target event to the US Transportable Array (TA) used in this study. The beachball marks the location and focal mechanism of the event. The triangle marks the approximate location of TA. The cross denotes the bounce point, which is located approximately half way between the source and the receiver. (b) A map of the TA stations (triangles). They are binned by azimuth and distance for further analysis. Black triangles indicate the stations in the azimuth range of 20-23º, which are chosen to plot record sections in forthcoming figures. Within this azimuth range, the stations in the distance range of 135-140º are shown in white circles.

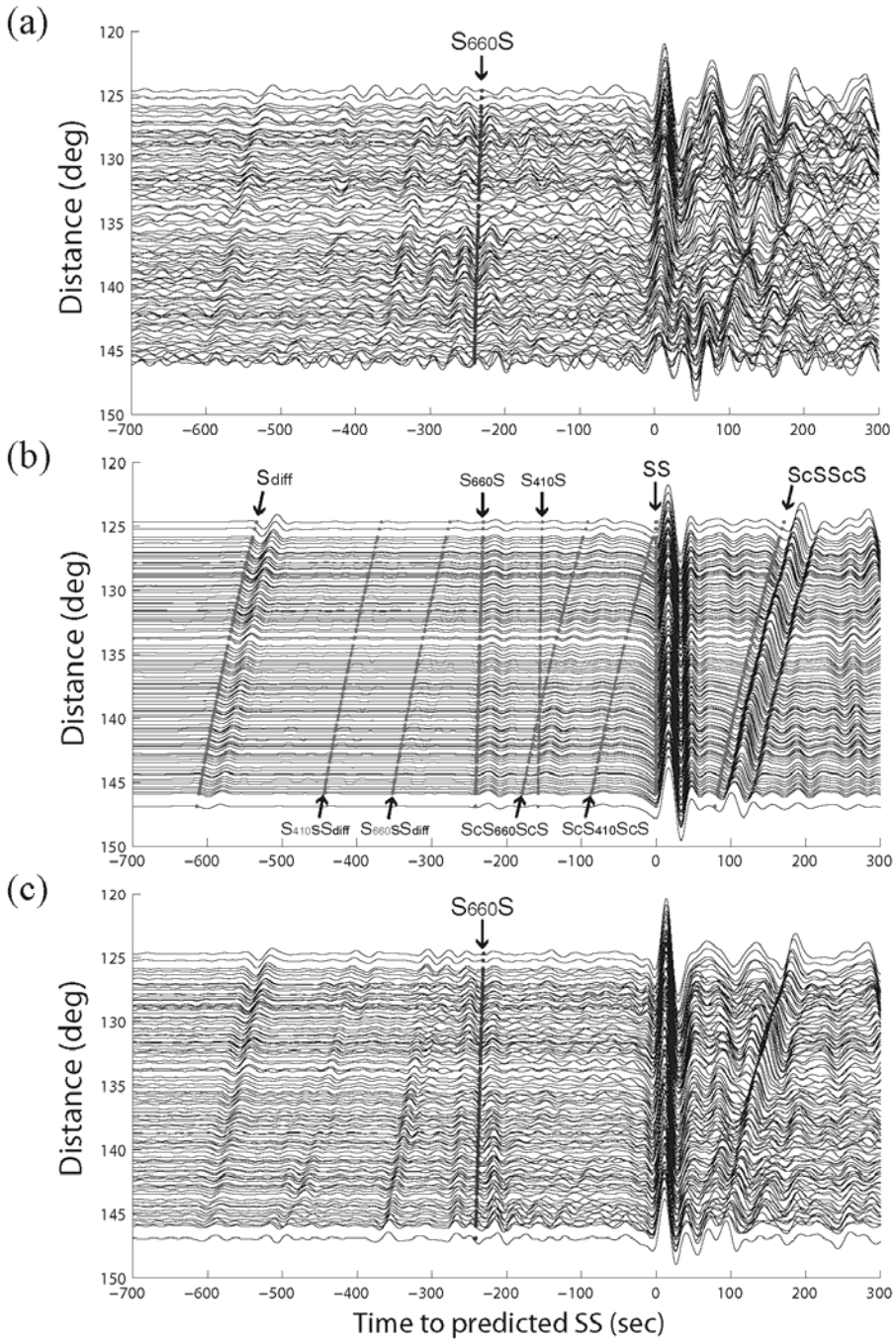

Figure 3.3. Transverse component record sections of (a) observed waveforms, (b) 1D synthetics and (c) 3D synthetics for stations in the azimuth range of 20-23º, aligned on the theoretical arrivals of the main phase *SS*. Major seismic phases and their associated precursors are marked by dotted lines on the 1D synthetics, for reference. The *PREM* model [*Dziewonski* and *Anderson*, 1981] is used to calculate the theoretical arrival times of these phases. The $S_{660}S$ precursors are marked on the observations and 3D synthetics.

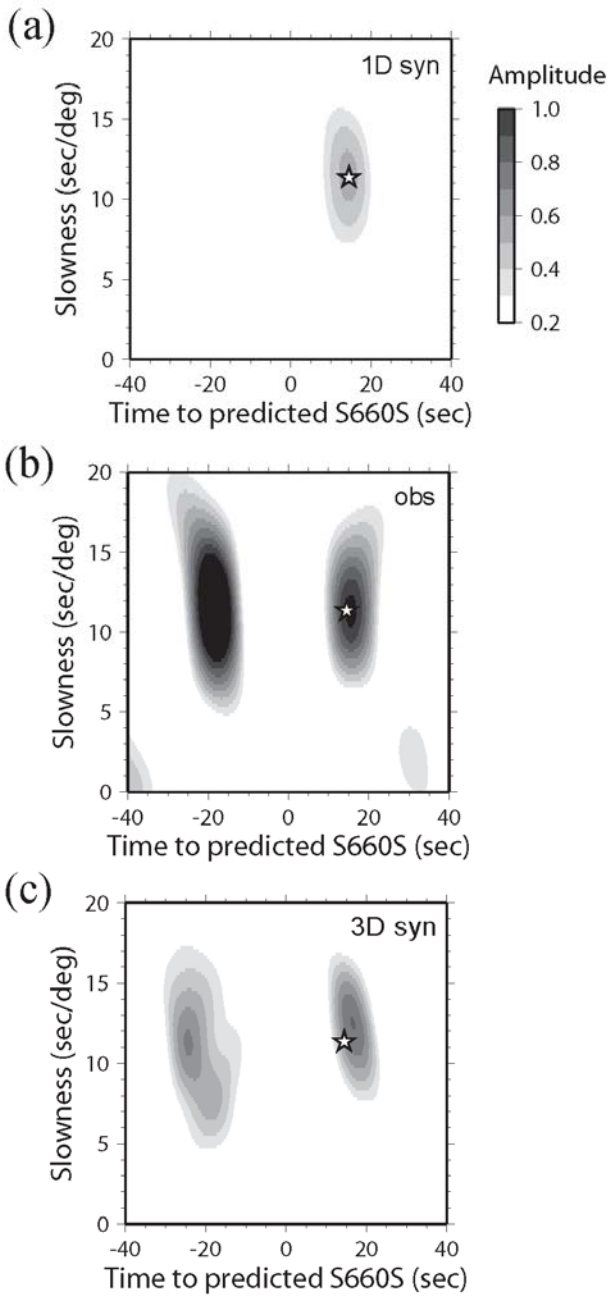

Figure 3.4. Vespagrams of (a) 1D synthetics, (b) observations and (c) 3D synthetics in the $S_{660}S$ precursor time window. A simple slant stacking (linear) technique is used. The stars denote the peak picked from the vespagram of the 1D synthetics. Its position is in agreement with predictions calculated by the *TauP* toolkit [*Crotwell et al.,* 1999] for *PREM*. The arrival time indicated by the star is ~14 seconds later than the *PREM* prediction (0 on the x-axis), which is understood because *TauP* calculates arrival times at infinitely high frequency (i.e. onset of the phase) whereas the vespagram looks for maximum energy.

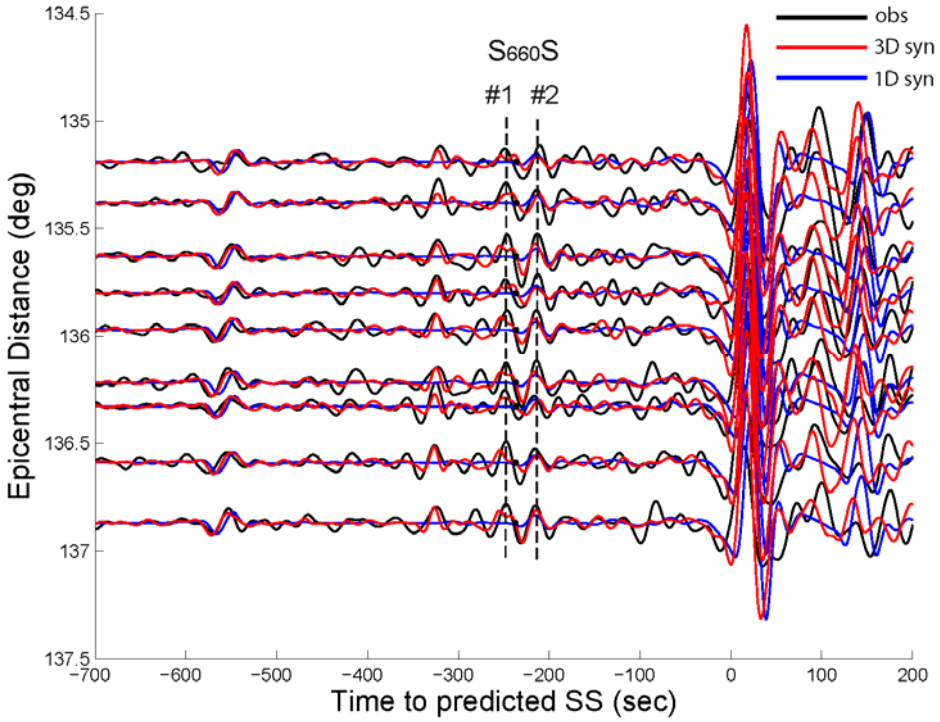

Figure 3.5. A close-in view of waveform comparison between the observed (black line), the 3D synthetics (red line) and the 1D synthetics (blue line). Two coherent phases, labeled #1 and #2, respectively, are identified around the theoretical arrival of the *S660S* precursor (marked by a dot on each trace) in the observed traces. This observation of "double precursors" is predicted by the 3D synthetics, despite the slight split of the #1 phase. In contrast, the 1D synthetics are flat in the time window of the #1 phase.

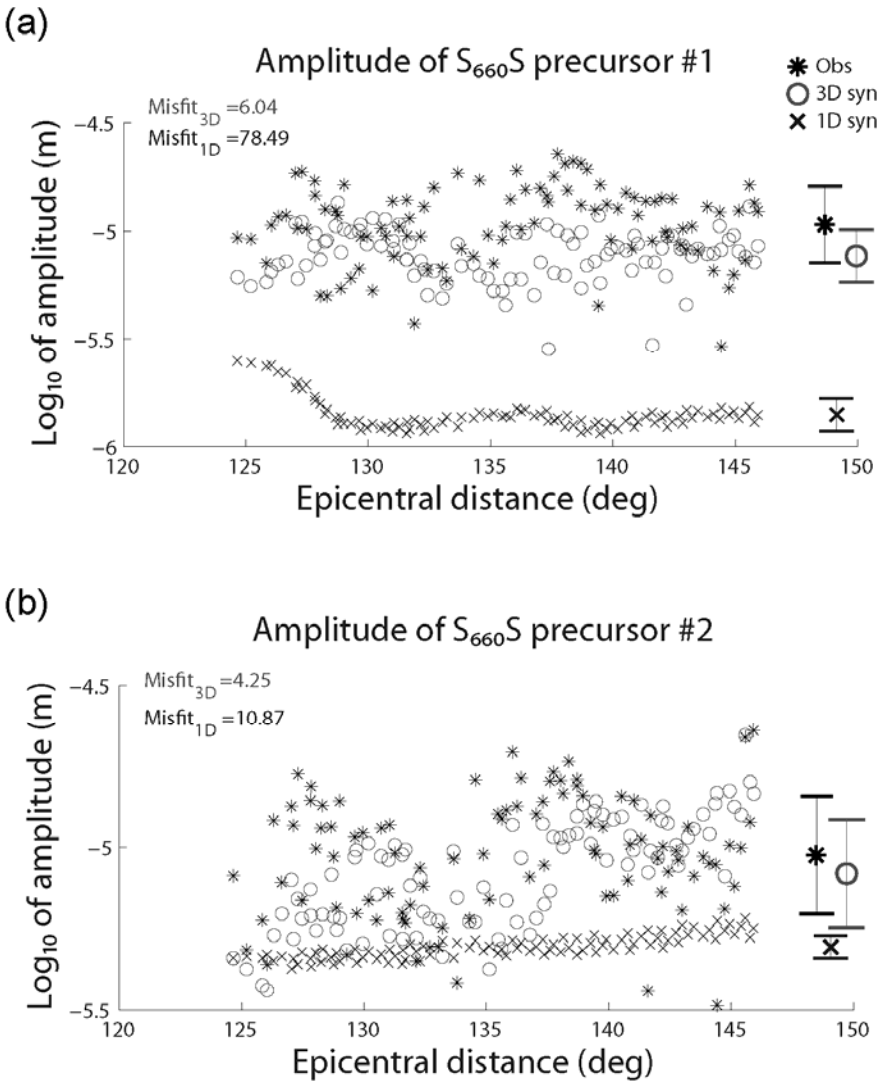

Figure 3.6. Measurements of the $S_{660}S$ precursor amplitude as a function of epicentral distance for the observations (stars), 3D synthetics (circles) and 1D (crosses), in the time windows of (a) precursor 1 and (b) precursor 2. The azimuth range of 20-23º is chosen for the measurements. The error bars on the right shows the mean and standard deviation from the observations, 3D and 1D synthetics, respectively. Misfits by 3D and 1D synthetics are listed at the top left of each panel. The misfit is defined as $\Sigma_i \, |log_{10}A^0{}_i - log_{10}A^1{}_i \,|$, where i is the index of trace, A^0 is the amplitude measured from observed and A^1 measured from 1D or 3D synthetics. The larger 1D amplitudes of precursor #1 at distance < 128º is due to interference of $S_{660}sSdiff$ (labeled on Figure 3.3b).

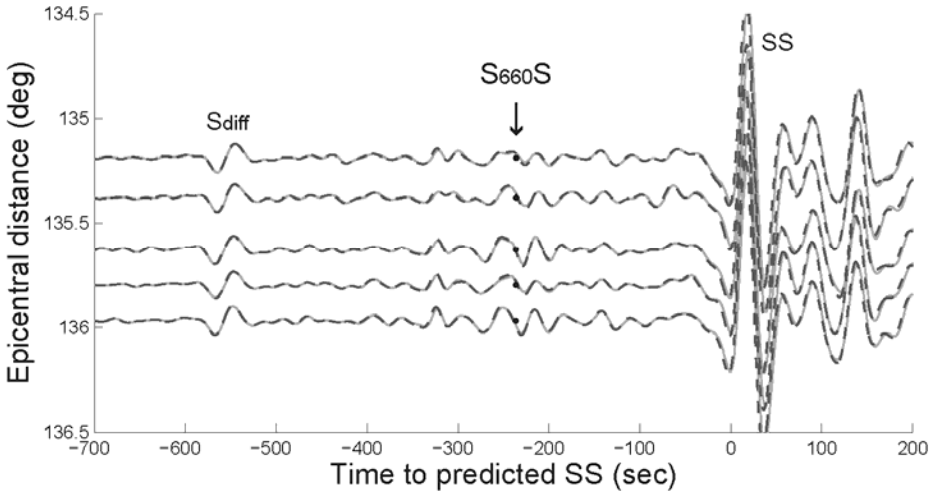

Figure 3.7. Comparison of synthetics from a 3D simulation in which the discontinuity topography is present (solid line) versus one in which the topography is removed (dashed line). The dots denote theoretical arrivals of $S_{660}S$.

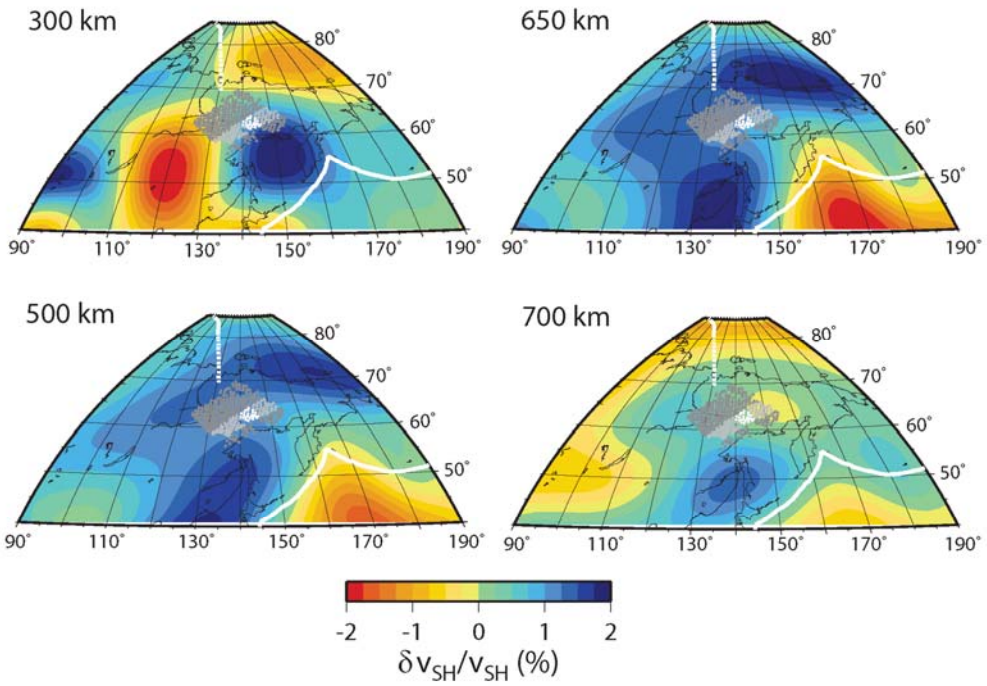

Figure 3.8. Depth slices of 3D mantle tomography model *S362ANI* [*Kustowski et al.*, 2008] in the SS bounce point region (the northern bank of Okhotsk Sea). The white curves delineate plate boundaries. The gray dots denote precursor bounce points. Light gray dots correspond to stations in the azimuth range of 20-23º; white ones stations in the distance range of 135-140º.

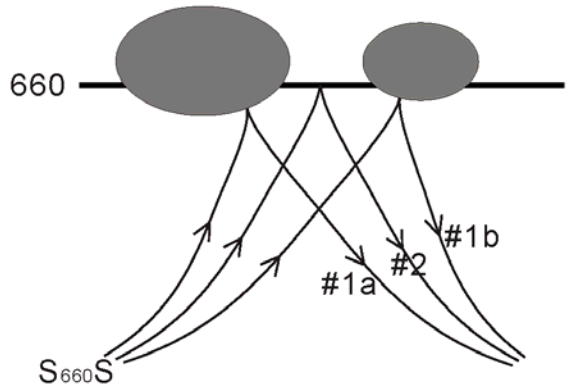

Figure 3.9. A schematic illustration of the "slab hole" concept (vertical section view) which fails to explain the double precursors produced on the 3D synthetics. The two shaded blobs represent the two slab pieces ponding on the 660 km discontinuity, as revealed by the 3D model *S362ANI*.

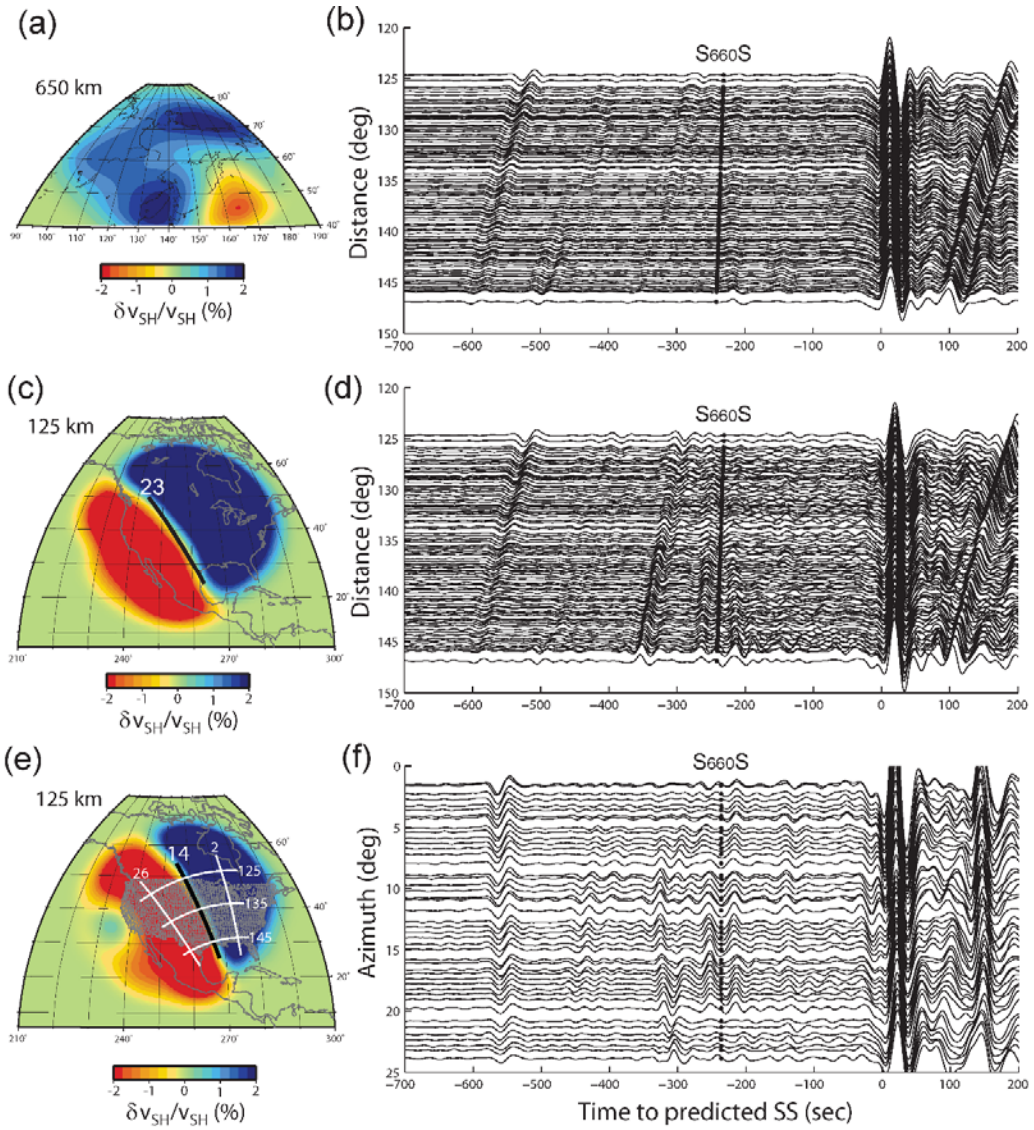

Figure 3.10. Results of 3D modeling: velocity models (left panels) modified from *S362ANI* and corresponding synthetics (right panels). The top row displays a model in which only 3D structures in the precursor bounce point region are preserved. The middle row shows a model in which only upper mantle structures near the receivers are preserved. A clear velocity boundary between the slower western US (red) and the faster craton (blue) on the east is seen. The orientation of the boundary roughly follows the great circle track with an azimuth of 23º (black thick line). The bottom row shows a model modified from the middle row one, in which the velocity boundary is shifted eastward to follow the great circle track at 14º azimuth (black thick line). An expanded set of virtual receivers (gray dots) is used in this simulation, the locations of which are taken from the TA, past, present and future stations. The thick lines indicate equi-azimuth (2, 14 and 26º) and equi-distance (125, 135 and 145º) curves. In (b) and (d), the synthetic traces in the azimuth range of 20-23º are plotted, sorted by epicentral distance. In (f), the synthetics are arranged by azimuth for all receivers in the distance range of 135±1º.

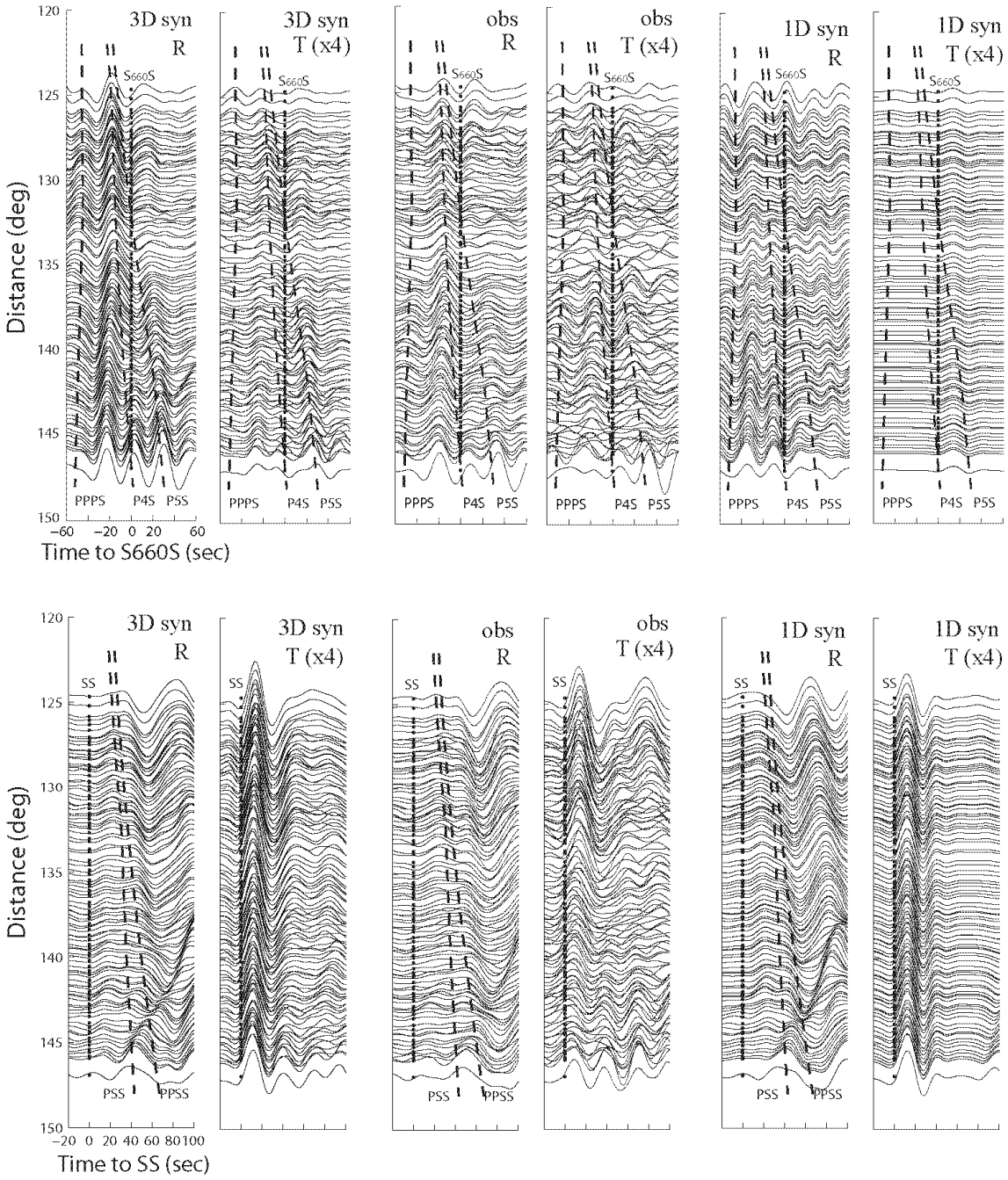

Figure 3.11. Comparison of radial and transverse component waveforms in the $S_{660}S$ (top) and *SS* (bottom) time windows for 3D synthetics, observations and 1D synthetics. The transverse component amplitudes are blown up by a factor of 4. The $S_{660}S$ and *SS* theoretical arrivals are marked by dotted lines, and the *PPPS*, *P4S*, etc. phases by dashed lines.

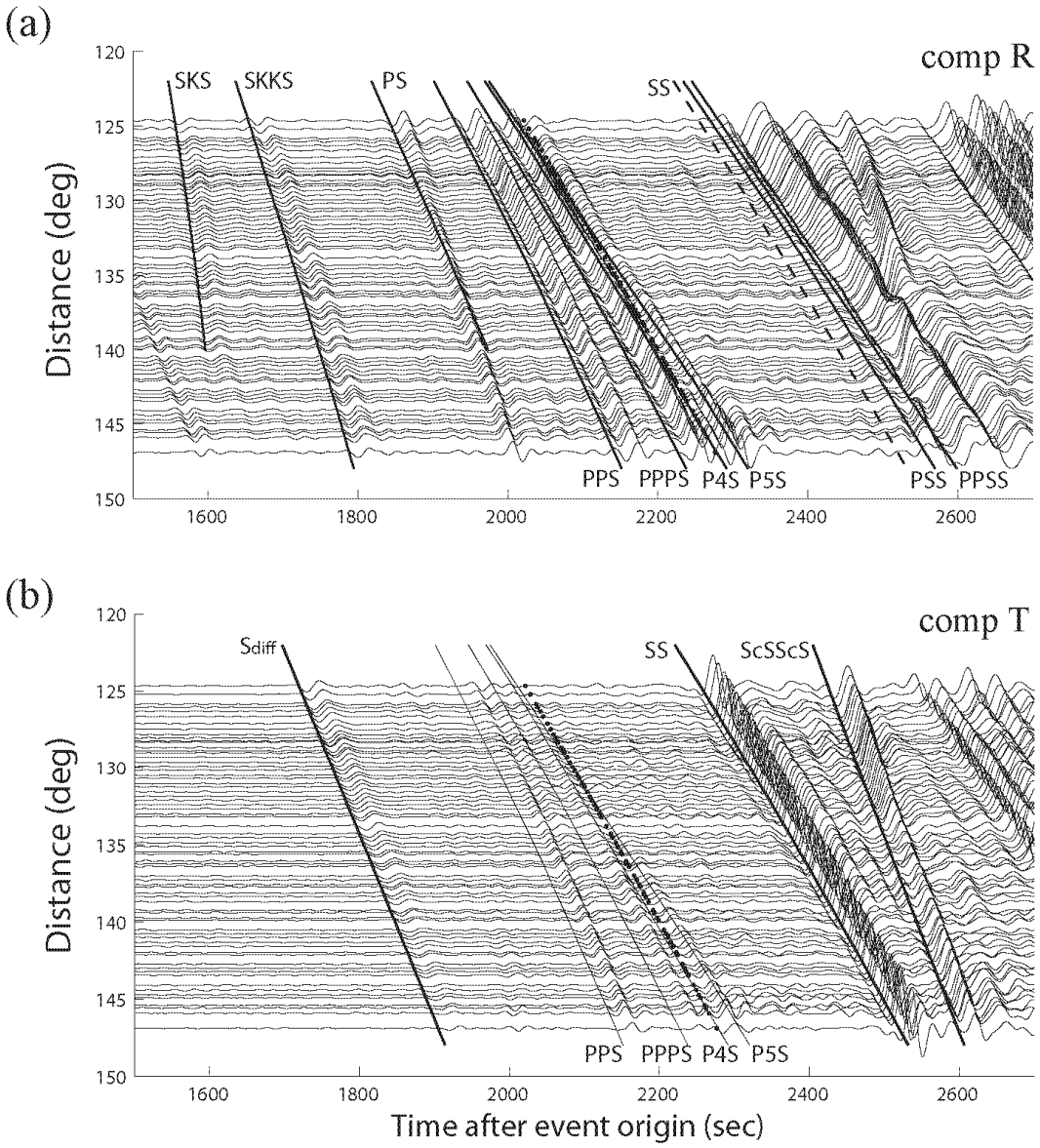

Figure 3.12. Record sections of 3D synthetics on (a) the radial and (b) the transverse components, aligned on the event origin time. Theoretical arrivals of major phases are marked by solid lines. The dotted line indicates the expected $S_{660}S$ arrivals.

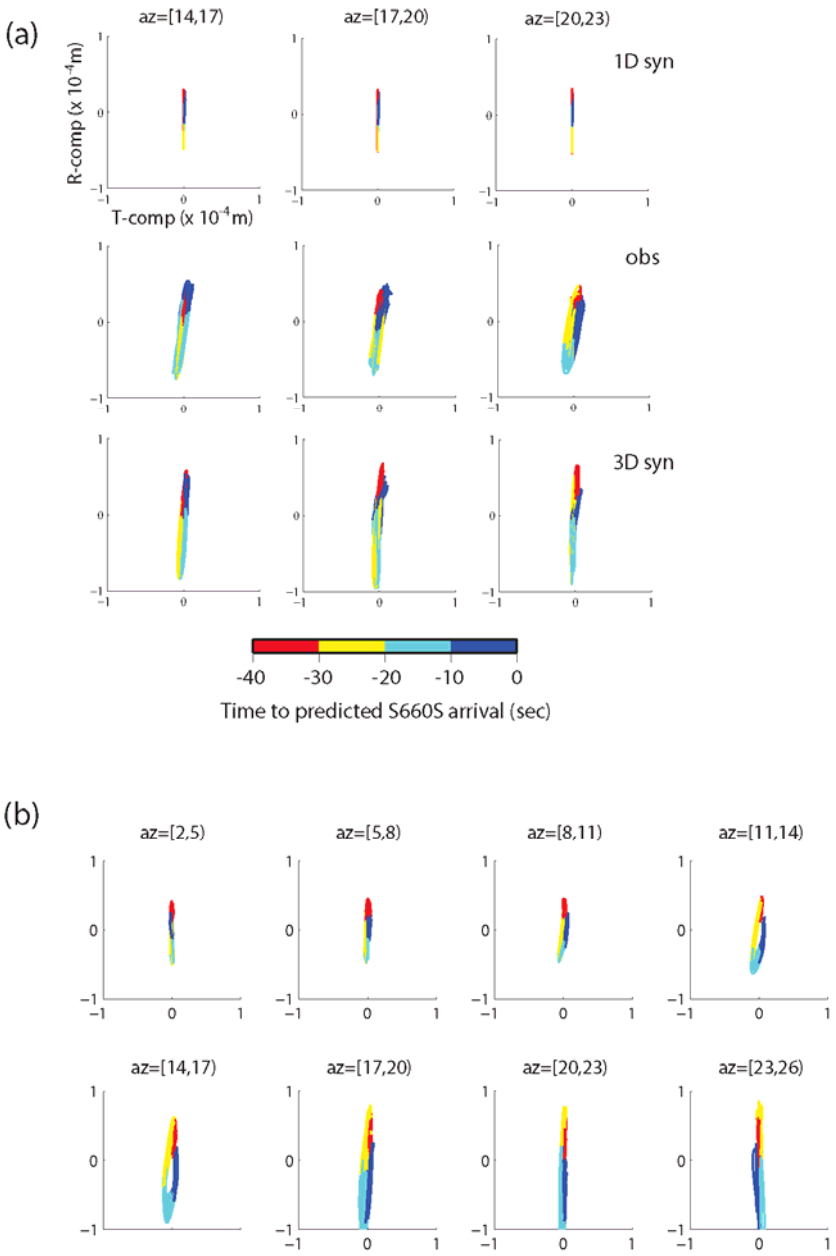

Figure 3.13. (a) Particle motions (radial vs. transverse component displacements) of the 1D synthetics (top row), observations (middle) and 3D synthetics (bottom) in the precursor time window. The colorbar shows time elapsed. Different columns from left to right show results for three different azimuth bins. (b) Particle motions of the synthetics from the 3D model in which the velocity boundary is shifted (Figure 3.10e), arranged by increasing azimuths. The velocity boundary in the model approximately follows the azimuth=14º great circle path.

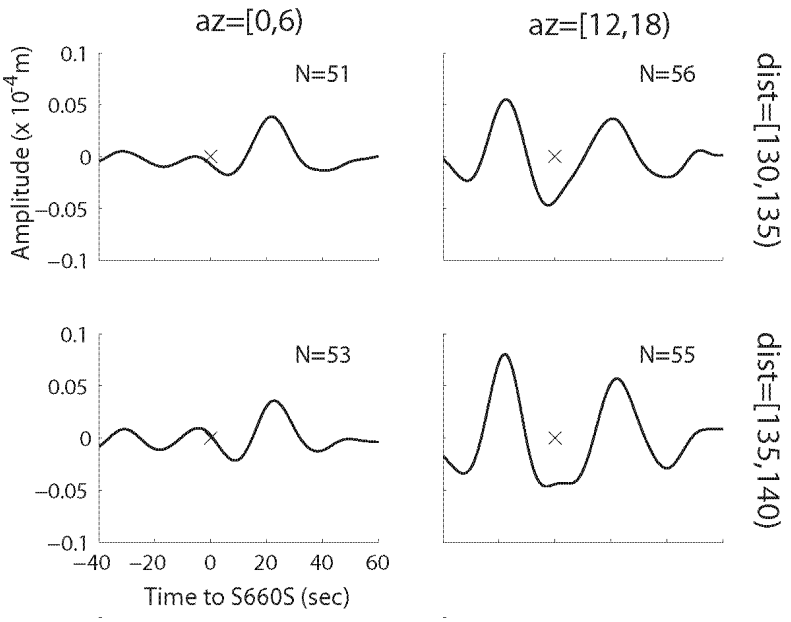

Figure 3.14. Stacks of synthetic seismograms from the 3D model in which the velocity boundary is shifted (see Figure 3.10e), shown for 4 azimuth and distance bins. The cross marks the predicted arrival time of $S_{660}S$ precursor. The number at the top right corner of each panel indicates the number of traces in that stack. When the bin is far away from the velocity boundary, only one precursor with smaller amplitude is seen, whereas when the bin is at or near the boundary, "double precursors" with larger amplitudes are seen. This shows the artificial "precursor" cannot be suppressed by stacking.

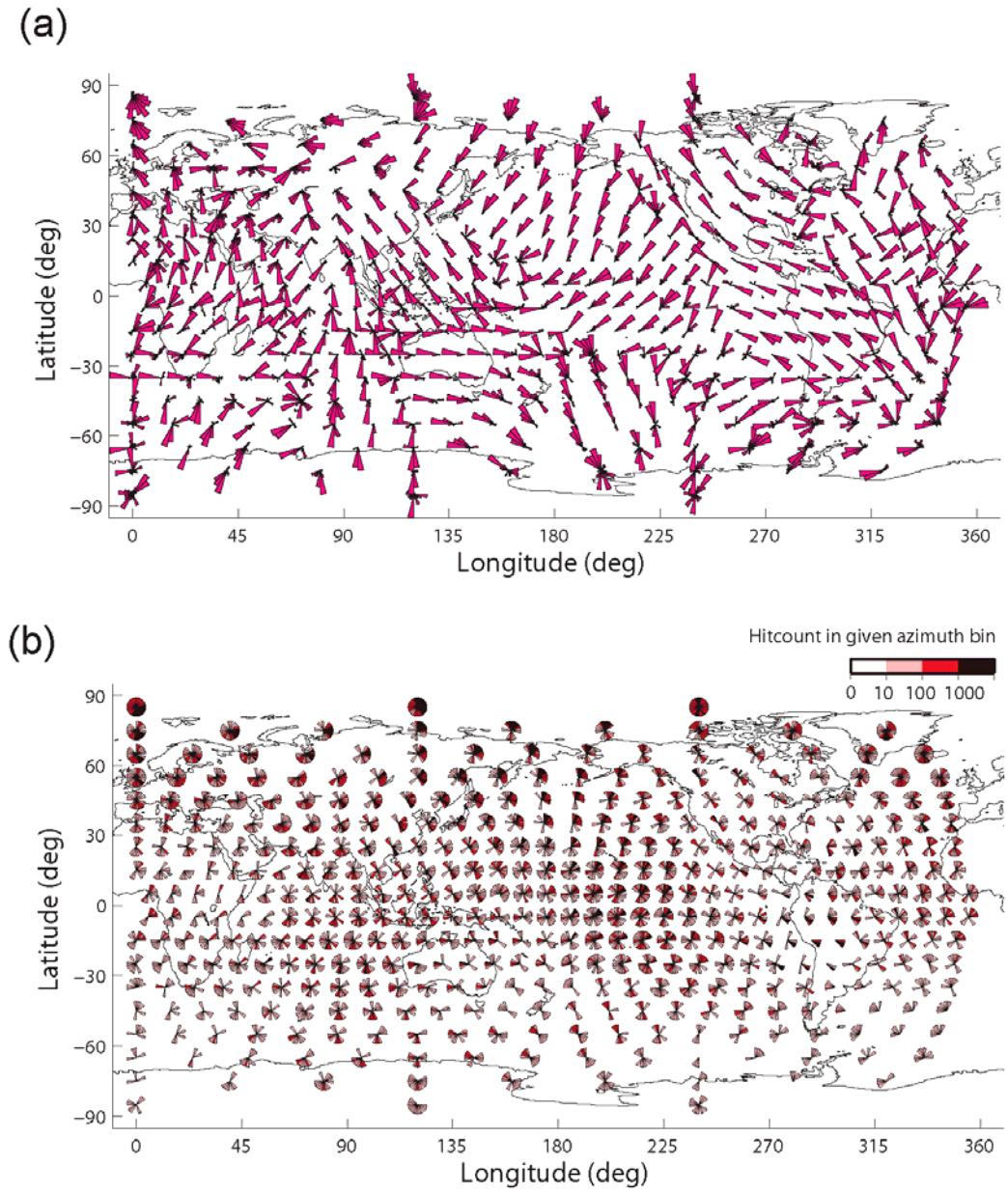

Figure 3.15. "Rose diagrams" (angle histograms) showing the global azimuthal coverage that could possibly be achieved by stacking all SS precursor data before the days of USArray. To compute the raypaths, the earthquakes are all shallow (depth ≤ 75 km) events with $5.8 \leq m_b \leq 7.0$ from the Global CMT catalog from 1976 to 2004, the stations are all seismometers available from IRIS before the deployment of USArray, and the distance range is limited in 100-160º. The globe is subdivided into 412 nearly equal-area, 10º-radius spherical caps for common SS midpoint stack. Within each cap, the 360º azimuth range is divided into 15º bins for plotting the angle histogram. (a) At each spherical cap (i.e. for each "rose"), the radius of each "rose petal" (azimuth bin) is proportional to the number of raypaths sampling that direction, and the maximum radius of each "rose" is normalized to 1. (b) At each spherical cap, all "petals" have a radius of 1, with the darkness of the petal's color indicates the number of traces sampling that direction.

Chapter 4

High Resolution Upper Mantle Discontinuity Images across the Pacific Ocean from *SS* precursors Using Local Slant Stack Filters

4.1 Introduction

In the introduction to Chapter 3, we pointed out the importance of upper mantle discontinuities (410 and 660) for understanding the temperature, composition and dynamics of the Earth's mantle. In recent years, with the improvement in the resolution of global mantle tomography (e.g. *French et al.*, 2013), there has been an increasing demand for higher resolution images of upper mantle discontinuity topography as well, in order to examine possible correlations between the two. However, there have been a few challenges that limit the spatial resolution of the discontinuity images retrieved from the *SS* precursors. First of all, the precursors are weak in amplitude (typically ~5% of the *SS* main phase), often at or below noise level. Therefore it is usually impossible to identify the precursors or make travel time measurements from single seismograms, and stacking is necessary. In practice, common-midpoint (CMP) stacking is employed, i.e. the precursor bounce points are grouped into geographic bins, and all traces within the same bin are stacked together to form one trace, on which the precursors are now evident, and measurements are then made on the stacked trace. As a rule of thumb, the signal to noise ratio (SNR) improvement scales as the square root of the "fold", namely the number of traces in the stack. For *SS* precursors, typically speaking, a fold on the order of 50~100 is required. In the past, due to the sparseness of the global seismic network, rather large geographic bins (typical radius 10°; at best 5°) had to be used for global-scale *SS* precursor studies, (for a review, see *Deuss*, 2009), which greatly limits the spatial resolution. Secondly, the *SS* precursors suffer interference from other seismic phases, such as the postcursors of S_{diff} (or *S* at shorter distances) and the precursors of *ScSScS*. To avoid these interferences, many previous studies have limited the epicentral distance of data selection to the "safe ranges" (for instance, *Schmerr* (2012) uses 95-115° and 140-

145°), although theoretically speaking the entire range of 80-160° contains usable *SS* precursor signals. This has reduced the amount of available data by a significant fraction and may have degraded the sampling density and led to loss of resolution.

The recent deployment of the much denser US Transportable Array (TA) has provided unprecedented opportunities to achieve much higher resolutions for *SS* precursor studies. From 2004 to 2013, ~400 portable broadband seismometers, deployed in a roll-over fashion, swept across the entire conterminous United States, resulting in ~1700 stations in total on a nearly regular grid. The average station spacing of the TA is ~70 km, so as a rule of thumb, the minimum spacing between *SS* bounce points is half of that, i.e. ~35 km. To overcome the above-mentioned limitations that come with the conventional CMP stacking method, here we utilize a new processing tool called the Local Slant-Stack Filters (LSSF), which seeks to maximize spatial resolution by exploiting the advantage of the dense array. In the following sections, we will first introduce the LSSF filters, with examples of application to synthetic and real data to demonstrate the power of the tool. We then apply the filtering method systematically to our *SS* precursor dataset recorded by TA sampling in the Pacific Ocean, and obtain high resolution upper mantle discontinuity images for the region. We compare our images to previous *SS* precursor studies, and discuss the correlation on fine scales between our discontinuity images and a high resolution 3D global mantle tomography model.

4.2 Method

4.2.1 The Local Slant-Stack Filters (LSSF)

Slant stacking (or slowness stacking) is a commonly used tool in seismic array processing. It stacks all traces in a record section along various slownesses in order to find an optimal slowness that maximizes the stacked amplitude (or other measures of coherence). The stacked amplitude versus slowness plot is known as a "vespagram".

The Local Slant-Stack Transform (LSST. *Ottolini*, 1983; *Harlan et al.*, 1984; *Bohlen et al.*, 2004; *Shlivinski et al.*, 2005) is an extension of the simple stacking. As the name suggests, it is a localized version of slant stacking. Figure 4.1 gives an example to show its basic concepts. Instead of stacking all traces across the entire epicentral distance range, it only stacks within a small distance window in the vicinity a given trace. Such localized stacking is then repeated for all traces. Essentially the LSST takes an input record section in the time-space domain and transforms it to the time-space-slowness domain (Figure 4.2). Then in the slowness domain one can design a set of filters to extract only a specific slowness and mask out other undesired slownesses, and then transform back to the time-space domain to obtain a cleaned-up record section, in which only energy of the target slowness is preserved, whereas interfering signals with a distinct

slowness (coherent noise, in other words) and random noise are removed. Readers are referred to *Ventosa et al.* (2012) for mathematical details.

Compared to the simple stacking which uses only one slowness for the entire distance range, the LSSF tracks the local variations of the slowness of the target signal, thus providing more details. In addition, unlike the simple stacking in which only one stacked trace is obtained (and one measurement), the LSSF produces a filtered record section, in which measurements can be made on each trace, therefore significantly improving the spatial resolution (which is still limited by the width of the local slant-stack window). The LSSF filters have been employed in exploration seismology for noise removal, and we recognize they are a suitable tool for our *SS* precursor study as well. In this case, the expected slownesses of the *SS* precursors and the interfering phases are known. Specifically, the *SS* precursors have slownesses that are very close to that of the *SS* (difference < ±0.5 s/deg predicted for *PREM*), while the interfering phases (S_{diff} postcursors and *ScSScS* precursors) have distinctively different slownesses (difference = ~3-4 s/deg), and can therefore be well separated from the *SS* precursors in the slowness domain. We note that the slownesses of the *SS* precursors and those of the interfering phases both vary with epicentral distance, so the LSSF helps to take this variation into account.

One key parameter of choice in designing the LSSF filters is the aperture (bin size) of local slant stacking. To achieve higher spatial resolution, a small aperture is desired. However, a small aperture will smear the slowness resolution, making it more difficult to separate the interfering slownesses from the target slowness on the vespagram. On the other hand, when the aperture is large, the slowness resolution is improved, but the spatial resolution will be degraded. Therefore an intermediate aperture needs be chosen in order to balance the two aspects. The strategy of how to determine an optimal aperture is quantitatively addressed in *Ventosa et al.* (2012).

It is worth pointing out that unlike other non-linear stacking methods such as the phase-weighted stacking or the *n*-th root stacking, the LSSF filtering is a linear process by construction, therefore the amplitude information is preserved. This is essential for reliable estimates of the impedance (the product of seismic velocity and density) and density contrasts across the discontinuities. The density contrast is an important piece of information from the geodynamical perspective. The linearity is also required if one desires to use the precursor waveforms for forward modeling or inversion.

4.2.2 Tests on synthetic and real data

We demonstrate the effectiveness of the LSSF filters by applying them to synthetic and real data. Figure 4.3 shows the results of a test in which we applied the filters to a synthetic record section of *SS* precursors. The locations of source and receivers are from

a real M_w 7.2 earthquake and the TA stations at the time of this earthquake. The epicentral distances range from 120-150°. As shown on the input record section in Figure 4.3(a), in the distance range of 132-145°, the $S_{410}S$ precursor suffers interference from $ScS_{670}ScS$, a precursor to the $ScSScS$, and the interference is very severe in 138-143°, where the two signals are completely entangled. In conventional studies, data in the above-mentioned distance range for this event would have been rejected due to concerns of interference. However, by taking advantage of the different slowness of the two phases, the LSSF filtering is able to extract the target $S_{410}S$ phase and remove the interfering $ScS_{670}ScS$ phase (Figure 4.3b), making the entire distance range available. The waveforms of the $S_{410}S$ precursor for a few traces in 137-139° distance range, in which the interference is the most severe, are somewhat distorted, but the impact on precursor travel time measurement is minor.

Figure 4.4 shows an example of applying the LSSF filters to real data. Figure 4.4(a) shows the record section from an M_w 7.8 earthquake in Samoa recorded at the TA for a specific azimuth window. The *SS* main phase is very clear. However, the *SS* precursors cannot be identified, because they are buried by the strong coda/postcursors following the *S* waves. Given the epicentral distance range (80-96°), the *S* phase is strong, so are its postcursors. In conventional studies, this event would have been rejected. Here we apply the LSSF filters to this record section. Only the signals within the slowness range of ±1 s/deg (with respect to the slowness of *SS*) and are spatially coherent over a radius of 1.5° are preserved. The filtered record section is shown in Figure 4.4(b). The $S_{410}S$ and $S_{660}S$ precursors can now be clearly identified throughout the record section. Their arrival times are in good agreement with the theoretical predictions, confirming the phase identification. To quantitatively demonstrate the improvement of the record section, we compare the travel times of the $S_{660}S$ precursor measured from the record section before and after the LSSF for this event in Figure 4.5. Before the filtering (Figure 4.5a), the travel time measurements are much more scattered, and the slope of the trend is in agreement with the slowness of *S*, indicating the measurements are strongly biased by the *S* postcursors. After the filtering (Figure 4.5b), the measurements are much more coherent, and have the correct travel time and slowness, except for only a few outliers due to cycle skipping in cross correlation. These tests confirm the effectiveness of the LSSF filters.

4.3 Data and processing

4.3.1 The dataset

Here, we systematically apply LSSF to real data recorded by the TA. We collected a dataset from events in the southwestern rim of the Pacific Ocean between January 2004 and December 2013 (the time span of the TA deployment up to date) with the following

criteria: $6.0 \leq M_w \leq 7.5$, depth $\leq$ 75km, $80° \leq \Delta \leq 160°$. These criteria are consistent with previous *SS* precursor studies (e.g. *Schmerr* and *Garnero*, 2006; *Schmerr*, 2012), except we relax the restriction on the epicentral distance range. We look at the transverse component displacement seismograms band-pass filtered in the range 15-75 seconds. For data quality control, we first visually inspect the record sections to make sure the *SS* main phase is strong and clear (not nodal in radiation pattern), the background noise level is reasonably low, etc.; then for the accepted events, we apply an automatic signal to noise ratio threshold on each trace, such that the ratio between the maximum amplitude within the *SS* precursor window and that of the *SS* main phase is less than 1/3, in order to remove the noisy traces. A total of 47 events entered the final dataset. Their *SS* precursor bounce points cover a wide region across the Pacific with high sampling density (Figure 4.6). We then apply the LSSF filters event by event to clean up the record sections. In this study, we intentionally restrict ourselves to single event analysis. As a result, the larger magnitude earthquakes are generally favored due to better signal-to-noise ratio. We do not stack across multiple events in order to avoid the complexity that comes from the variability of source duration, source time function shape, focal depth, etc. across different events, which can greatly distort the stacked waveforms and lead to biased travel time measurements. This is more of a concern because we use larger magnitude events. One way to address the source complexity is to deconvolve the *SS* main phase from the precursor waveforms before stacking (e.g. *Schultz* and *Gu*, 2013a; b).

The aperture of local slant stacking is determined based on the balance between desired spatial resolution and the quality of data. Here in this study, given the typical hitcount density, the signal to noise ratio, and the frequency content of the *SS* precursor signal, we choose an optimal aperture (bin radius) of 1.5°. This value is fixed for all events. A more flexible approach would be to make the bin radius automatically adaptive (e.g. as attempted by *Kim* and *Lawrence*, 2013), to seek even higher resolution in places where the coverage is even denser. It is not implemented here in our study, but we recognize it is worth exploring.

4.3.2 From travel time measurements to discontinuity depth

Differential travel time between the *SS* main phase and a precursor (410 or 660) is then measured using cross correlation from each trace in the LSSF filtered record sections. A time window of [-20, 20] second around the *PREM* predicted arrival time is used for the cross correlation for each target phase, with the exception that a window of [-10, 30] second is used for the 660 precursor, in order to account for the fact that *PREM* assigns a slightly deeper nominal depth of 670 km to the 660-discontinuity.

We calculate corrections for these travel times due to: (1) bathymetry/topography of the free surface, (2) variations in Moho depth and (3) 3D heterogeneities in the mantle. For

bathymetry/topography, we use *ETOPO5* (*Edwards*, 1989) smoothed on a 1x1° global grid. For Moho depth, we use *CRUST1.0* (*Laske et al.*, 2012), which is also gridded 1x1°. For 3D mantle, we use the whole mantle tomographic model *SAW24B16* (*Megnin* and *Romanowicz*, 2000). These travel time corrections are calculated cumulatively along each ray path in the 1D Earth model. For ray tracing, the *TauP* toolkit (*Crotwell et al.*, 1999) is used, and the model is *PREM* (*Dziewonski* and *Anderson*, 1981). The results of these corrections are shown in Figure 4.7. The free surface and crust corrections are on the order of a few seconds mainly within the oceanic regions, and the mantle corrections are on the order of 1-2 seconds. These trends are in good agreement with previous global *SS* precursor studies (e.g. *Bai et al.*, 2012) as well as a regional scale study for the central Pacific (*Schmerr* and *Garnero*, 2007). The mantle corrections here are generally small, due to the fact that the tomography model *SAW24B16* is fairly smooth. Another point to keep in mind is that here we use 1D ray tracing, implying the assumption that the ray paths of *SS* and the precursors are not perturbed by 3D heterogeneity, which is only true to first order. In reality, large scale heterogeneities can alter the ray paths and result in larger travel time perturbations in certain cases.

After the above corrections are properly applied, the precursor travel time measurements are then converted to discontinuity depths at the bounce point for each ray path. A velocity model is needed for the time to depth conversion; here we use *PREM*. After the measurements from each point have been obtained, they are then combined to form a map of discontinuity topography for the study region.

4.4 Results and discussion

In this section, maps of 410 and 660 discontinuity depths are presented. We remind the readers that in the simplest case where the discontinuity depth change is purely caused by a thermal anomaly, a cold anomaly (e.g. subducted slab) will result in an uplifted 410 and a depressed 660, while a warm anomaly (e.g. upwelling) will cause a deepened 410 and a shallower 660. The color convention of our discontinuity topography maps will reflect this thermal-origin assumption. We also note that there may exist other complication factors besides the simple thermal interpretation, such as compositional anomaly, and/or the effect of remaining 3D volumetric heterogeneities that are not fully accounted for by the travel time corrections described in the previous section.

4.4.1 The 410 discontinuity

Figure 4.8(a) shows a map of the 410 discontinuity depth. Warm colors represent a longer *SS*-$S_{410}S$ differential travel time, or equivalently, an apparently deeper 410, suggesting a warm anomaly if explained by temperature effect on the olivine phase transformation alone. Cold colors, on the contrary, indicate a shorter *SS*-$S_{410}S$ time, or an apparently

shallower 410, suggesting a presumably cold anomaly. Overall the 410 discontinuity does not show large topography. A few warm anomalies are seen on the map (circled out and labeled "A", "B" and "C" on Figure 4.8a), with different size and strength. The locations of these anomalies are in good agreement with a few low velocity columns penetrating the 410 discontinuity as revealed by the very recent high resolution upper mantle tomography model, *SEMum2* model (*French et al.*, 2013), as shown in Figure 4.8 (b) and (c). These low velocity columns are explained as hot material rising from the lower mantle, which is in agreement with the warm anomaly revealed by the 410 discontinuity topography map. It is remarkable that not only the locations, but also the horizontal extent and the strength of the anomalies are in good agreement from the 410 topography and the tomography. This shows that our method and data are capable of imaging the fine-scale features of the upper mantle discontinuity. The strong correlation between the 410 topography and tomography suggests that there could still be some trade-offs between the discontinuity depth and the volumetric heterogeneity.

4.4.2 The 660 discontinuity

Figure 4.9 shows a map of the 660 discontinuity depth. Warm colors represent a shortened (contrary of the convention used for 410) *SS*-$S_{660}S$ differential travel time, or equivalently an apparently shallower 660 consistent with a warm temperature anomaly. Cold colors, on the other hand, suggest a cold anomaly.

Overall the 660 discontinuity shows larger magnitude of topography than the 410. The depth of the 660 is depressed in the subduction zones (colder) at the northwestern rim of the Pacific Ocean, and uplifted in the oceanic regions, which is in agreement with previous global *SS* precursor studies (e.g. *Gu et al.*, 2003, *Lawrence* and *Shearer*, 2008; *Houser et al.*, 2008; *Deuss*, 2009; *Houser et al.*, 2010).

One striking feature is an area of extremely warm color to the east of Hawaii. This area is sampled by 3 events (Figure 4.10a) in our dataset, and all 3 events give consistent results. Depth cross sections from a recent global shear velocity tomography model are constructed to explore possible cause of the discontinuity anomaly. The model we use is a most recent whole mantle tomography model (*French*, 2014), which is an extension to the whole mantle of the upper mantle model *SEMum2*. In Figure 4.10 (b), a section of the profile A1-A2, which is along the great circle path of a representative ray path is shown, and in (c), a section of the profile B1-B2, which is perpendicular to the ray path. A prominent feature is the long section is the upwelling "plume" beneath Hawaii. It originates from the lower mantle, rises almost vertically with a slight tilt toward the east of Hawaii up to ~1000 km depth, then swings and stretches westward at shallow depths up to ~400 km. The ray path of the $S_{660}S$ precursor travels along the eastern boundary of the low velocity anomaly for a fairly long distance, whereas the path of the $S_{400}S$

precursor and the *SS* phase travels through a high velocity anomaly above the low velocity stretch. This would yield a delayed $S_{660}S$ absolute travel time and advanced $S_{410}S$ and *SS* times. Since differential travel time is used instead of absolute travel time, this will lead to a more or less normal *SS*-$S_{410}S$ differential travel time, and a significantly longer *SS*-$S_{660}S$ time, and when converted from time to depth, an apparently normal 410 depth and a significantly shallower or "warmer" 660 depth, which agrees very well with what is observed on our discontinuity maps in Figure 4.9 and 4.8 as well as on the record section of this event shown in Figure 4.11. This gives us confidence in interpreting the detailed features we see on the discontinuity images. In addition, we notice from the cross section in Figure 4.10 that the upwelling seems to be less continuous at ~1000 km depth. If this is true, then it will enhance the velocity contrast across this depth and may produce an observable *SS* precursor signal. Indeed, from the filtered record section shown Figure 4.11, an additional precursor signal is observed, corresponding to a depth of roughly 900 km. The amplitude of this precursor is weaker than those of the 660 and 410 precursors, which is expected because of smaller velocity contrast. This is one case where the *SS* precursor study serves as an independent observation to confirm the fine-scale features imaged by tomography.

4.5 Conclusions

We present high resolution topography images of the 410 and 660 discontinuities for a vast region across the Pacific Ocean measured from *SS* precursors. The high quality and density of US Transportable Array data in combination with a new data processing technique, namely the Local Slant Stack Filters (LSSF), in combination has allowed for unprecedented image resolution. We observe intriguing correlations between the fine-scale features in our discontinuity images and the heterogeneities seen by high resolution global mantle tomography models.

The LSSF is a powerful tool for cleaning up *SS* precursor record sections. It enables us to remove interfering seismic phases as well as random noise and extract the weak yet coherent SS precursor signals, yielding reliable precursor travel time measurements from single traces within an array, which significantly improves the resolution of upper mantle discontinuity topography maps compared to conventional CMP (common midpoint) stacking method. We recognize that the cleaned record sections can also be used as input data for other array imaging techniques such as migration (e.g. *Thomas* and *Billen*, 2009; *Schmerr* and *Thomas*, 2011), or used for a joint inversion along with tomographic data to simultaneously constrain volumetric velocity anomaly and discontinuity topography (e.g. *Gu et al.*, 2003; *Houser et al.*, 2008). It is worth pointing out that the LSSF filtering is a linear process by construction, so the amplitudes of the precursors are preserved, which is essential for reliable estimates of the impedance (and density) contrast across the discontinuities.

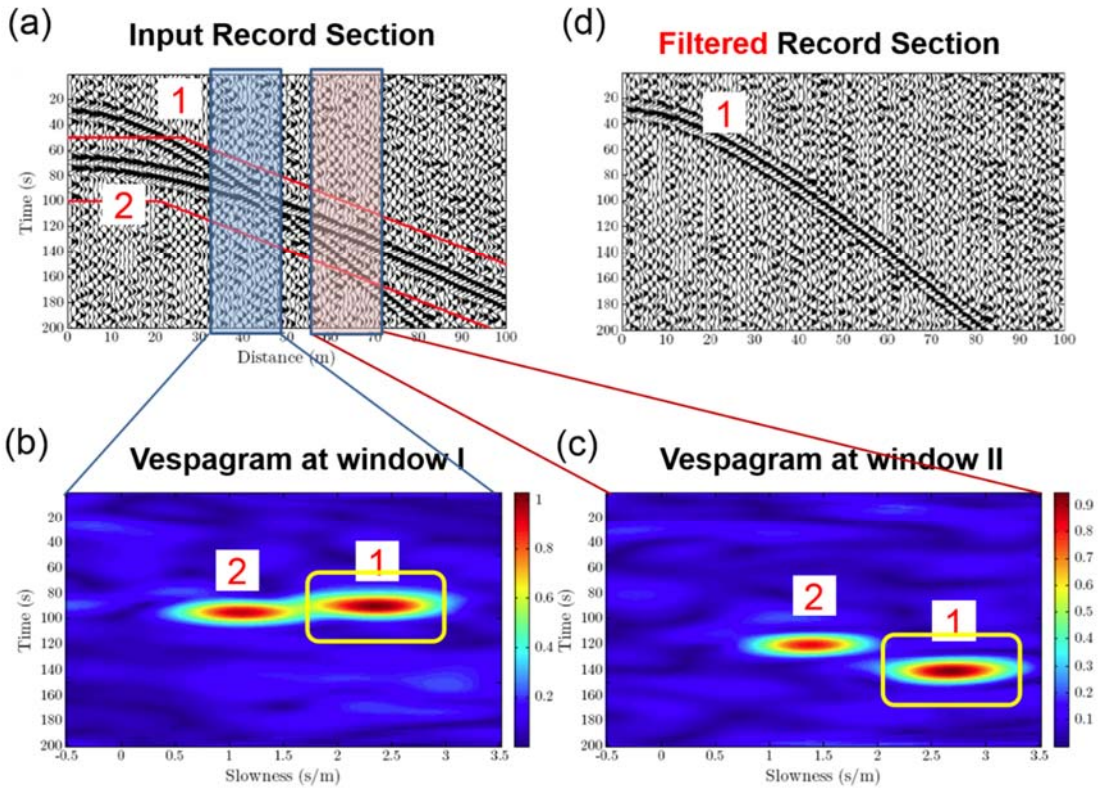

Figure 4.1. An example from exploration seismology to demonstrate the basic concept of the Local Slant-Stack Filters (LSSF). (a) Input record section containing two coherent signals marked "1" and "2" interfering with each other. (b) and (c) Vespagrams for two spatial windows around distances of 40 m and 60m, respectively. The difference in the slowness of the two signals "1" and "2" is revealed. The yellow box shows one can choose to extract signal "1" and remove "2" in the slowness domain. (d) After returning to the time domain, a cleaned record section is obtained with only signal "1" preserved.

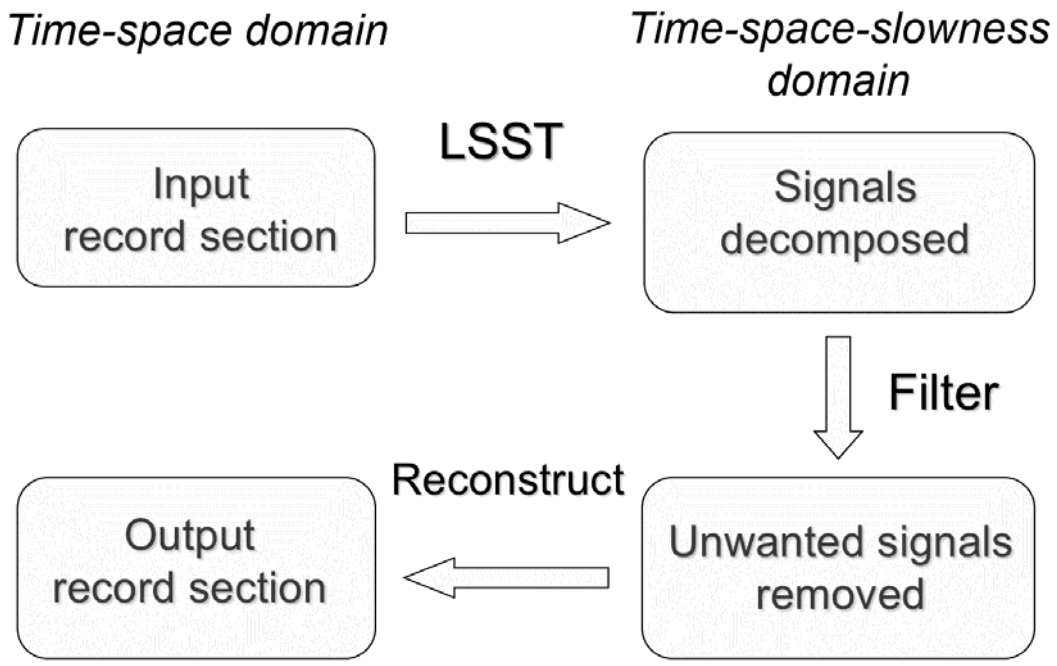

Figure 4.2. A summary of the workflow of the LSSF filtering. The left column shows time-space domain, and the right column the time-space-slowness domain. In the slowness domain, one can design filters to remove signals with undesired slownesses (in other words, coherent noise), as well as random noise.

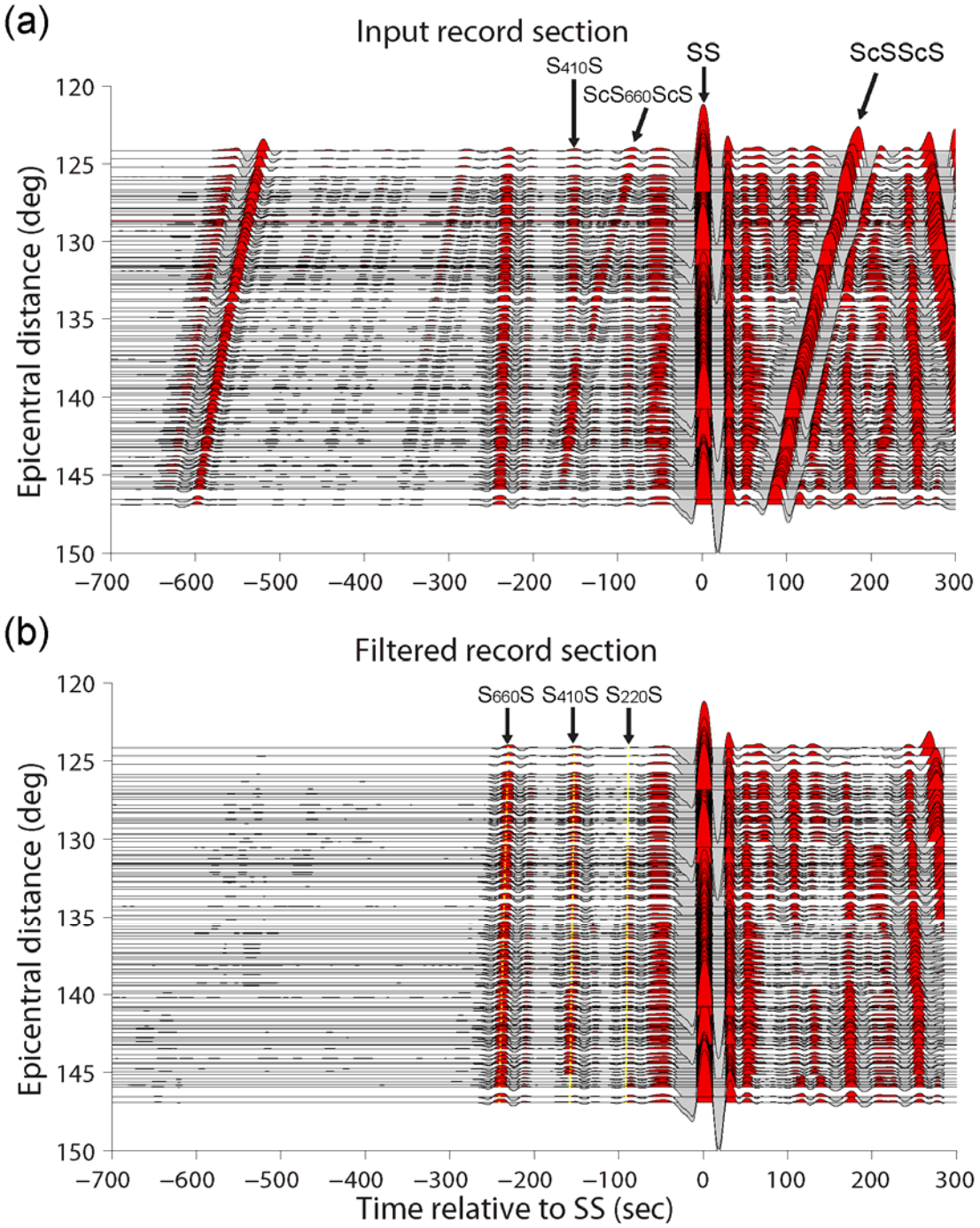

Figure 4.3. An example of applying the LSSF filters to a synthetic record section. The 1D synthetic seismograms are computed for the *PREM* model using normal mode summation. (a) Input record section; (b) filtered record section. The seismograms are aligned on the *SS* main phase, arranged by epicentral distance. Yellow dotted lines indicate theoretical arrival times of the SS precursors calculated for the *PREM* model using the *TauP* toolkit (*Crotwell et al.,* 1999).

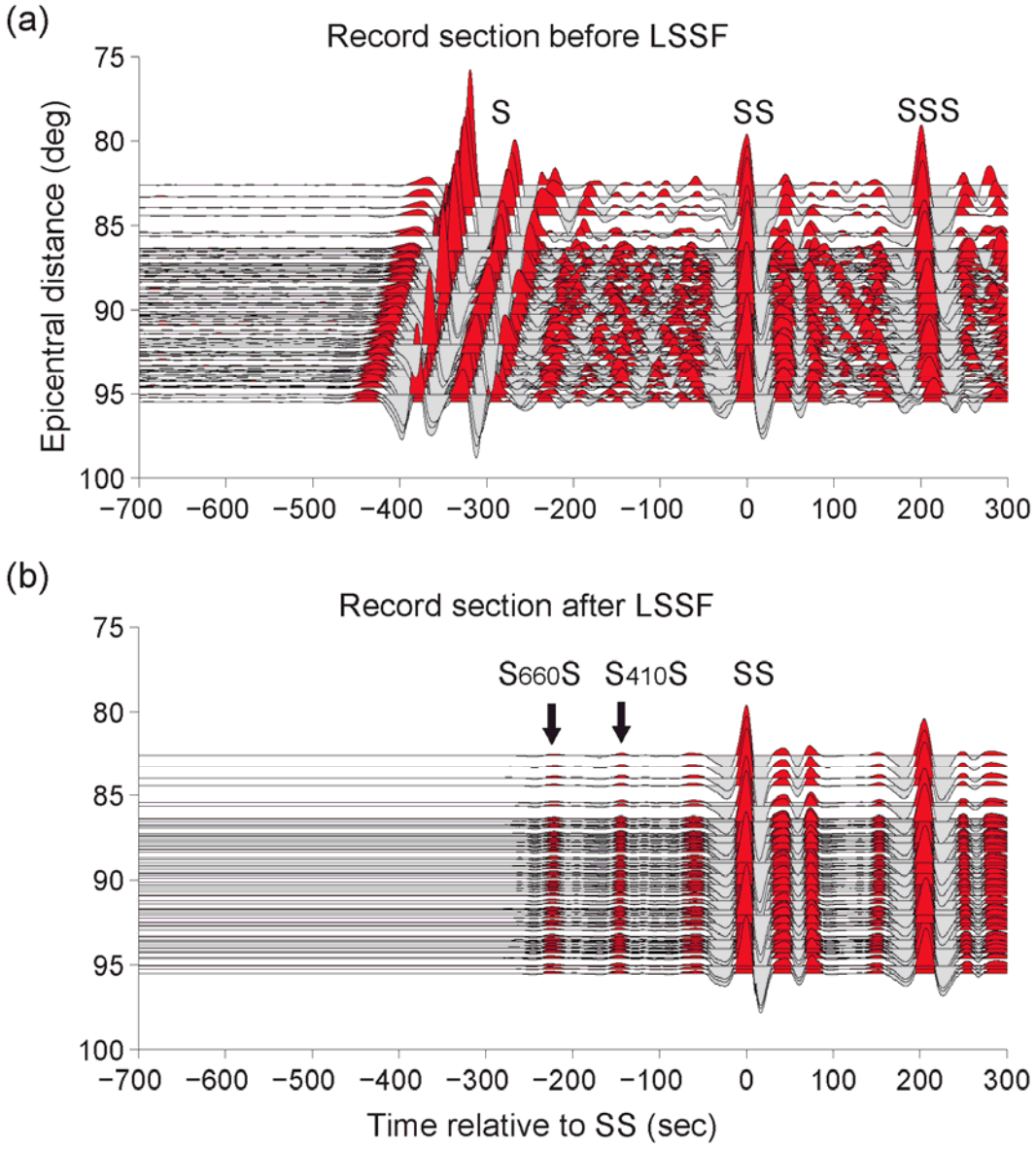

Figure 4.4. An example of applying the LSSF filters to an observed record section. The seismograms are aligned on the *SS* main phase. (a) Input record section; (b) filtered record section.

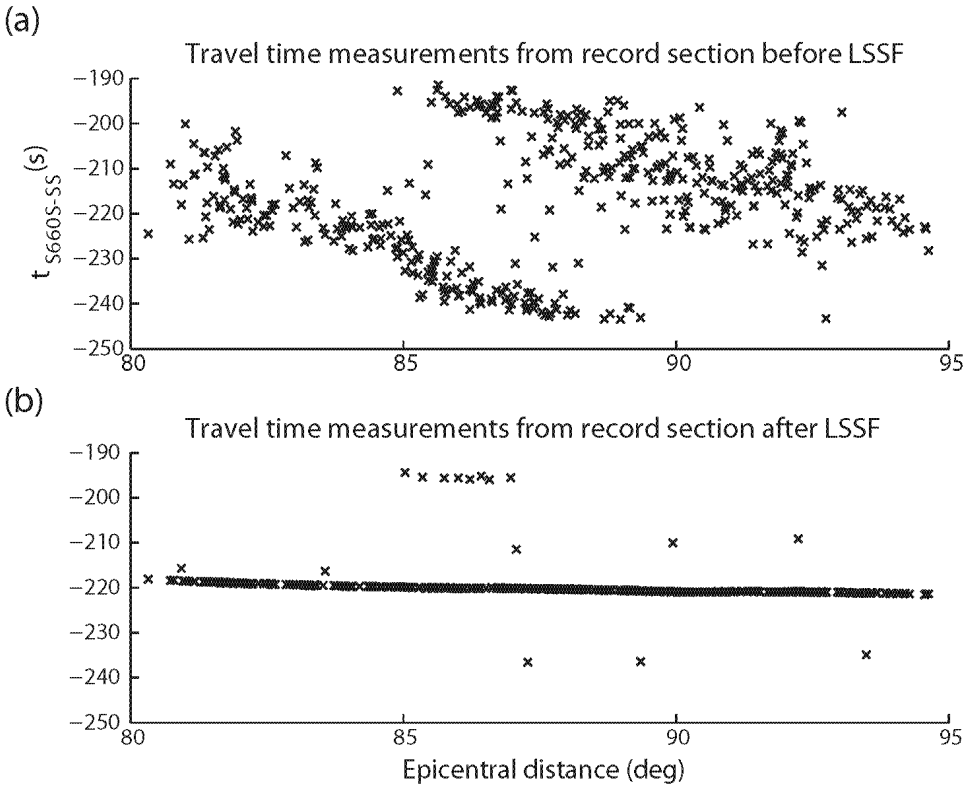

Figure 4.5. Differential travel times of $S_{660}S$-SS measured from the input and filtered record sections shown in Figure 4.4. The travel times are measured by cross-correlation between the $S_{660}S$ and SS waveforms.

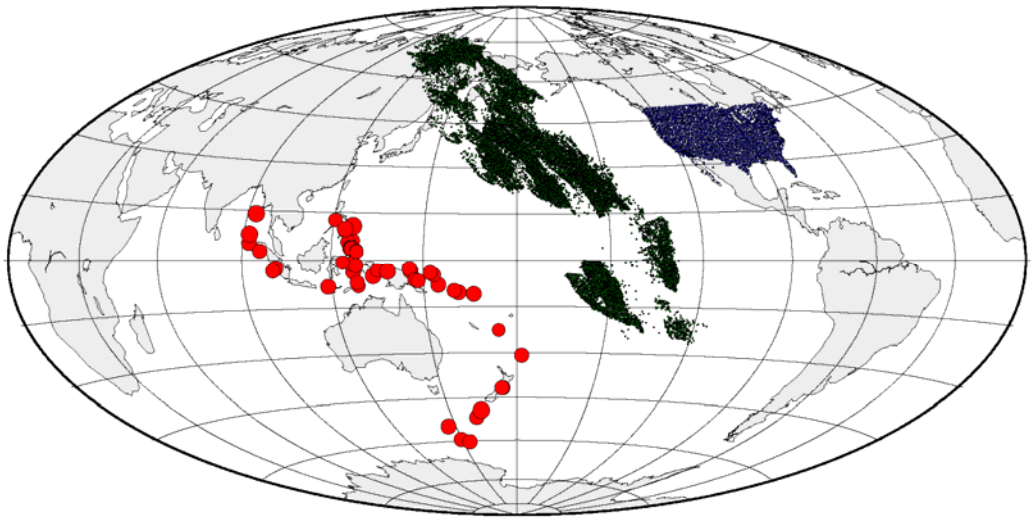

Figure 4.6. A map showing the dataset of 47 earthquakes with high-quality SS precursor record sections recorded by the US Transportable Array. The source locations are shown by red circles, the stations by blue triangles, and the SS bounce points by dark green dots.

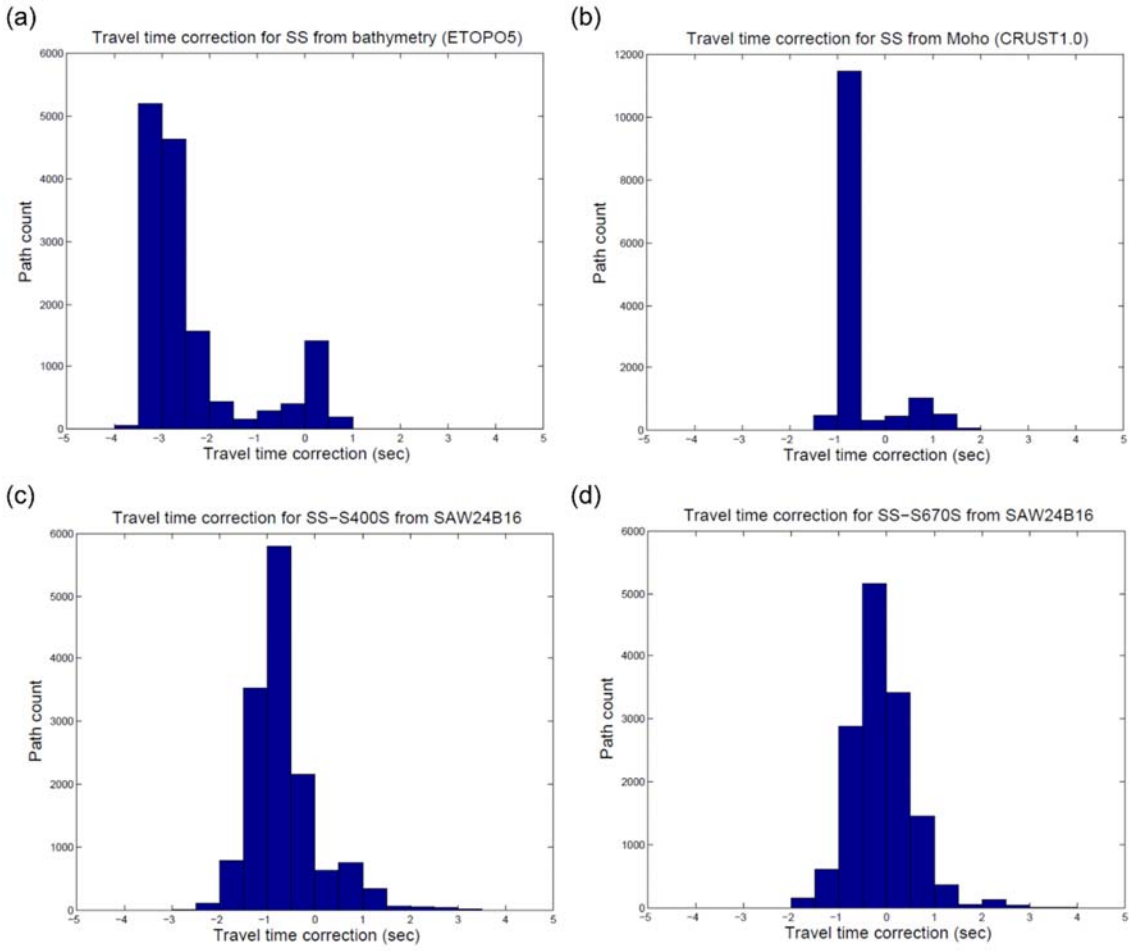

Figure 4.7. Corrections to *SS* and the precursor travel times due to (a) surface topography/bathymetry, (b) variation in Moho depth, (c) and (d) 3D velocity structure in the mantle. For topography/bathymetry, *ETOPO5* (*Edwards*, 1989) model is used. For Moho depth, *CRUST1.0* (*Laske et al.*, 2012) model is used. For 3D mantle structure, the shear velocity tomography model *SAW24B16* (*Megnin* and *Romanowicz*, 2000) is used.

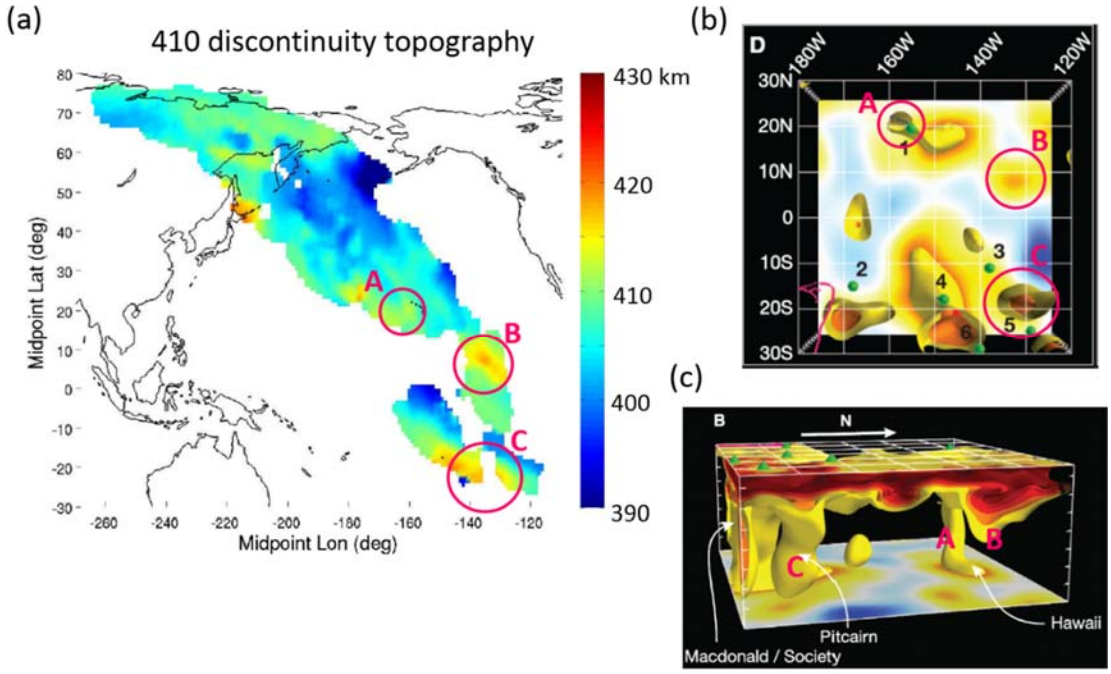

Figure 4.8. (a) A map of the 410 discontinuity topography converted from precursor travel times. Warm colors represent longer *SS*-$S_{410}S$ differential travel time, or equivalently, an apparently deeper 410, suggesting a warm anomaly if explained by temperature effect alone on the olivine phase transformation. Cold colors, on the contrary, indicate a shorter *SS*-$S_{410}S$ time, or an apparently shallower 410, suggesting a cold anomaly. (b) and (c) Tomographic images from *SEMum2* model (*French et al.*, 2013) for the region shown in (a) as a dashed box. Low shear velocity (>2% V_s reduction) bodies are shown in yellow, which are explained at least partially as a warm temperature anomaly. The 3 circled areas labeled A, B and C show geographic locations at which both a "warm" anomaly in the 410 topography and a slow velocity anomaly in the tomography model are observed.

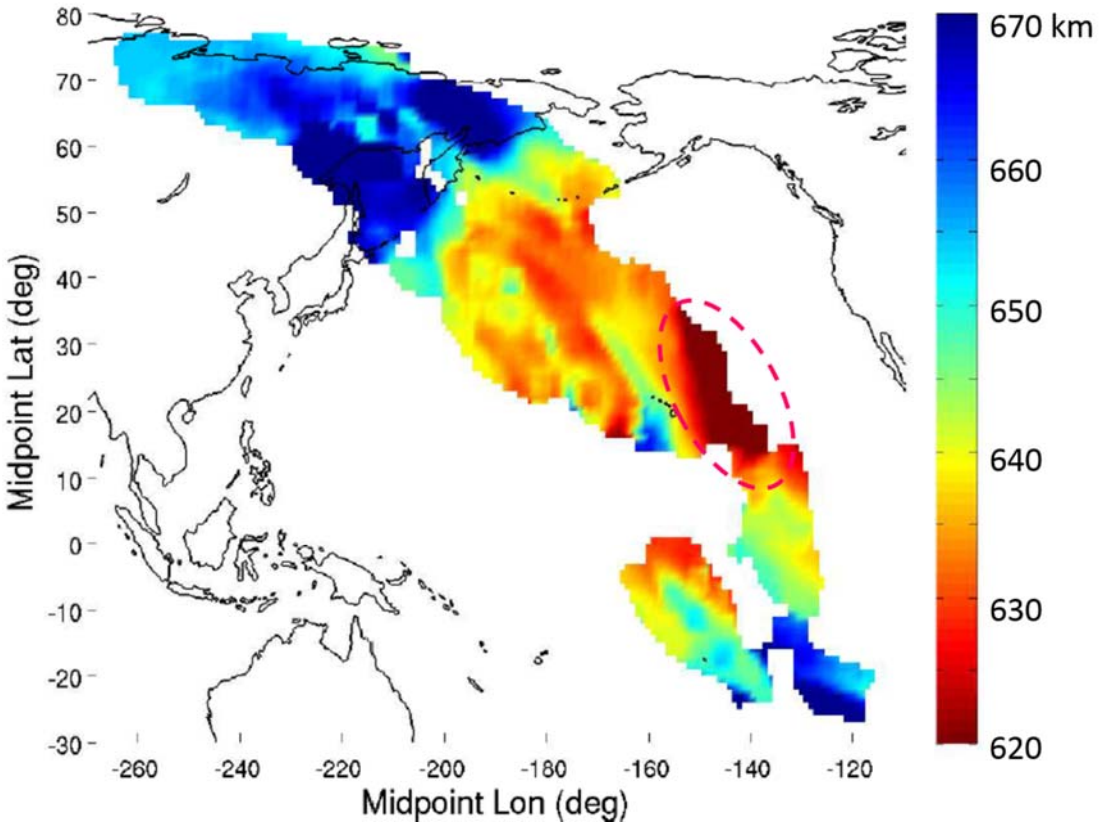

Figure 4.9. A map of the 660 discontinuity topography in the study region. The dashed oval outlines an anomalous area to the east of Hawaii, which shows significantly shorter *SS*-$S_{660}S$ differential travel times.

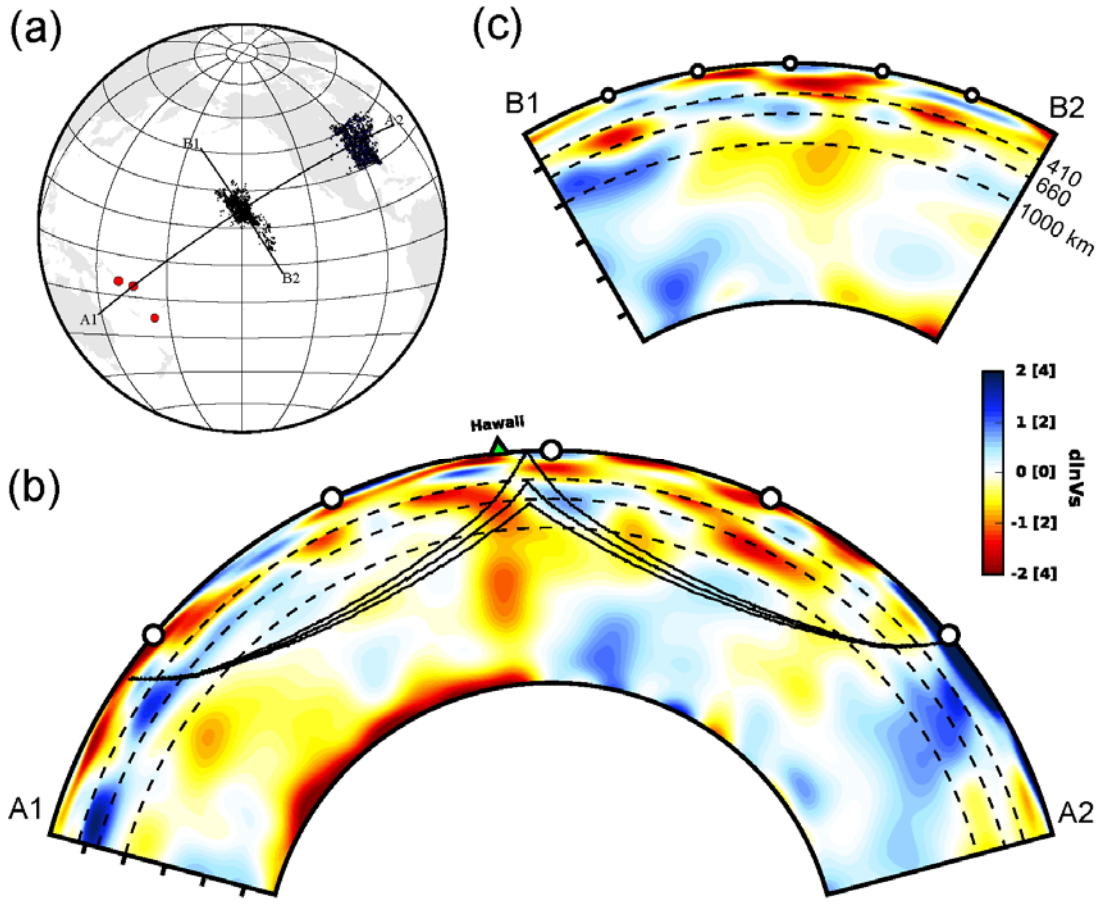

Figure 4.10. (a) A map showing the 3 events that sample the anomalous area outlined in Figure 4.9. The event locations are shown by red circles, the stations by blue triangles, and the *SS* bounce points by green dots. (b) Cross section along the great circle plane A1-A2, of a very recent whole mantle shear velocity tomography model by *French* (2014), which is an extension of the upper mantle model *SEMum2* (*French et al.*, 2013) to the whole mantle. The ray paths of the *SS* and its precursors are shown. (c) Cross section along Profile B1-B2, which is perpendicular to Profile A1-A2.

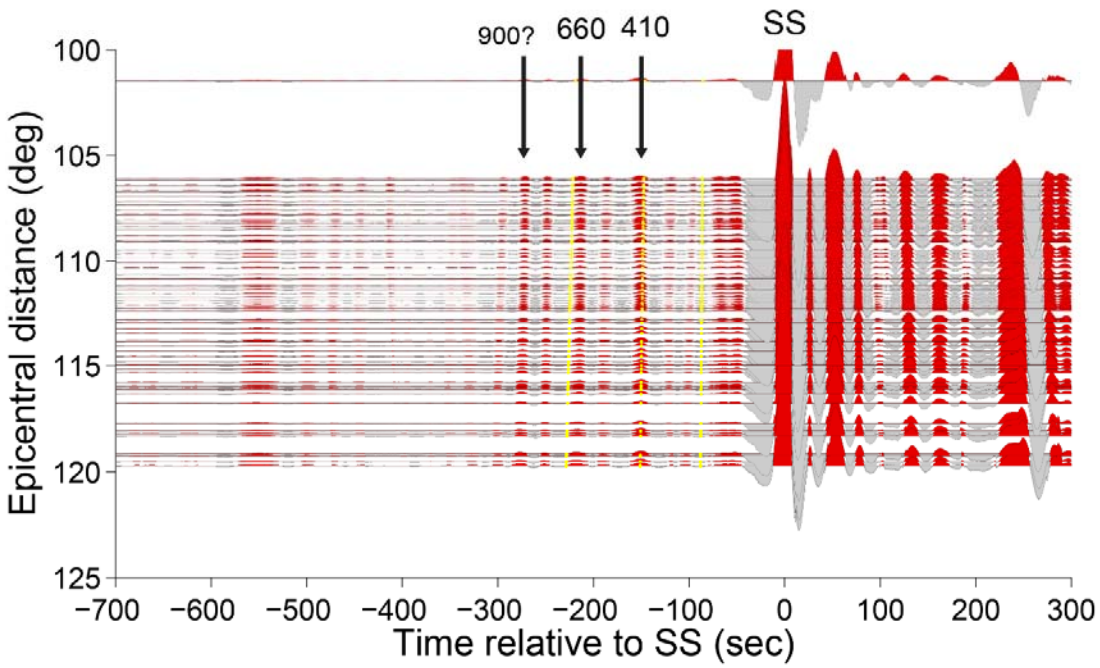

Figure 4.11. Filtered record section from the event in Figure 4.10(a) cut through by profile A1-A2. The waveforms are aligned on *SS*. The yellow dotted lines indicate theoretical arrival times of the SS precursors calculated for *PREM*. The $S_{660}S$ precursor arrives later than the *PREM* prediction, indicating an apparently shallower 660 discontinuity. In addition to the expected 410 and 660 precursors, there exists another precursor which corresponds to a discontinuity at ~900 km depth.

Chapter 5

Toward a Hybrid Adjoint Tomography for the North American Upper Mantle

5.1 Introduction

The deployment of the US Transportable Array (TA) has provided dense array coverage and unprecedented opportunity for imaging the crust and upper mantle of North America (NA). The Berkeley Global Seismology group has been utilizing high-quality waveform data from the TA to produce continental-scale shear velocity and anisotropy models for the region (*Yuan* and *Romanowicz*, 2010; *Yuan et al.*, 2011; *Yuan et al.*, 2013). Seismic tomography in general consists of three pieces: the forward modeling (i.e. for a given model, calculating the synthetic data -- in this case the seismic waveforms), the computation of sensitivity kernel (or the functional derivative of data with respect to model) and the inversion (i.e. solving for an update to the current model in order to minimize the misfit between the data and the prediction). In the earlier works (*Yuan* and *Romanowicz*, 2010; *Yuan et al.*, 2011, as well as *Marone et al.*, 2007, a first generation NA tomographic model prior to the deployment of TA), the Non-linear Asymptotic Coupling Theory (NACT; *Li* and *Romanowicz*, 1995; 1996) was employed for both forward modeling and the computation of sensitivity kernels. In the latest study (*Yuan et al.*, 2014), in the forward modeling part, the approximate NACT method is replaced by the numerically accurate Regional Spectral Element method (*RegSEM*; *Cupillard et al.*, 2012), at the price of much higher computational cost, while the kernels are still computed with NACT, making it a hybrid approach. In all these studies, a Gauss-Newton (GN) scheme is used to solve for model updates. Specifically, the *normal equation*

$$(A^T A)\delta m = A^T \delta d \tag{5.1}$$

is solved to obtain

$$\delta m = (A^T A)^{-g}(A^T \delta d) \tag{5.2}$$

with δm being the model update, δd = || d - $f(m)$ || the data residual (f the forward operator), A the sensitivity kernel, and "-g" denotes generalized matrix inverse.

For global and continental scale waveform tomography, it is still numerically very challenging to conduct the tomography entirely numerically. On the continental scale, there have been attempts of fully numerical implementations (e.g. *Fichtner et al.*, 2009; *Zhu et al.*, 2012; 2013) based on the adjoint method. The adjoint method (*Tarantola*, 1984; *Tromp et al.*, 2005) states that the sensitivity kernel can be constructed by convolving the forward wavefield and the adjoint wavefield (with the adjoint source formed from data residual). Instead of inverting the normal equation, these implementations have employed gradient methods such as the conjugate gradient method (CG) to directly estimate model updates. Since CG only takes into account the gradient (first-derivative) of the misfit function, it converges much more slowly than the GN scheme, which utilizes the (approximate) Hessian A^TA (second-derivative of the misfit function) – more details are explained in Section 5.2. For example, *Zhu et al.* (2012), an adjoint tomography for Europe, required more than 30 iterations, which is computationally very heavy, whereas the GN scheme typically requires only a few iterations to converge.

In this chapter, we propose a framework of a hybrid adjoint tomography based on the Gauss-Newton scheme. In this framework, the gradient of the misfit function $A^T\delta d$ (the right-hand side of the normal equation (5.1)) is computed based on the adjoint method with the numerical code *RegSEM*, while the sensitivity kernel A and the approximate Hessian A^TA (the left-hand side of the normal equation) are still computed approximately with NACT. *Lekic* and *Romanowicz* (2011) have argued that accurate computation of the forward wavefield is more important than that of the sensitivity kernels, for which error is of second order, and which can therefore be computed approximately, as long as the starting 3D model already contains the salient long wavelength features of the model. The model update δm is then obtained by solving the normal equation (5.1). This hybrid adjoint tomography framework is one step forward from the hybrid tomography framework in *Yuan et al.* (2013), in which only $f(m)$, and thus $\delta d = \| d - f(m) \|$, is computed numerically, and then δd is multiplied by the sensitivity kernel A computed approximately with NACT to obtain the right-hand side of the normal equation.

5.2 Theoretical framework

5.2.1 The misfit function and the normal equation

In the context of waveform tomography, the misfit function to be minimized is:

$$\Phi(m) = \frac{1}{2}\sum_i ||d_i - f_i(m)||^2 \tag{5.3}$$

where d_i are the data (seismic waveforms), and $f_i(m)$ the prediction of data for model m.

If the misfit function is expanded in Taylor's series around the starting model m_0, and truncated to the second order, one finds:

$$\Phi(m) = \Phi(m) + \frac{\partial \Phi}{\partial m}(m_0)(m - m_0) + \frac{1}{2}(m - m_0)^T H(m_0)(m - m_0) \tag{5.4}$$

where H is called the Hessian, which is the matrix form of second-order derivative of $\Phi(m)$ with respect to m:

$$H(m) = \frac{\partial^2 \Phi}{\partial m^2} \tag{5.5}$$

and

$$\frac{\partial \Phi}{\partial m}(m_0) = -\left[\frac{\partial f}{\partial m}\ (m_0)\right]^T\ (d - f(m_0)) \tag{5.6}$$

is the gradient of the misfit function. One can denote

$$\frac{\partial f}{\partial m}(m_0) = A \tag{5.7}$$

The minimum of $\Phi(m)$ is found at model m such that

$$\nabla_m\big(\Phi(m)\big) = \frac{\partial \Phi}{\partial m}(m_0) + H(m_0)(m - m_0) = 0 \tag{5.8}$$

Thus

$$H(m) = \frac{\partial^2 \Phi}{\partial m^2}(m_0) = A^T A + \left[\frac{\partial A}{\partial m}\ (m_0)\right]^T\ (d - f(m_0)) \tag{5.9}$$

In general practice, the second term of the Hessian is often neglected. This is justified when the residual d - $f(m)$ is small and/or the problem is only weakly non-linear (i.e. $\frac{\partial A}{\partial m}$ is small). The approximate Hessian is then

$$H(m) \approx A^T A \tag{5.10}$$

and Eq. (5.8) gives the Gauss-Newton normal equation:

$$A^T A(m - m_0) = A^T\,(d - f(m_0)) \tag{5.11}$$

which is exactly the same as Eq. (5.1).

5.2.2 The adjoint method

Instead of solving the normal equations, the adjoint method directly linearizes the misfit function with respect to the model perturbation δm around the starting model m_0:

$$\Phi(m) = \int K(\boldsymbol{x})\delta m(\boldsymbol{x})dV \tag{5.12}$$

where $K(\boldsymbol{x})$ is called the Frechet kernel and is evaluated at the starting model m_0.

Tromp et al. (2005) demonstrated for the case of travel time tomography as well as waveform tomography that the Frechet kernels can be expressed as a time-integrated product between spatial and temporal derivatives of the forward wavefield $\boldsymbol{s}$ and the time-reversed adjoint wavefield $\boldsymbol{s}^+$. For instance, in the case of waveform tomography, the Frechet kernel with respect to the perturbation in the density ρ and the elastic tensor C_{jklm} are:

$$K_\rho(\boldsymbol{x}) = -\int_0^T \rho(\boldsymbol{x})\,\partial_t^2 \boldsymbol{s}(\boldsymbol{x},t)\;\boldsymbol{s}^+(\boldsymbol{x},T-t)\;dt \tag{5.13}$$

$$K_{C_{jklm}}(\boldsymbol{x}) = -\int_0^T \varepsilon_{lm}(\boldsymbol{x},t)\,C_{jklm}(\boldsymbol{x})\,\varepsilon^+_{\boldsymbol{jk}}(\boldsymbol{x},T-t)\;dt \tag{5.14}$$

where $\boldsymbol{\varepsilon}$ denotes the strain tensor.

The adjoint wavefied is obtained by solving the wave equation that governs the forward wavefield, except that the source term is replaced by the adjoint source, which is formed by the waveform residuals summed over all receivers:

$$f_i^+(\boldsymbol{x},t) = \sum_{r=1}^{N_r} (\boldsymbol{s}(\boldsymbol{x},T-t) - \boldsymbol{d}(\boldsymbol{x},T-t))\ \delta(\boldsymbol{x}-\boldsymbol{x}_r) \tag{5.15}$$

with r is the index for receivers, and $\boldsymbol{s}$ and $\boldsymbol{d}$ denote the synthetic and observed seismograms, respectively.

In the implementation of *Tromp et al.* (2005), three simulations are required to obtain the Frechet kernel: one forward simulation to produce synthetic seimograms in order to form the adjoint source as in Eq. (5.15), then a second simulation (time-reversed) to generate the adjoint wavefield, and a simultaneously forward simulation (the third simulation) to reproduce the forward wavefield in order to convolve with the adjoint wavefield to obtain the Frechet kernels according to Eq. (5.13) and (5.14). The third simulation can be exempted if one chooses to save the synthetic wavefield at each space location and each time point during the first simulation, however due to overwhelming storage requirements and the corresponding I/O time, *Tromp et al.* (2005) opted not to do so.

Once the Frechet kernels are formed, the conjugate gradient (CG) method can be employed to estimate a model update in the steepest descending direction. The Hessian is not formed because it would be numerically too expensive. Since CG only takes into account the gradient (first-derivative) of the misfit function, it converges much more slowly than the Gauss-Newton (GN) scheme, which utilizes the (approximate) Hessian (second-derivative of the misfit function). In this work, we propose a compromise between the two. We still use the normal equation (5.1), except the gradient (the right-hand side right-hand side of (5.1)) is computed with the adjoint method, while the approximate Hessian A^TA (the left-hand side of (5.1)) are still computed approximately with NACT to avoid the expensive numerical cost. It is one step forward from the hybrid tomography framework described in *Yuan et al.* (2013).

5.3 Current progress

In this section, we show results of numerical tests of forward and adjoint simulations using realistic event and stations from the NA tomography dataset used in *Yuan et al.* (2013).

5.3.1 The dataset

In order for a direct comparison with the previous generation hybrid tomography framework described in *Yuan et al.* (2013), we use the same dataset as that study. The dataset consists of three parts: (1) Waveforms from a collection of ~360 global earthquakes observed on global seismic network stations, filtered at a shortest period of 60 sec (used in *French et al.*, 2013); (2) ~600 global events observed at NA stations, filtered at 60 sec (used in *Yuan et al.*, 2011); (3) 136 NA regional events, filtered at 40 sec (added in *Yuan et al.*, 2013). The waveforms are broken up into packets of fundamental surface waves and overtones. The wave packets are weighted by their amplitude, noise level and path redundancy following the scheme described in *Li* and *Romanowicz* (1996).

Figure 5.1 shows an example event used for the tests described in the upcoming sections. The event occurred in Oklahoma on Nov 6th, 2011 with a magnitude of M_w 5.7 and a depth of 5 km. The location of the event is near the center of the study region, therefore the ray paths of different azimuths provide a comprehensive sampling of various parts of the NA continent, making this event ideal for test purposes.

5.3.2 Forward simulation using *RegSEM*

For the forwarding simulation of the seismic wavefield, we use the highly accurate numerical code, *RegSEM* (*Cupillard et al.*, 2012). *RegSEM* is a regional Spectral Element code. It allows a model "box" of horizontal size as big as 90°×90° and laterally as deep as to the core-mantle boundary. It uses spherical coordinates. Ellipticity of the Earth, attenuation and arbitrary anisotropy can be included. Perfect Matched Layer (PML) absorbing boundary conditions are used to avoid artificial reflections at the boundaries of the model box.

Figure 5.2 and 5.3 shows results of forward simulation with *RegSEM* for the test event. The velocity model used is the starting model in *Yuan et al.*, (2013). In Figure 5.2, a snapshot of the wavefield at t = 1000 sec approximately after the event origin is shown. In Figure 5.3, synthetic seismograms at a few stations are shown in comparison against observations. The RegSEM synthetics show reasonable agreement with the observed waveforms both in phase and amplitude. There are some phase mismatches, which is

expected because this is only a starting model. It is noticeable that the body wave fits are good.

5.3.3 Body wave picking

One weakness in the NA model presented in *Yuan et al.* (2013) is that the amplitude of heterogeneity decreases at greater depths (>200 km), especially for ξ, the radial anisotropy parameter (defined as V_{SH}^2/V_{SV}^2, where V_{SH} and V_{SV} are the horizontally and vertically polarized shear wave velocities, respectively). Several reasons may be responsible for it. The most likely one is the lack of body waves which are more sensitive to the deeper structure than the surface waves, despite the fact that overtone surface waves were used in *Yuan et al.* (2013); other possible reasons include the incompatibility between the synthetic waveforms computed from *RegSEM* (for the regional events) and those from NACT (for the global events). As a remedy, in this study we add packets of body waves from the dataset. Figure 5.4 shows examples of body wave packets picked for the test event at station BBGH. For stations at greater epicentral distances such as this one, both *P* and *S* (and sometimes *SS* and/or *ScS*) wave packets are picked. In *Yuan et al.* (2013), these body wave packets are picked altogether as one overtone wave packet. By breaking the overtone packet into several individual body wave packets, one can now apply different weights to these packets to balance the amplitude differences, which will hopefully lead to improvement in the heterogeneity amplitude recovery power at depth.

5.3.4 Adjoint simulation using *RegSEM*

The adjoint source is formed according to Eq. (5.15). Only the stations with picked wave packets are included in forming the adjoint source. The weight information contained in the wave packets is carried over. Figure 5.5 shows examples of the time-reversed waveform residuals at station BBGH. The residuals from all stations with successful wave packet picks are summed to form the adjoint source, which is then fed to the wave equation to solve for the adjoint wavefield.

In the adjoint simulation, one key point to pay attention to is the attenuation. Because the adjoint simulation is time-reversed, the amplitude of the wavefield may blow up if the attenuation is not properly treated. *Masson et al.* (2014) implemented the idea of "checkpoints" in *RegSEM*, where the adjoint wavefield is inspected at regular time intervals to make sure the amplitude does not diverge. A snapshot of the adjoint wavefield from the test event is shown in Figure 5.6.

5.3.5 Next steps

Due to time constraints, the authors are unable to finish all the steps of this project. Remaining steps include: (2) Form the gradient from the adjoint simulation, and project

from the GLL (Gauss-Lobatto-Legendre) node basis used in *RegSEM* to the spline basis on which the Hessian A^TA is computed. The inversion will be done on the latter basis. (3) The inversion.

In addition, *Masson et al.* (2014) have implemented a modification to the *RegSEM* code, which allows it to simulate "out-of-box" teleseismic events by using the refined regional model inside the box and a coarser global 3D model outside the box. Including "out-of-box" events will help to further improve the path coverage for the target region. This new development will allow us to place the North America in the background 3D global model (e.g. *French et al.*, 2013; *French*, 2014) for inversion in a consistent manner, and hopefully lead to higher compatibility between the regional and the global models.

5.4 Conclusions

We set up the theoretical framework for a hybrid adjoint tomography for the North American continent. In this framework, we solve the Gauss-Newton normal equation for model update, and the gradient of the misfit function is computed based on the adjoint method with the numerical code *RegSEM*, whereas the sensitivity kernel A and the approximate Hessian A^TA are still computed approximately with NACT. This is one step forward toward fully numerical continental-scale tomography from our previous NA tomography studies, while the computational efficiency (convergence) is the same as the Gauss-Newton method. We have also implemented the first few steps of the tomography with the existing NA dataset. Although not all steps are implemented yet, this work serves as a starting point for future work.

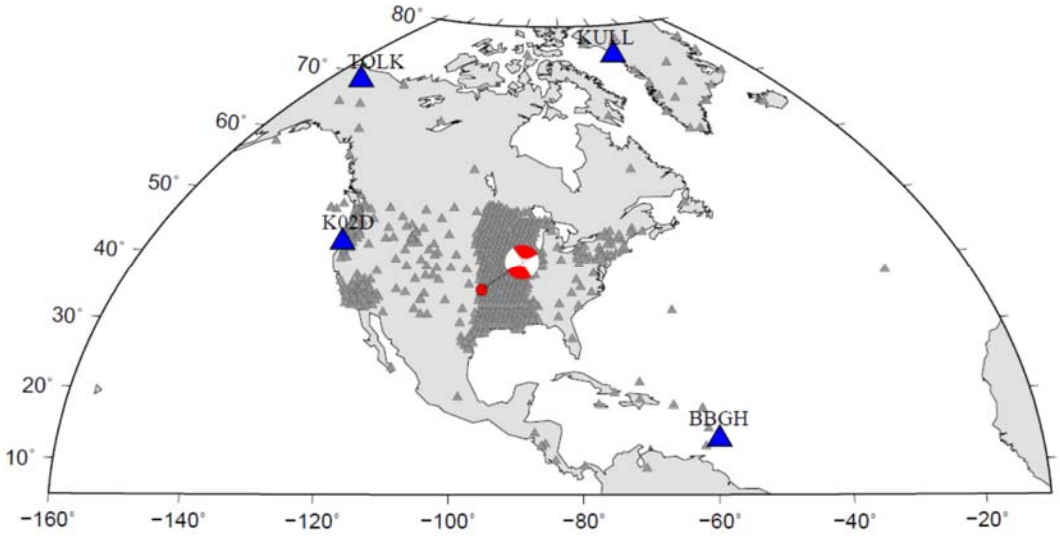

Figure 5.1. A map showing the seismic event (2011 Oklahoma M_w 5.7 earthquake) and the stations used for numerical tests. The beachball shows the global CMT focal mechanism for this earthquake, and the red dot shows its location. Highlighted and labeled are the stations for which seismograms are shown in Figure 5.3, 5.4 and 5.5.

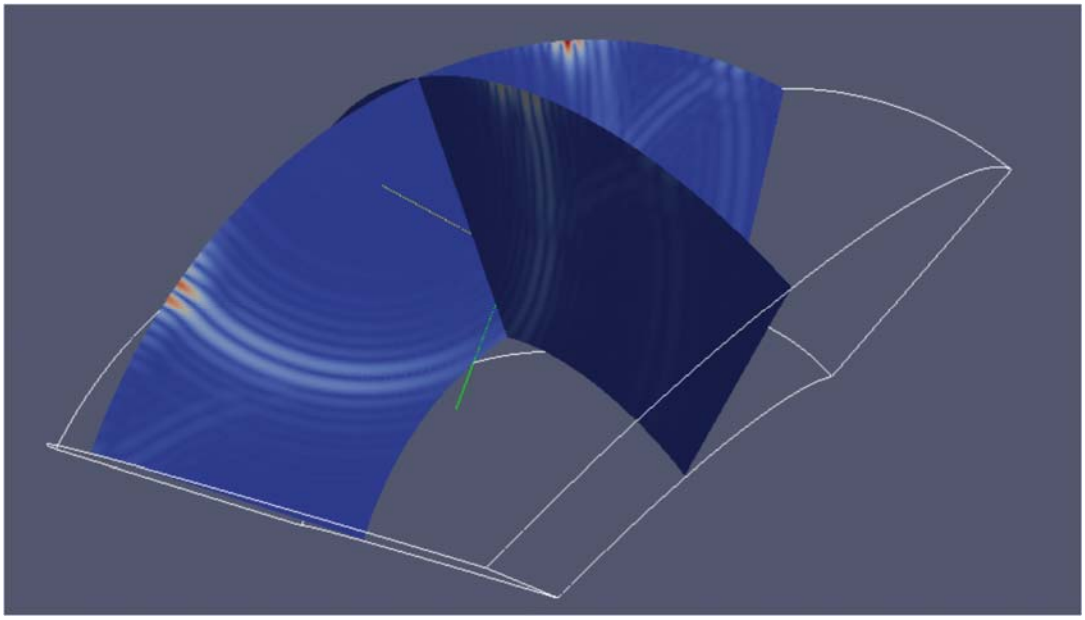

Figure 5.2. A snapshot of the forward wavefield for the test event shown in Figure 5.1 using the *RegSEM* simulation code (*Cupillard et al.*, 2012). The white frame shows the model box used in *RegSEM*; it has a horizontal size of 90°×90° and the depth ranges from 0 to 2800 km. The 3D velocity model is the starting model used in *Yuan et al.* (2013). The snapshot at approximately 1000 seconds after the event origin time is shown. The entire length of simulation is 3000 seconds.

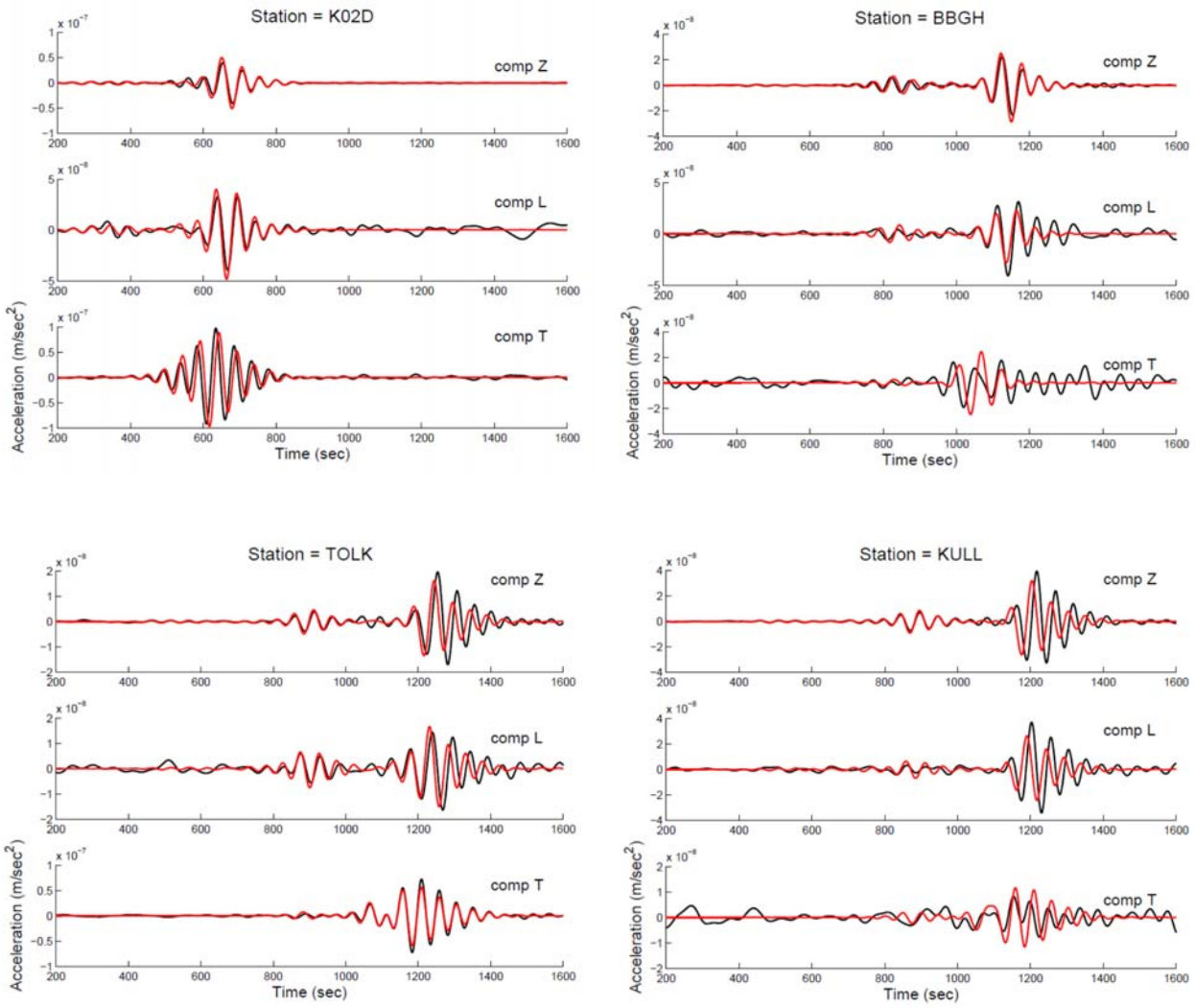

Figure 5.3. Synthetic seismograms (red) for the test event from *RegSEM* forward simulation, in comparison to observed seismograms (black), for the stations highlighted in Figure 5.1. All seismograms are filtered with a cosine taper at (40, 60, 250, 400) sec, with the four numbers denote the shortest cutoff period, the shortest corner period, the longest corner period and the longest cutoff period, respectively.

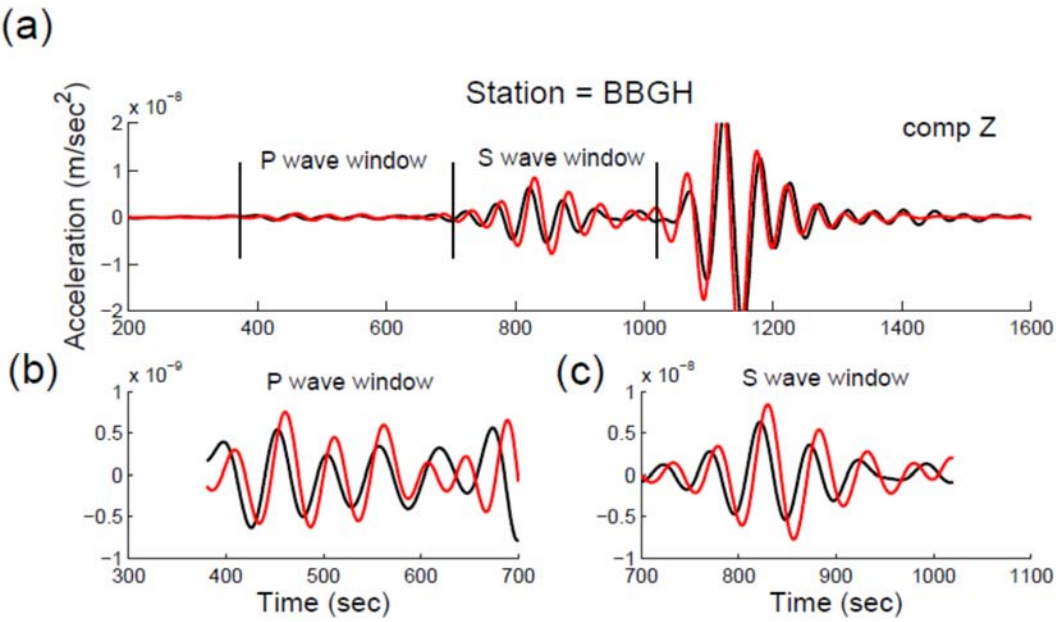

Figure 5.4. Examples of body wave packets picked from vertical component seismogram at station BBGH (epicentral distance Δ=42°). (a) The synthetic (red) and observed (black) seismograms. (b) The P wave packet picked. (c) The S wave packet picked. The waveforms in (b) are amplified by a factor of 10 to be comparable to (c).

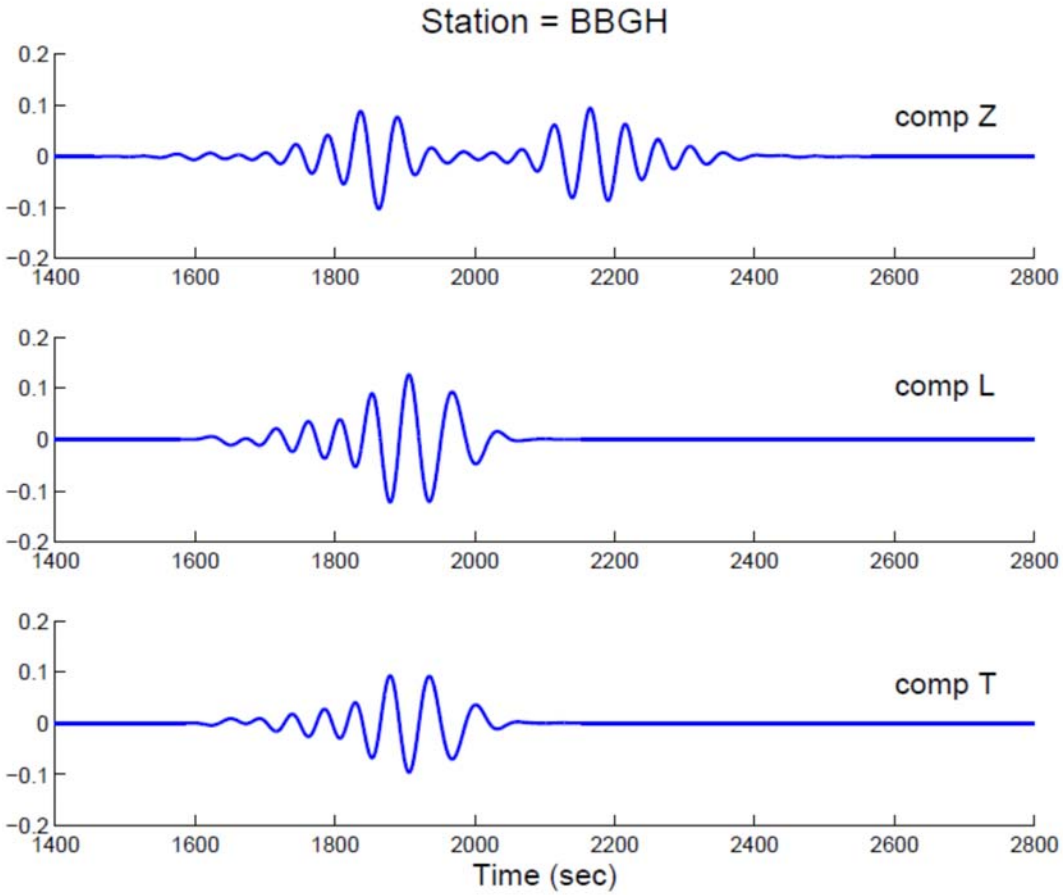

Figure 5.5. Time-reversed waveform residual (observation minus synthetic) at station BBGH. The residuals at all stations for which wave packets are successfully picked are then combined to form the adjoint source.

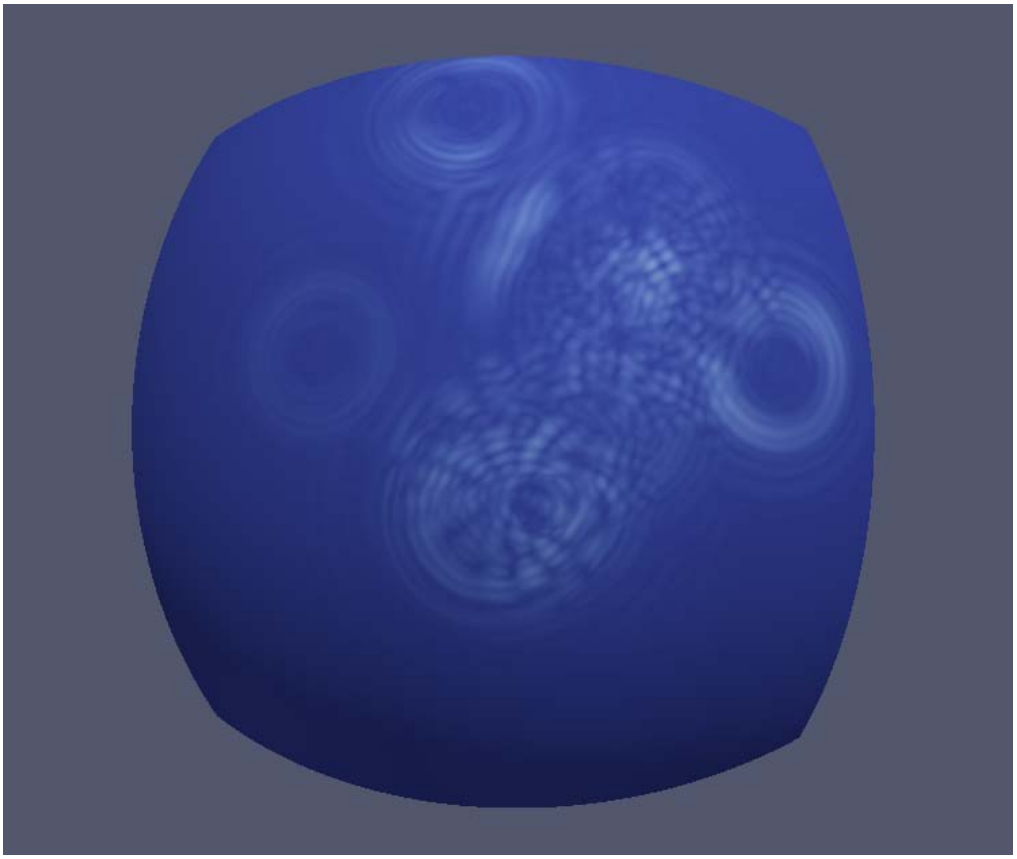

Figure 5.6. A snapshot (view from the top of the model box) of the adjoint wavefield for the test event from *RegSEM* simulation. For this test run, only a subset of receivers are used as adjoint sources. The concentric rings show the propagation of wavefronts, and the adjoint sources are located at the centers of each set of rings.

Chapter 6

Long Period Noise Removal for MOBB and Its Application to Regional Moment Tensor Inversion in Northern California

This chapter has been published in *Bulletin of Seismological Society of America* under *Taira, Zheng* and *Romanowicz* (2014) with the title 'On the Systematic Long Period Noise Reduction on Ocean Floor Broadband Seismic Sensors Collocated with Differential Pressure Gauges'.

6.1 Introduction

Vertical component data from broadband stations installed on the ocean floor at regional distances from the coast exhibit increased noise levels, compared to land stations, at long periods (typically 20-200 s), due to the effect of ocean infragravity (IG) waves induced by a dynamic ocean environment. This period range is essential for several applications: structural studies using surface waves as well as moment tensor inversion of regional earthquakes. In particular, rapid moment tensor determination of regional earthquakes is one of the crucial components in real-time earthquake hazard assessment in regions such as California (Sipkin, 1982; Dreger and Helmberger, 1991; Romanowicz *et al*., 1993; Dreger and Romanowicz, 1994; Pasyanos *et al*., 1996; Tajima *et al*., 2002; Ichinose *et al*., 2003; Clinton *et al*., 2006; Guilhem and Dreger, 2011). This is also the period range of choice for studies of regional structure using surface waves. Surface wave observations from offshore stations are necessary to constrain structural transitions in the crust and upper mantle at the edges of continents.

In practice, the reliability of the moment tensor determination strongly depends on the station azimuthal coverage (e.g., Ford *et al*., 2010). Improved estimates of the moment tensor could be achieved by integrating broadband seismic data from ocean bottom seismographs (OBS) in near coastal regions and on the seaside of offshore active faults, for which OBS data fill the gap of station azimuthal coverage. Minimizing IG-wave induced signals on broadband OBS records is therefore essential. In particular, developing an automatic procedure for IG-wave induced signal removal is crucial to make use of OBS records for real-time moment tensor determination.

Long-term data collection at the Monterey Ocean Bottom Broadband (MOBB) observatory (Romanowicz *et al*., 2003, 2006) offers a unique opportunity to characterize IG-wave induced signals on OBS records and to develop an optimal near real-time procedure for their removal. Additionally, station MOBB is the only offshore broadband seismic station in central California (Figure 6.1), except for the island-based Farallon Islands station (station FARB) of the Berkeley Digital Seismic Network (BDSN) (Romanowicz *et al*., 1993). It thus provides complementary azimuthal coverage of the San Andreas Fault system to the land-based network. Moreover and most importantly, broadband OBS data from station MOBB have now been available in real time since February 2009 (Romanowicz *et al*., 2009).

6.2 Data and Methodology

6.2.1 The MOBB Observatory

Station MOBB was installed in April 2002, at a water depth of 1000 m about 40 km offshore in the Monterey Bay, California (Figure 6.6.1) through a collaborative effort between the Monterey Bay Aquarium Research Institute (MBARI) and the Berkeley Seismological Laboratory (BSL). Station MOBB is equipped with three geophysical sensors: (1) a three-component broadband Güralp CMG-1T seismometer, with corners at periods of 0.02 s and 360 s, (2) a differential pressure gauge (DPG) (Cox *et al*., 1984), and (3) an ocean-bottom current meter. Broadband seismic data are sampled at 20 Hz while DPG and ocean-bottom current data are sampled at 1 Hz (Romanowicz *et al*., 2003, 2006). The seismometer package is installed inside a PVC cylinder that was buried in the seafloor, and covered with glass beads (Romanowicz *et al*., 2003). This was performed with the help of the MBARI ROV "Ventana".

After 7 years of autonomous operation, in February 2009, the MOBB instrument package was successfully connected to the Monterey Accelerated Research System (MARS) fibre-optic cable, and the data have been available in real time at the Northern California Earthquake Data Center (Romanowicz *et al*., 2009; see the Data and Resources section). Since then, the data completeness has significantly improved and the internal clock drift of the MOBB seismic sensor has been continuously monitored (D. Neuhauser, personal communication, 2012).

6.2.2 Observation of IG Waves

IG waves are primarily generated by non-linear interactions between short-period ocean waves with periods of 5 s to 20 s along the nearshore region (Munk, 1949; Tucker, 1950; Sutton *et al*., 1965; Snodgrass *et al*., 1966; Herbers *et al*., 1995). Seafloor deformation under the pressure forcing by IG waves results in long-period seismic signals (20-500 s) on OBS records (e.g., Webb *et al*., 1991; Webb, 1998; Dolenc *et al*., 2005; Laske *et al*., 2009; Bromirski *et al*., 2010; Yang *et al*., 2012). At station MOBB, seismic signals induced by IG waves are generally more dominant on the vertical component than on horizontal components (Dolenc *et al*., 2005).

We compared the background noise level of the MOBB vertical component data, with those from other stations installed on land (Figure 6.6.2). Due to the IG-wave induced seismic signals, the background noise level of station MOBB shows a marked increase in the period range 20-200 s, compared with those from land stations. In the period range 1-10 s, increased noise levels observed at all stations correspond to the double-frequency microseismic peak. A smaller peak around at a period of 12 s corresponds to single frequency microseisms.

The 20-200 s period band for the IG-wave induced signals generally overlaps with that used for a variety of seismic analyses including surface wave imaging studies (e.g., Ritzwoller *et al*., 2002; Pasyanos, 2005; Obrebski *et al*., 2011) and seismic moment

tensor analysis for regional earthquakes (e.g., Dreger and Romanowicz, 1994; Kao *et al*., 1998; Kubo *et al*., 2002; Stich *et al*., 2003; Bernardi *et al*., 2004; Brandt *et al*., 2011).

During stormy weather, the IG-wave induced signal is observed in a broader period range (~20-500 s) and its amplitude is higher (Figure 6.6.2). As only the energy of IG waves with wavelengths longer than the water depth is coupled with ocean floor, the IG-wave induced signals are not observed at periods shorter than 20 s at station MOBB. This is the hydrodynamic effect, resulting in a "low noise notch" (between the microseismic peak and the IG wave peak), the width of which varies with the depth of water (Araki *et al*., 2004; Dolenc *et al*., 2008; Laske *et al*., 2009; Webb and Crawford, 2010; Bécel *et al*., 2011; Yang *et al*., 2012). As shown in Dolenc *et al*. (2005), because of the depth of water of 1000 m at station MOBB, this low noise notch is limited to the period range 10-20 s, where the background noise level of MOBB data is comparable to that of land-stations (Figure 6.6.2).

6.2.3 Removal of IG-Wave Induced Noise on Vertical Component OBS Data

Following previous studies (e.g., Webb and Crawford, 1999; Crawford and Webb, 2000; Crawford et al., 2006; Dolenc *et al*., 2007), the noise removal method we have employed makes use of the frequency-dependent transfer function between vertical seismic and pressure recordings to predict the deformation signal induced by IG waves on the vertical component. Ambient noise on DPG records is primarily induced by IG waves (Webb and Crawford, 1999). The transfer function allows the removal of the predicted deformation signal induced by IG waves from the vertical seismic records.

In the frequency domain, the transfer function, $T(\omega)$, at frequency ω, can be expressed as

$$T(\omega) = \gamma(\omega)\sqrt{G_{ss}(\omega)/G_{pp}(\omega)}, \tag{6.1}$$

where $G_{ss}(\omega)$ and $G_{pp}(\omega)$ are the average ensembles of one-sided auto-spectral density functions for vertical component and pressure records, respectively, and $\gamma(\omega)$ is the coherence between these records (Webb and Crawford, 1999). We used the coherence function defined by Bendat and Piersol (1986) as

$$\gamma(\omega) = \frac{G_{sp}(\omega)}{\left[G_{ss}(\omega)\cdot G_{pp}(\omega)\right]^{1/2}}, \tag{6.2}$$

where $G_{sp}(\omega)$ is the average ensemble of one-sided cross-spectral density function between vertical component and pressure records. Following Crawford and Webb (2000),

we estimate $G_{ss}(\omega)$, $G_{pp}(\omega)$, and $G_{sp}(\omega)$ from the Fourier transforms of the observed vertical component data $S(\omega)$ and pressure recording $P(\omega)$:

$$G_{ss}(\omega) = \left(\frac{2}{NL}\right)\sum_{i=1}^{N}|S_i(\omega)|^2$$

$$G_{pp}(\omega) = \left(\frac{2}{NL}\right)\sum_{i=1}^{N}|P_i(\omega)|^2$$

$$G_{sp}(\omega) = \left(\frac{2}{NL}\right)\sum_{i=1}^{N}S_i^*(\omega)\cdot P_i(\omega) \tag{6.3}$$

where $S_i(\omega)$ and $P_i(\omega)$ are the Fourier transforms of the vertical component and pressure records, respectively for the data window i, and N and L are the number of data windows and the length of data window, respectively. The asterisk represents the complex conjugate.

The coherent part of the pressure record corresponding to IG-wave induced signals is subtracted from the vertical component seismogram, and the resulting spectrum of the vertical component seismogram after correction for IG-wave induced signal $S'(\omega)$ can be expressed as:

$$S'(\omega) = S(\omega) - T^*(\omega)\cdot P(\omega), \tag{6.4}$$

The noise removal of IG-wave induced signals with the transfer function is based on the high temporal correlation ($\gamma(\omega)$ in equation (6.2)) between the vertical component and DPG records in the IG wave band. This temporal correlation between MOBB OBS and DPG data is examined in the Temporal Behavior of Transfer Function section.

6.3 Results and Discussion

6.3.1 Temporal Behavior of the Transfer Function

We have systematically analyzed all available MOBB broadband seismic and DPG records collected between February 2009 and June 2012 and computed the transfer function between them as described above (equation (6.1)). Prior to February 2009, i.e. when MOBB was an autonomous station, visited every 3-4 months, data analysis is made more difficult due in particular to the presence of time offsets between the broadband seismic and DPG channels caused by internal clock drifts of the seismometer. Note that the cable which links the MOBB instrumentation to the MARS science node was trawled

in February 2010, and about a year of data is missing, until it was possible to replace the cable in June 2011.

As previously noted (Dolenc *et al*., 2007), in the absence of earthquakes, vertical displacement and pressure records are nearly perfectly coherent in the IG wave band (Figure 6.3a). The continuous MOBB OBS and DPG records are split into non-overlapping 3-hour-long segments, to examine the temporal behavior of the coherence and the transfer function. In each single 3-hour-long data, we employed a moving-window cross-correlation analysis by using a 2048-s time window with 50% overlap to compute the ensemble averaged cross-correlation spectra. The use of this short-time window with overlap will minimize effects of long-duration wave trains from teleseismic earthquakes in the coherence and transfer function estimates.

We examined the variability of the coherence squared, by computing the median and the lower 5th percentile of the coherence-squared distribution obtained from the 3-hour-long data set (Figure 6.3b). We used the lower 5th percentile as the lower bound of the coherence squared. We obtained 4487 3-hour-long records used to estimate the distribution of the coherence squared. For example, at a period of 75 s, the median and the lowest 5% of the coherence squared are 0.9918 and 0.9809, respectively.

Our measurement shows the median values of the coherence squared in the period band 30-200 s are higher than 0.990 (Figure 6.3c) which corresponds to the theoretical limit of noise reduction of about 20 dB inferred from $10*\log_{10}(1-\gamma^2(\omega))$ introduced in Webb and Crawford (1999). The high median coherence squared (> 0.990) in the period band 30-200 s indicates that the seismic signals observed on the vertical component, in the absence of earthquakes, are primarily due to seafloor deformation under pressure loading induced by IG waves. Therefore, deformation signals computed with the transfer function ($T^*(\omega)$ x $P(\omega)$) in equation (6.4)) represent the IG-wave induced signals on the MOBB vertical component data well. The lower 5th percentile of the coherence-squared distribution, however, shows rapid decays of the coherence squared below 40 s and above 100 s (Figure 6.3c). The amount of noise reduced by the transfer function will thus very for individual 3-hour-long segments analyzed.

We observe several excursions in the transfer function associated with the internal clock drifts and timing corrections of the MOBB OBS (Figure 6.4). We manually excluded this type of excursions from our data sets based on the station MOBB log file (D. Neuhauser, personal communication, 2012). This procedure rejects 16% of the 3-hour-long data and the total number of the 3-hour-long segments used in this study is 4487.

The temporal evolution of the transfer function shows an abrupt change in transfer function from the 3-hour-long segment between March 2010 and July 2011, i.e. at both ends of the interruption due to the cable failure (Figure 6.5). This change corresponds to

the replacement of the DPG by another sensor of the same type, with nominally the same instrument response function, while the seismometer was not modified (P. McGill, personal communication, 2012). The replacement of the DPG appears to introduce a constant offset in the transfer function (Figures 5b and 5d). Our observation illustrates that different DPGs actually have significantly different instrument responses, which may be important for certain types of studies relying on the DPG calibrations (e.g., Baba *et al*., 2004; Saito *et al*., 2010; Ito *et al*., 2011; Maeda *et al*., 2011; Saito *et al*., 2011).

As shown in Figure 6.5a, there appears to be a seasonal variation in the amplitude response of the transfer function at a period of 25 s during the time interval April 2009 to February 2010. The amplitude response at this period systematically increases by a factor of about 2 from northern hemisphere summer (April through September 2009) to winter (October through December 2009 and January through February 2010). One possible explanation for this systematic change is that it is due to a temperature effect (Barzilai *et al*., 1998). A systematic temporal variation is not observed during the time interval July 2011 to June 2012 although the variability of the amplitude of the transfer function is comparable to that observed during the time interval April 2009 to February 2010. To characterize the temporal variations of the transfer function at a period of 25 s and the possible causes of the fluctuations will require analyzing longer term data sets and will be addressed in a further study.

We obtained the 1-day stacks of transfer function and examined their variability (Figure 6.6). We determined that a 1-day time window is the optimal window length to compute the transfer function in order to obtain the maximum reduction in the IG-wave induced signals on the vertical component data (see the Obtaining Improved Vertical Waveform Data section). Similarly to the estimate of the coherence squared, we estimated the median amplitude and phase responses for the 1-day stack of transfer function, and the lower and higher 5th percentiles, from the distributions of the amplitude and phase responses, to address the variability of the transfer function (Figure 6.6). Due to the abrupt change in the transfer function related to the replacement of DPG that occurred in July 2011, we used the two time intervals, before and after the DPG replacement to estimate the variability of the 1-day stack of transfer function.

The two reference transfer functions are obtained by applying a median stacking of transfer functions (the solid lines in Figure 6.6). These two reference transfer functions computed from the 2009-2010 and the 2011-2012 data hereafter are referred to as tf2009 and tf2011, respectively. As the lower and upper bounds of the 1-day stack of transfer function, we computed the lower and higher 5th percentiles from the distribution of the 1-day stacks of transfer function (the dashed lines in Figure 6.6). In each case, we estimated the percentage difference between the 1-day stacks of the transfer function and the reference transfer function $[(A_d(\omega)-A_r(\omega))/A_r(\omega)]$ x 100 (%) and $[(\phi_d(\omega)-\phi_r(\omega))/\phi_r(\omega)]$ x

100 (%), where $A(\omega)$ and $\phi(\omega)$ are the amplitude and phase responses, respectively, and the subscript d and r indicate the 1-day stack of transfer function and the reference transfer function.

Our analysis indicates that the amplitude and phase responses in the period band 50-100 s vary within the ranges of -5.6%-2.8% and -3.1%-3.4%, respectively. In the wider period range 35-200 s, the variabilities of the amplitude and phase responses are -10.68%-5.64% and -5.01%-6.11%, respectively.

6.3.2 Obtaining Improved Vertical Component Waveform Data

We obtained the MOBB vertical component data with reduced IG-wave induced noise, by applying the two reference transfer functions, tf2009 and tf2011 (Figure 6.7a). We used tf2009 and tf2011 for data collected in the time intervals 2009-2010 and 2011-2012, respectively. To estimate the variability of the noise reduction obtained with the reference transfer functions, we evaluated the median and lower 5th percentile from the distribution of noise reductions obtained from individual 3-hour-long data as a function of period (Figure 6.7b).

By using the reference transfer functions, the resulting median noise reduction in the period range 50-100 s is about 20 dB, which is comparable to the theoretical maximum reduction in the noise level inferred from the coherence squared (Figure 6.3c). In this period range, the lower 5th percentile of the distribution of noise reduction ranges from 13 dB to 15dB. This suggests that using a one-year stack of transfer function reduces the noise level on the MOBB vertical component data by at least 13-15 dB for any time window in the period band 50-100 s. At shorter periods, the amount of noise reduction is lower. We are however able to obtain a 5-15 dB noise reduction at periods greater than 30 s, which is important for our moment tensor analysis.

We additionally examined the amount of noise reduction by applying a set of transfer functions with different time windows, in order to identify the optimal length of time window to minimize the IG-wave induced noise on the vertical component data. In addition to the reference transfer functions, tf2009 and tf2011, we computed four different transfer functions with time windows of (1) 3 hours, (2) 1 day, (3) 10 days, and (4) 50 days. Those four transfer functions were obtained from the data collected prior to the 3-hour-long segment in which we applied the transfer function. For example, in the case of the 10-day transfer function, we computed the median transfer function by stacking transfer functions obtained from data segments collected in the last 1-10 days before the 3-hour-long data analyzed.

As with the estimate in the median noise reduction for the reference transfer function, we systematically analysed our entire data set by applying four different transfer functions

and obtained the median noise reduction for individual four different transfer functions. We then calculated the difference in noise reduction with respect to that obtained with the reference transfer function (Figure 6.7c). Our results show that the 1-day stack of transfer function obtained immediately prior to the 3-hour-long data minimizes noise induced by IG-waves. The improvement of noise reduction is however not more than 0.7 dB in the period range 50-100 s.

As the dominant period of IG-wave induced signals observed at station MOBB falls in the 50-100 s period band (Figure 6.2), our result shows that the reference transfer function derived from observations over a duration of several months to a year can allow us to effectively correct for the effect of IG waves on the MOBB vertical component records without continuously calibrating the transfer function, which in turn leads to an automatic implementation of the procedure. At shorter periods (30-50 s), the reference transfer function reduces the noise level by 5-15 dB. This noise reduction however improves signal-to-noise ratios for seismic signals from local earthquakes. It is thus possible to establish rapid data processing to provide OBS data recorded at station MOBB with enhanced signal-to-noise level and, in particular, to implement it for near real-time moment tensor analysis.

With these reference transfer functions, we minimized IG-wave induced signals in the vertical component and estimated the background noise level of the corrected MOBB vertical component data (MOBB.Z-C). We then compared it with that of the un-corrected MOBB Z-component data (MOBB.Z-U). The background noise level was identified as the median PSD from the distributions of PSDs obtained from 3-hour-long data (Figure 6.8). Although the amplitude of IG-wave induced signals varies with time, the resultant background noise level of MOBB.Z-C is about 20 dB quieter than that of MOBB.Z-U in the period band 50-100 s. The noise removal method used in this study provides an improved waveform dataset on the MOBB vertical component, with reduced noise in the IG wave band.

As the variability of the 1-day stack of transfer function exceeds +/- 2-3% in the period band 50-100 s (Figure 6.6), we need to check that the noise removal method with the reference transfer function does not remove seismic signals that are not related to the IG wave from the vertical component data, which would introduce distortion of the resulting waveforms used for the moment tensor analysis. To investigate this issue, we applied an optimal 1-day stack of transfer function for the waveforms from the local events listed in Table 6.1 and examined the waveform distortion by comparing the corrected MOBB vertical component waveforms obtained by the 1-day stack of transfer function with that from the reference transfer functions (Figure 6.9).

On the both corrected MOBB vertical data, the seismic phases radiated from the local events extracted by the noise removal method appear to be nearly identical, although there is residual long-period noises on the corrected waveform using the reference transfer function (the solid line shown in Figure 6.9). We conclude that the reference transfer function works well to obtain the improved vertical component data for our moment tensor analysis.

We also explored the effect of the two reference transfer functions on MOBB.Z-C records, by applying the reference transfer function obtained from the 2009-2010 data to a set of data including seismic signals from local earthquakes that occurred in 2011. Although the MOBB.Z-C data with the 2009-2010 reference transfer function shows a reduction of IG-wave induced signal (the thin line shown in Figure 6.10), this data still exhibits long-period noise that is not present in the MOBB.Z-C data corrected using the more appropriate 2011-2012 reference transfer function (the solid line in Figure 6.10). This analysis demonstrates that it is crucial to calibrate the transfer function when DPG sensors are swapped, even though the two DPG sensors have nominally the same instrument response.

6.3.3 Seismic Moment Tensor Analysis

We analyzed MOBB OBS data for twelve $M_w \geq 3.5$ local earthquakes (Table 6.1) that occurred in northern California during March 2009 through April 2012. We used two target areas to identify local earthquakes; (1) the region between latitude 35.50°N to 35.75°N and longitude -123.00°E to -120.50°E for $M_w \geq 4.0$ earthquakes (the solid rectangle in Figure 6.1) and (2) the region between latitude 36.30°N to 37.30°N and longitude -122.50°E to -121.50°E for $M_w \geq 3.5$ earthquakes (the dashed-line rectangle in Figure 6.1). The first target area includes the four M_w 4+ earthquakes that occurred along the Calaveras fault (EV1 and EV7), on the central San Andreas fault (EV10), and near the 2003 M_w 6.5 San Simeon rupture zone (EV3). The second smaller target area focuses on the northernmost creeping segment of the San Andreas fault in the San Juan Bautista region that includes eight M_w 3.5+ earthquakes.

We computed MOBB.Z-C data for the twelve local earthquakes and confirmed that our noise removal method recovers the seismic phases that were previously hidden in the IG-wave induced signals for the five of twelve local earthquakes (EV1, EV3, EV9, EV7, and EV10). For example, as illustrated in Figure 6.11, the seismic signal at periods greater than 30 s from EV1 is below the background noise level of the un-corrected MOBB vertical component data. At periods shorter than 50 s, the PSD of the seismic signal exceeds the noise level of the corrected MOBB vertical component data. The resultant PSD also appears to be above the low noise model of the corrected MOBB vertical

component data defined as the lower 5th percentile of the PSD distribution for the corrected MOBB vertical component data.

Regarding the remaining seven earthquakes, there are no seismic signals obtained on MOBB.Z-C data. We thus examined expected seismic signal levels by computing the data with synthetic seismograms obtained using the seismic moment tensor solutions determined by the Northern California Seismic System (NCSS). To compute Green's functions, we used the frequency-wavenumber code of Herrmann (2009; see the Data and Resources section), with a one-dimensional model called GIL7 (Table 6.2) that is currently used for the moment tensor analysis of northern California earthquakes (Dreger and Romanowicz, 1994). The amplitudes of the resultant expected seismic signals from these seven earthquakes are below both the background noise level and the low noise model for MOBB.Z-C in the period range 10-100 s (Figure 6.11).

We performed the moment tensor inversion for the five local earthquakes for which we recovered seismic signals on MOBB.Z-C data (Figures 12 and 13), assuming a double-couple source model (e.g., Stich *et al*., 2003; Minson and Dreger *et al*., 2008; Zahradník and Custódio, 2012). The moment tensor solutions were determined with a grid search approach, by maximum variance reduction (VR):

$$\mathrm{VR} = \left[1 - \frac{\int \{d_o(t) - d_s(t)\}^2 dt}{\int \{d_o(t)\}^2 dt} \right] \times 100, \tag{6.5}$$

where $d_o(t)$ and $d_s(t)$ are the observed and synthetic data, respectively. The grid intervals are 5 degrees in strike, dip, and rake, 1 km in depth, and 0.1 in M_w. We exclude MOBB horizontal data from the moment tensor inversion to focus on the waveform fits (or VR) for the MOBB vertical component data.

The noise removal method significantly improves VRs in the MOBB vertical component data for all five local earthquakes analyzed (Table 6.3). For example, the VR is increased from 9.2 % to 63.2 % for EV1 after the noise removal method is applied (Figure 6.12).

We evaluated total waveform VRs for three different data sets: (1) land-station data, (2) land-station with MOBB.Z-C data, and (3) land-station with MOBB.Z-U data (i.e. uncorrected data). The resultant VRs obtained using both land-stations and MOBB.Z-C data is comparable to those obtained using only land-station data (Figure 6.14 and Table 6.3). Our result demonstrates the effectiveness of the noise removal method using the reference transfer functions to include MOBB vertical component data in the moment tensor analysis. While the examples shown are for earthquakes that are already well constrained using the land-based network, we expect that inclusion of MOBB OBS data will be important for events that may occur offshore in the future.

As shown in Figures 12 and 13, MOBB horizontal component data exhibit long period noise likely induced by the effects of seafloor tilts which are strongly influenced by tides and ocean currents and are directional (Crawford and Webb, 2000; Dahm *et al*., 2006; Dolenc *et al*., 2008). Ocean-bottom current data from station MOBB will be used in a forthcoming study to explore the possibility of noise reductions on the horizontal components. Further assessment of noise on the horizontal components will likely require the availability of arrays of geophysical instruments, such as DPGs and ocean-bottom current meters.

6.4 Summary and Conclusions

We have analyzed several years of continuous vertical component MOBB broadband seismic data and DPG records and have shown that there is a strong correlation between the water pressure and the vertical component of seafloor ground velocity in the period range 30-200 s, By making use of this temporal correlation, a transfer function was determined and utilized to successfully deconvolve the IG-wave induced signals from the vertical component of MOBB broadband data.

The maximum noise reduction (up to 20 dB) in the IG wave band is obtained by using a 1-day stack of transfer function inferred from data segment collected prior to data in which the noise removal method is applied. A one-year stack of transfer function also reduces the noise level by 20 dB in the period range 50-100 s, and up to 15 dB in the period range 30-50 s. This period range is critical for regional moment tensor studies. Our result implies that we can use a median transfer function inferred from data collected for over a year to effectively correct for the effect of IG waves on the MOBB vertical component data, without having to calibrate the transfer function each time, providing a means to obtain improved MOBB vertical component data with reduced IG-wave induced noise, in quasi real-time.

The effectiveness of the noise removal method with the transfer function is demonstrated by recovering seismic phases that were previously masked by the IG-wave induced signals for five $M_w \geq 3.5$ local earthquakes. After applying the noise removal method, the waveform fit between the observed and synthetic for the MOBB vertical component data is significantly improved. The corrected MOBB data are then useful to determine the moment tensors of these five local earthquakes. We have implemented the IG-wave induced signal removal method into the NCSS to enhance the real-time earthquake monitoring capability in northern California. The noise removal method developed here can also be applied to other broadband deployments on the ocean floor, as long as DPGs are installed in the vicinity of the seismic sensors.

6.5 Data and Resources

Seismic data from land-based and MOBB OBS stations used in this study can be obtained from the Northern California Earthquake Data Center (http://quake.geo.berkeley.edu). The relocated earthquake locations were extracted from the double-difference earthquake catalog (http://www.ldeo.columbia.edu/~felixw/NCAeqDD and http://ddrt.ldeo.columbia.edu/DDRT/index.html). The surface traces of active fault were downloaded from the U.S. Geological survey Quaternary Fault and Fold Database of the United States (http://earthquake.usgs.gov/hazards/qfaults). Green functions used in this study were computed using the Computer Programs in Seismology package (http://www.eas.slu.edu/eqc/eqccps.html; Herrmann, 2009). Some plots are made a using the Generic Mapping Tools version 4.1 (http://www.soest.hawaii.edu/gmt; Wessel and Smith, 1998). Some data analyses were completed using the Seismic Analysis Code (http://www.iris.edu/software/sac; Goldstein and Snoke, 2003). All web sites were last accessed January 2013.

6.6 Acknowledgments

Morgan Guinois, undergraduate intern at BSL from May to July 2012 contributed to the data processing part of this study. We thank P. Lombard, D. Neuhauser, M. Hellweg, D. S. Dreger for the implementation of our noise removal codes into the Northern California Seismic System, and P. McGill for discussions. D. Dolenc kindly provides us with the codes to compute power spectral density and transfer function. Careful reviews by two anonymous reviewers greatly improved this manuscript. This study was supported by the National Science Foundation OCE-9911392 and OCE-0648302. This is BSL contribution number 13-14.

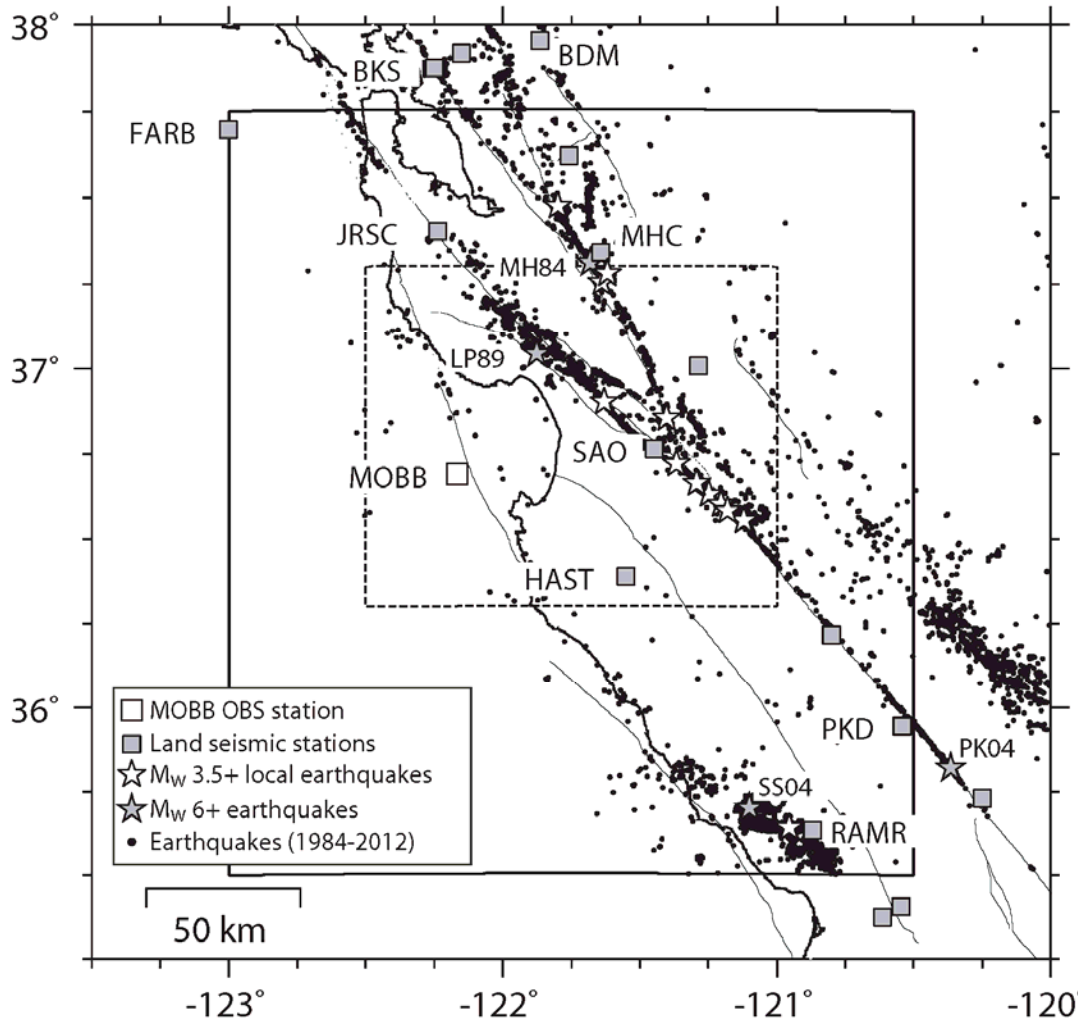

Figure 6.1. Map view of the ocean-bottom MOBB station with land-based broadband stations. The solid and dashed-line rectangles are the target areas (see texts for details) to identify the twelve $M_w \geq 3.5$ local earthquakes analyzed in this study. Also shown are earthquakes during 1984-2012 (Waldhauser and Schaff, 2008; see the Data and Resources section), the surface fault traces (thin lines; see the Data and Resources) and the locations of M_w 6+ historical earthquakes (MH84, the 1984 M_w 6.2 Morgan Hill earthquake; LP89, the 1989 M_w 6.9 Loma Prieta earthquake; SS04, the 2004 M_w 6.5 San Simeon earthquake; and PK04, the 2004 M_w 6.0 Parkfield earthquake).

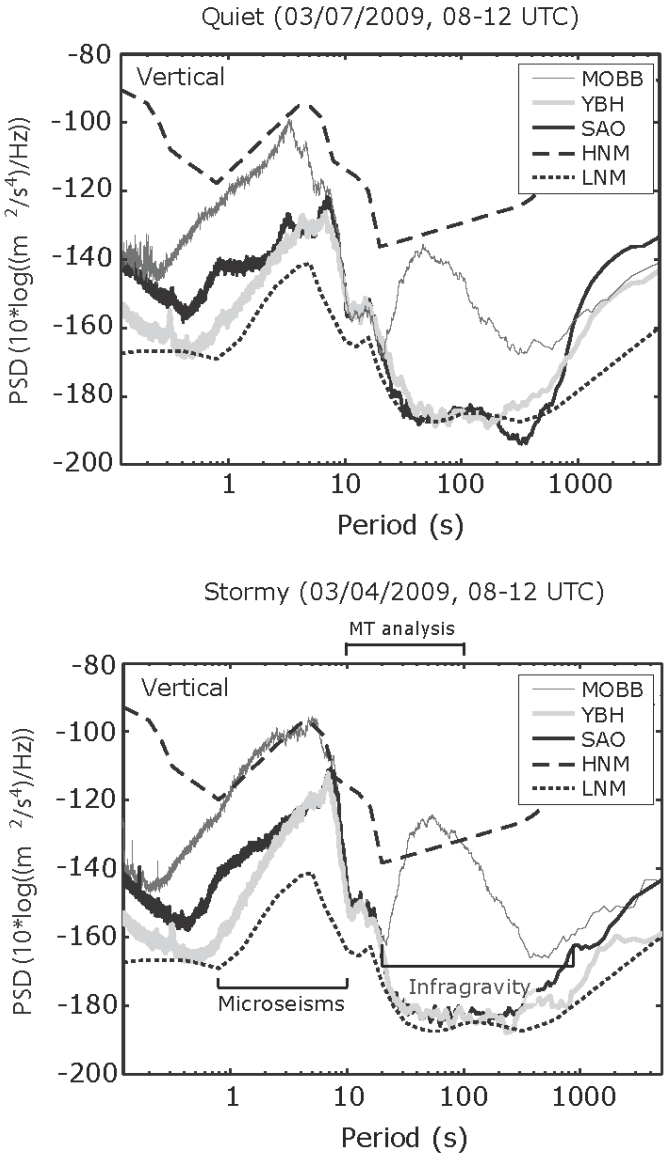

Figure 6.2. Power spectral densities (PSDs) of 4-hour-long noise data in the vertical component recorded at ocean-bottom station MOBB and two other BSDN land stations SAO and YBH (one of the quietest stations of the BDSN, located 560 km north of station MOBB) on two days in 2009 when no significant earthquake signals were recorded. The top and bottom panel show PSDs obtained on a "quiet day" and a "stormy day", respectively. Also shown are the U.S. Geological Survey high- (HNM) and low-noise (LNM) models (Peterson, 1993). Increased noise levels for periods 20 s to 200 s (induced by IG waves) are observed at station MOBB on both quiet and stormy days. A period range 10-100 s is used for our moment tensor (MT) analysis.

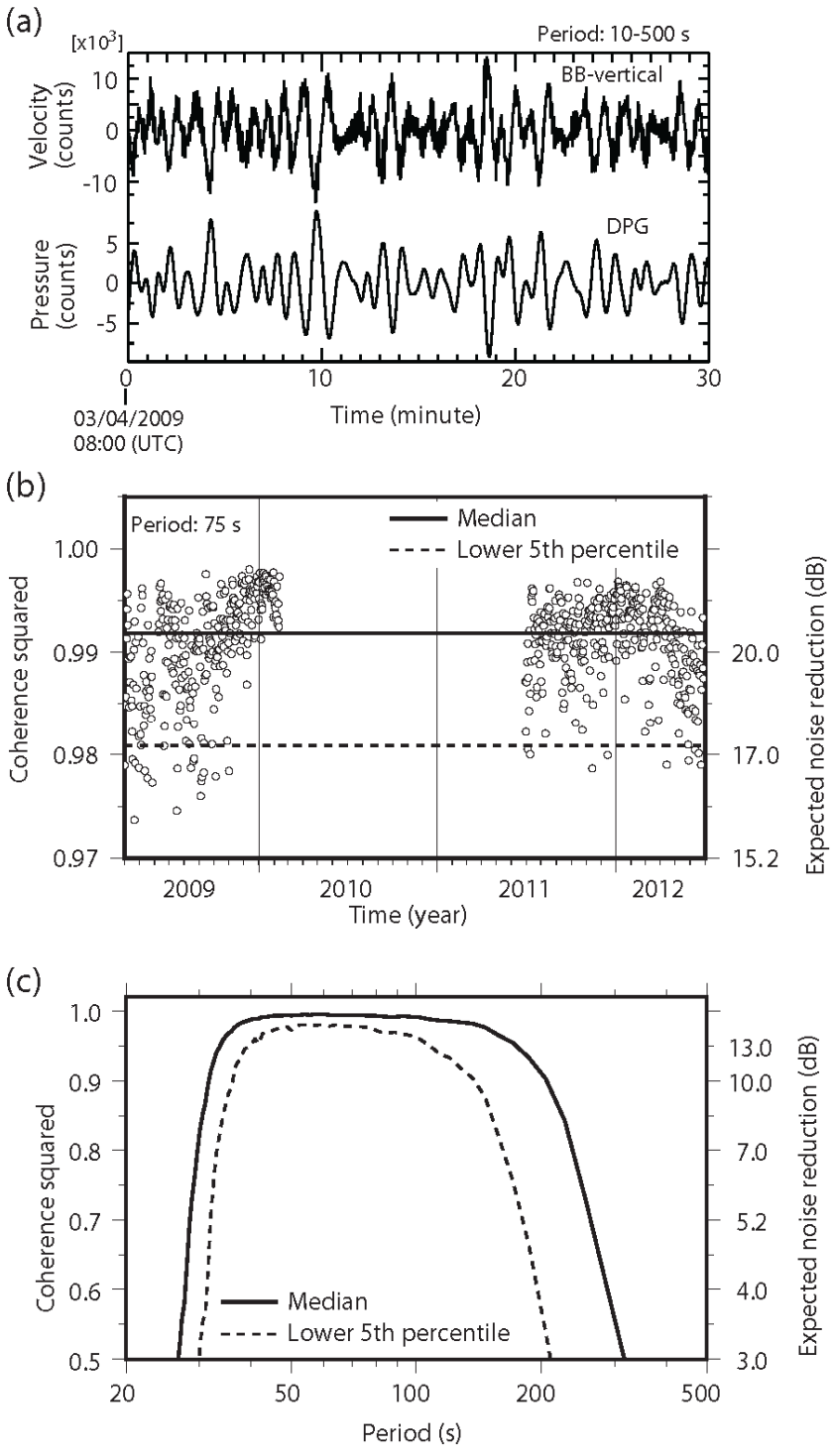

Figure 6.3. Correlation between the vertical component of seafloor ground velocity and the water pressure inferred from the DPG record in the IG wave band. (a) Observed 30-minute-long MOBB vertical component data (the top trace) and DPG record (the bottom

trace) with a 10-500 s bandpass filter. (b) Temporal behavior of the coherence squared between MOBB vertical component and DPG records at a period of 75 s. The solid line is the median coherence squared (0.9918). The dashed line is the lower 5th percentile (0.9809) obtained from the coherence-squared distribution estimated by analyzing 4487 3-hour-long records. Note that the MOBB data were not available during April 2010 through June 2011. (c) The median coherence squared (the solid line) and the lower 5th percentile of the coherence-squared distribution as a function of period. Also shown in Figures 6.3b and 6.3c is the theoretical limit of noise reduction (the right axis) introduced by Webb and Crawford (1999), inferred from the coherence squared (see texts for details).

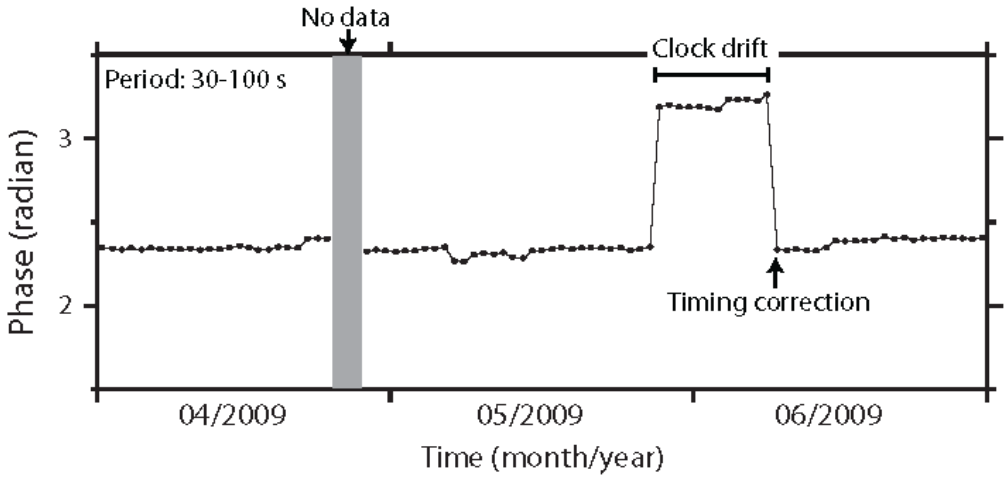

Figure 6.4. Temporal behavior of the phase response of the transfer function averaged over the period range 30-100 s for a 3-month period (April through June 2009). A change of the phase response occurred during 22 May through 9 June 2009 because of an internal clock drift of the MOBB OBS sensor. The transfer functions obtained during this period were excluded in the computation of the median transfer functions shown in Figures 6.5 and 6.6. The resultant transfer functions shown here are 1-day moving averages.

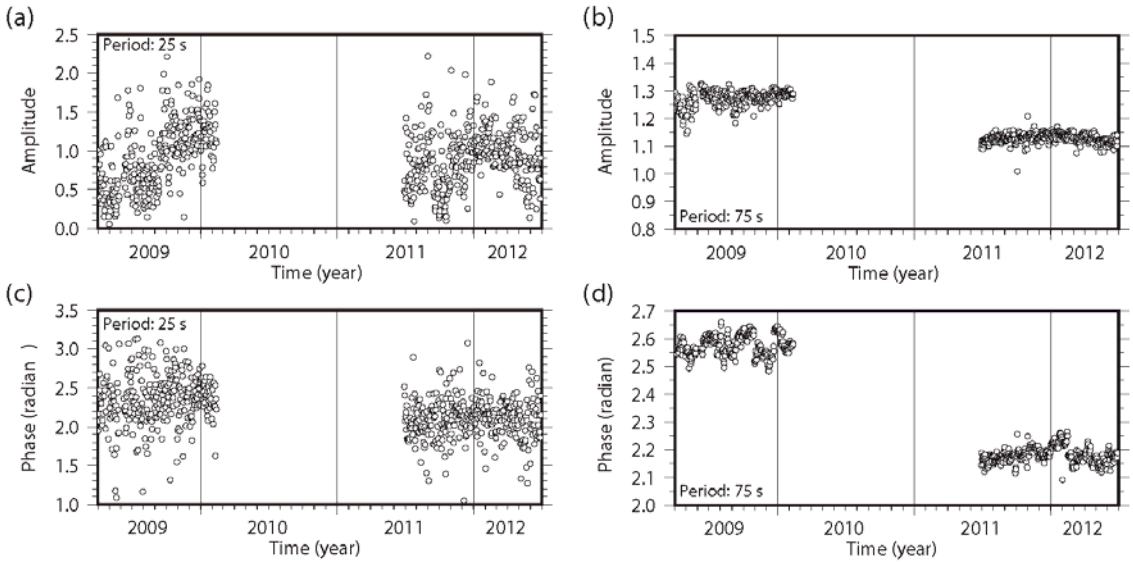

Figure 6.5. Temporal variations in transfer function at periods of 25 s and 75 s. (a,b) Amplitude and (c,d) phase responses of 1-day stacks of transfer function obtained from 3-hour-long data. The transfer functions obtained at a period of 25 s are shown in Figures 6.5a and 6.5c while those functions obtained at a period of 75 s are shown in Figures 6.5b and 6.5d. Note that the MOBB data were not available during April 2010 through June 2011.

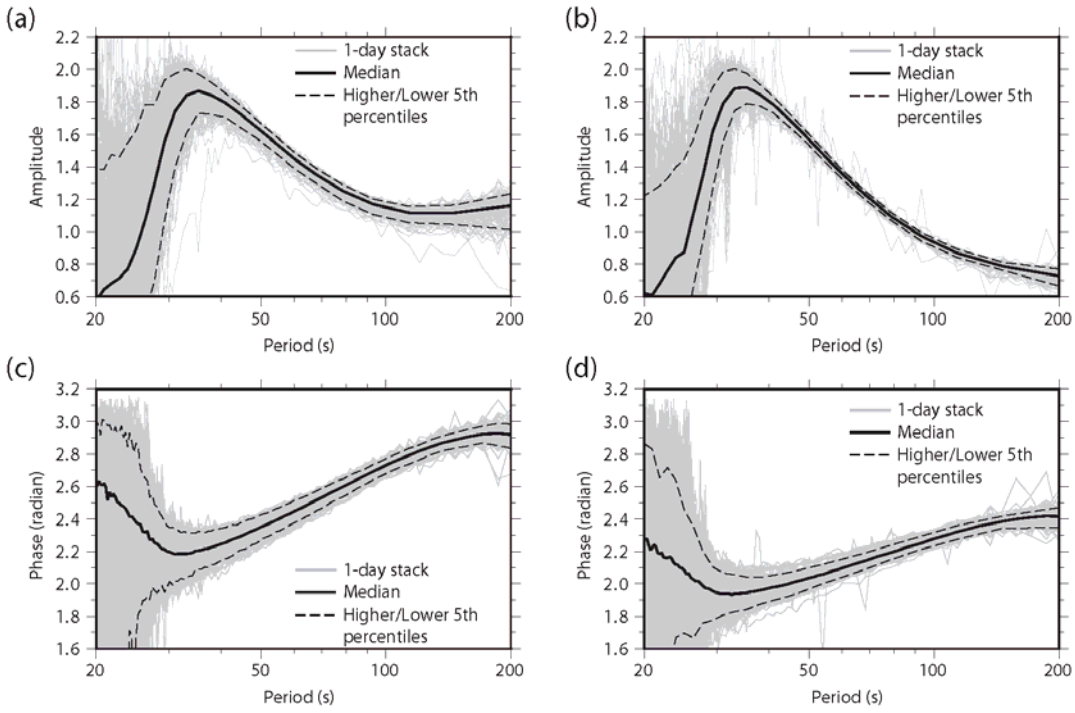

Figure 6.6. Variabilities of 1-day stacks of transfer functions in time intervals 2009-2010 and 2011-2012. (a,b) Amplitude and (c,d) phases responses of 1-day stacks of transfer function. The solid lines are the median values (the solid line). The transfer functions obtained in the time interval 2009-2010 are shown in Figures 6.6a and 6.6c while those functions obtained in the time interval 2011-2012 are shown in Figures 6.6b and 6.6d. Also shown are the lower and higher 5th percentiles (the dashed lines) of the distribution of the transfer functions.

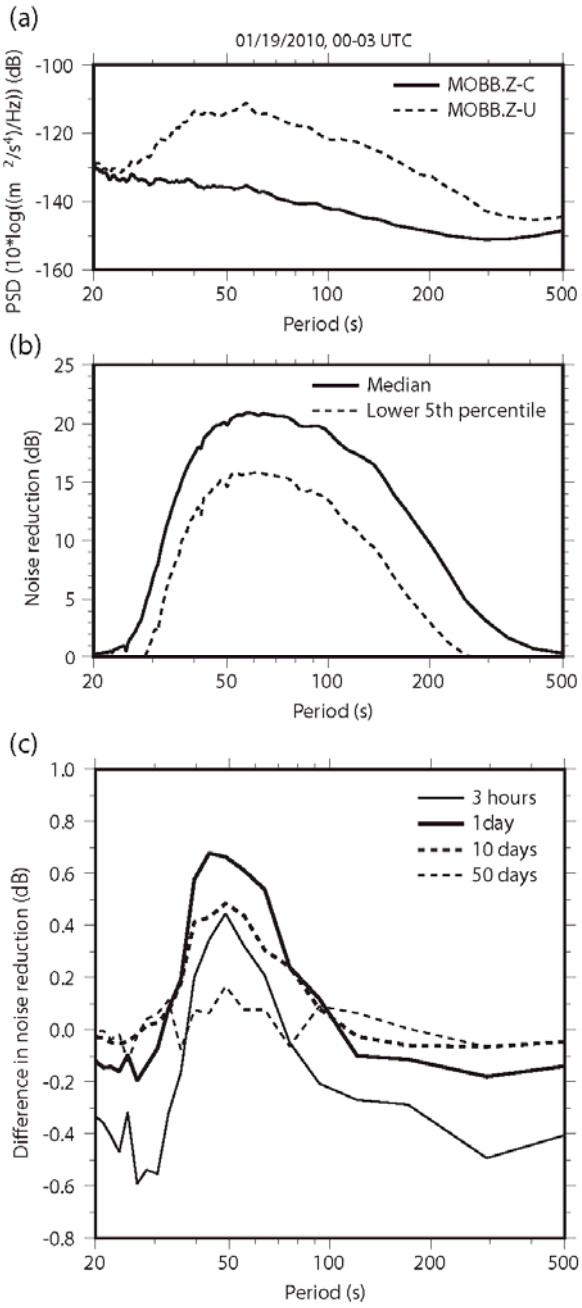

Figure 6.7. Noise removal of IG-wave induced signals. (a) Example of the noise reduction with the reference transfer function. The solid and dashed lines are PSDs for the corrected (MOBB.Z-C) and un-corrected (MOBB.Z-U) MOBB vertical component data, respectively. (b) The median noise reduction (the solid line) and the lower 5th percentile (the dashed line) of the noise reduction inferred from the distribution of the noise reduction distribution estimated by analyzing 4487 3-hour-long records. (c) Comparison of amounts of noise reductions by different transfer functions. The four different transfer functions with time windows of 3 hours (the thin line), 1 day (the solid

line), 10 days (the dashed line), and 50 days (the thin dashed line) were used to estimate the difference in median noise reduction with respect to that obtained with the reference transfer function (the solid line shown in Figure 6.7b).

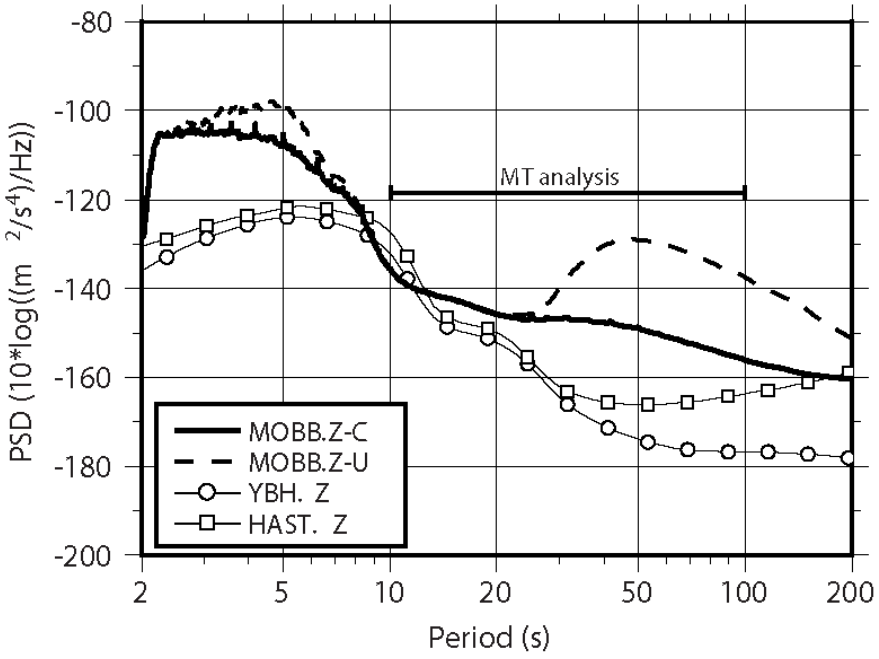

Figure 6.8. Reduction of noise level at IG wave periods (20-200 s) obtained by applying the noise removal method (equation (6.4)). Comparison of the noise levels of the corrected (MOBB.Z-C) and un-corrected (MOBB.Z-U) MOBB vertical component data. Also shown are the median PSDs for land stations YBH and HAST determined from all available data collected in 2011. Data in the period range 10-100 s were used for our moment tensor (MT) analysis.

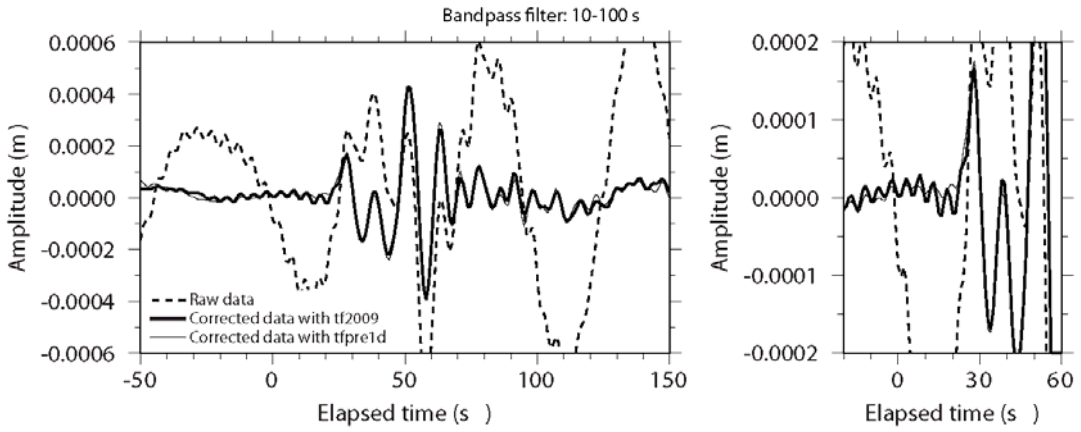

Figure 6.9. Seismic waveforms for the EV3 M_w 4.4 local earthquake. The solid and thin traces are MOBB vertical component data after removal of the coherent DPG record by using the reference transfer function (tf2009) and the 1-day stack of transfer function (tfpre1d), respectively. Also shown is the un-corrected MOBB vertical seismogram (the dashed line). A 10-100 s bandpass filter was applied to waveform data. Left panel shows 200-s-long records and right panel shows an enlarged view to illustrate residual long-period noises on the corrected waveform using the reference transfer function.

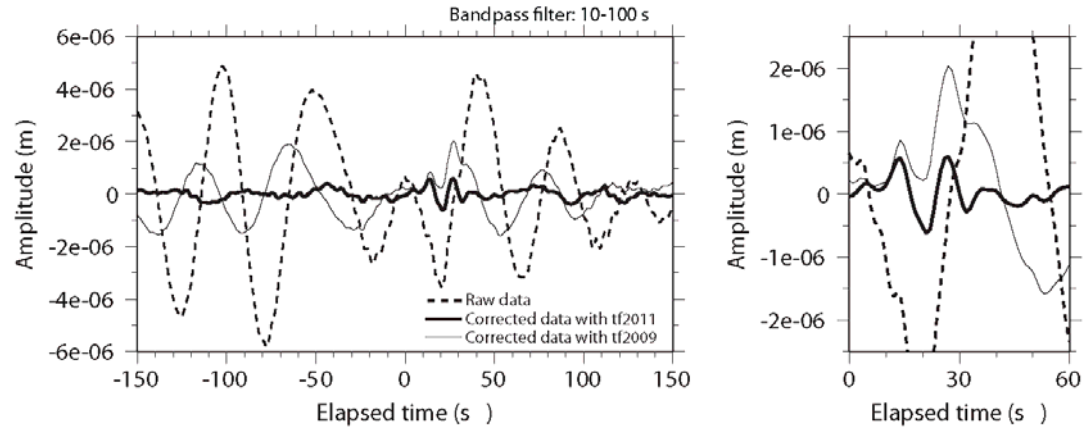

Figure 6.10. Seismic waveforms for the EV9 M_w 3.8 local earthquake. The solid trace is MOBB vertical component data after removal of the coherent DPG record by using the reference transfer function (tf2011) obtained from the 2011-2012 MOBB data. The dashed trace is the un-corrected MOBB vertical seismogram. A 10-100 s bandpass filter was applied to waveform data. Left panel shows 3-minute-long records including pre-event data and right panel shows an enlarged view of seismic phases from the local earthquake for the time interval between 0 s to 60 s from the earthquake origin time. Also shown is the corrected MOBB vertical component data (the thin line) with the reference transfer function (tf2009) obtained from the 2009-2010 MOBB data.

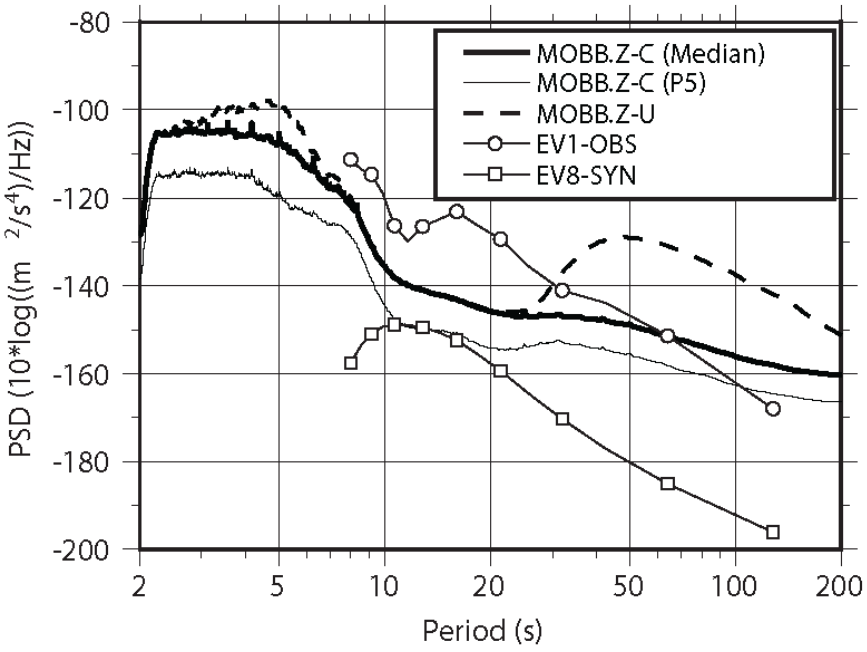

Figure 6.11. PSDs of the corrected MOBB vertical component data for the EV1 M_w 4.3 local earthquake and the synthetic MOBB data for the EV8 M_w 3.5 local earthquake. Also shown are background noise levels for the corrected (the solid line, MOBB.Z-C) and un-corrected (the dashed line, MOBB.Z-U) MOBB vertical component data. The thin line is the low noise model for the corrected MOBB vertical component data based on the lower 5th percentile (P5) inferred from the distribution of the PSDs of the corrected MOBB vertical component data.

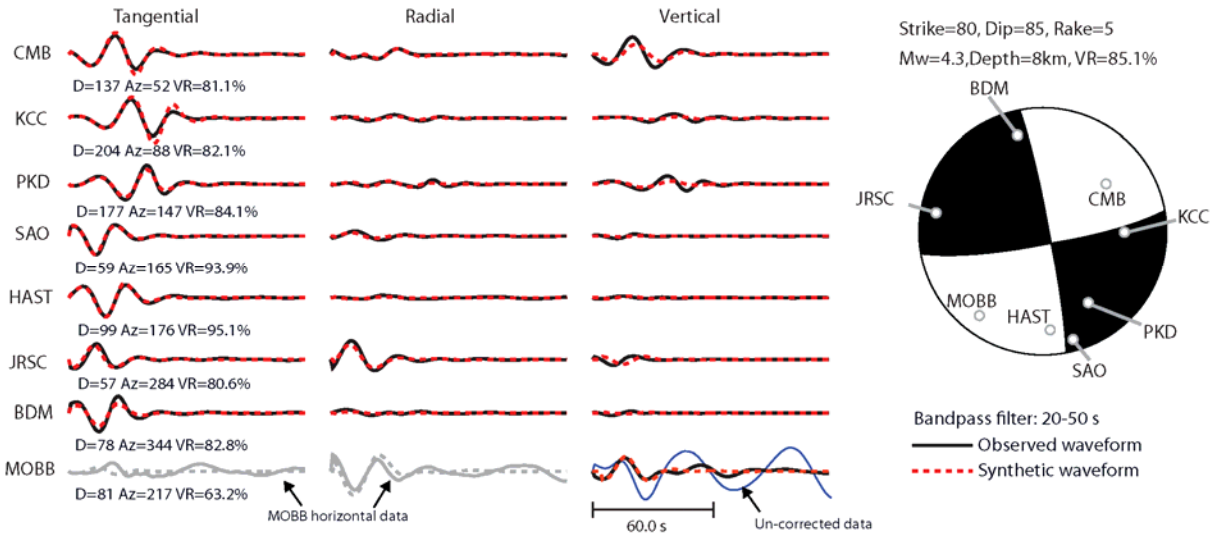

Figure 6.12. Moment tensor analysis for the EV1 M_w 4.3 local earthquake. Comparison of observed and synthetic waveforms. Also shown are earthquake-station distances (D) in km, azimuths (Az) in degrees from north, and variance reduction (VR, equation (6.5)). The VR for MOBB data is computed from the waveform fits of the vertical component data only. The un-corrected MOBB vertical component waveform is shown to illustrate the effectiveness of the noise removal method for IG-wave induced signals. Note that MOBB horizontal component data were not used for the moment tensor inversion, although they are shown in this figure.

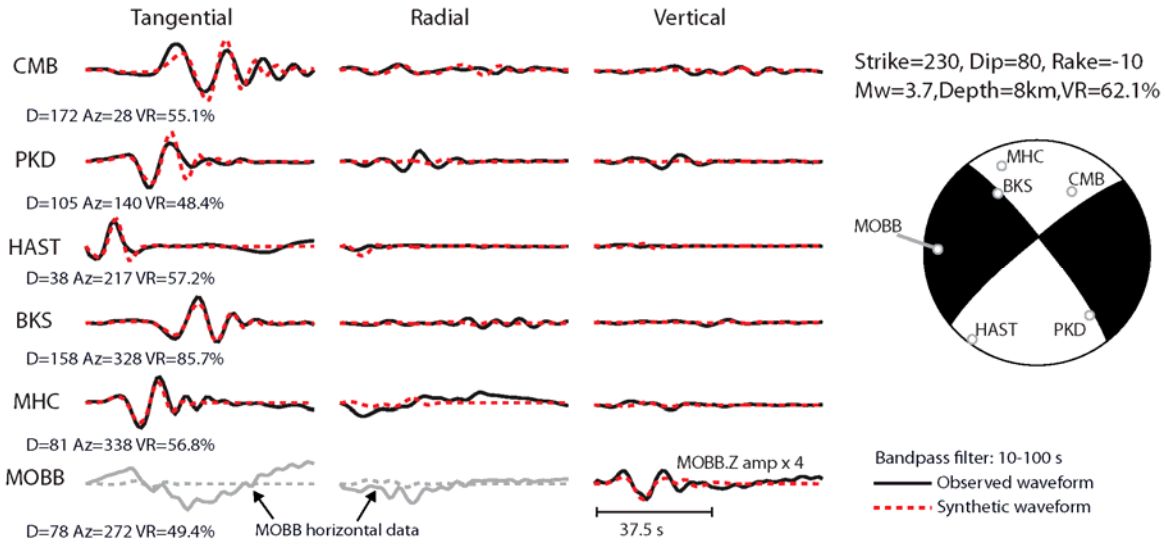

Figure 6.13. Same as Figure 6.12 except for the moment tensor analysis of the EV9 M_w 3.8 local earthquake.

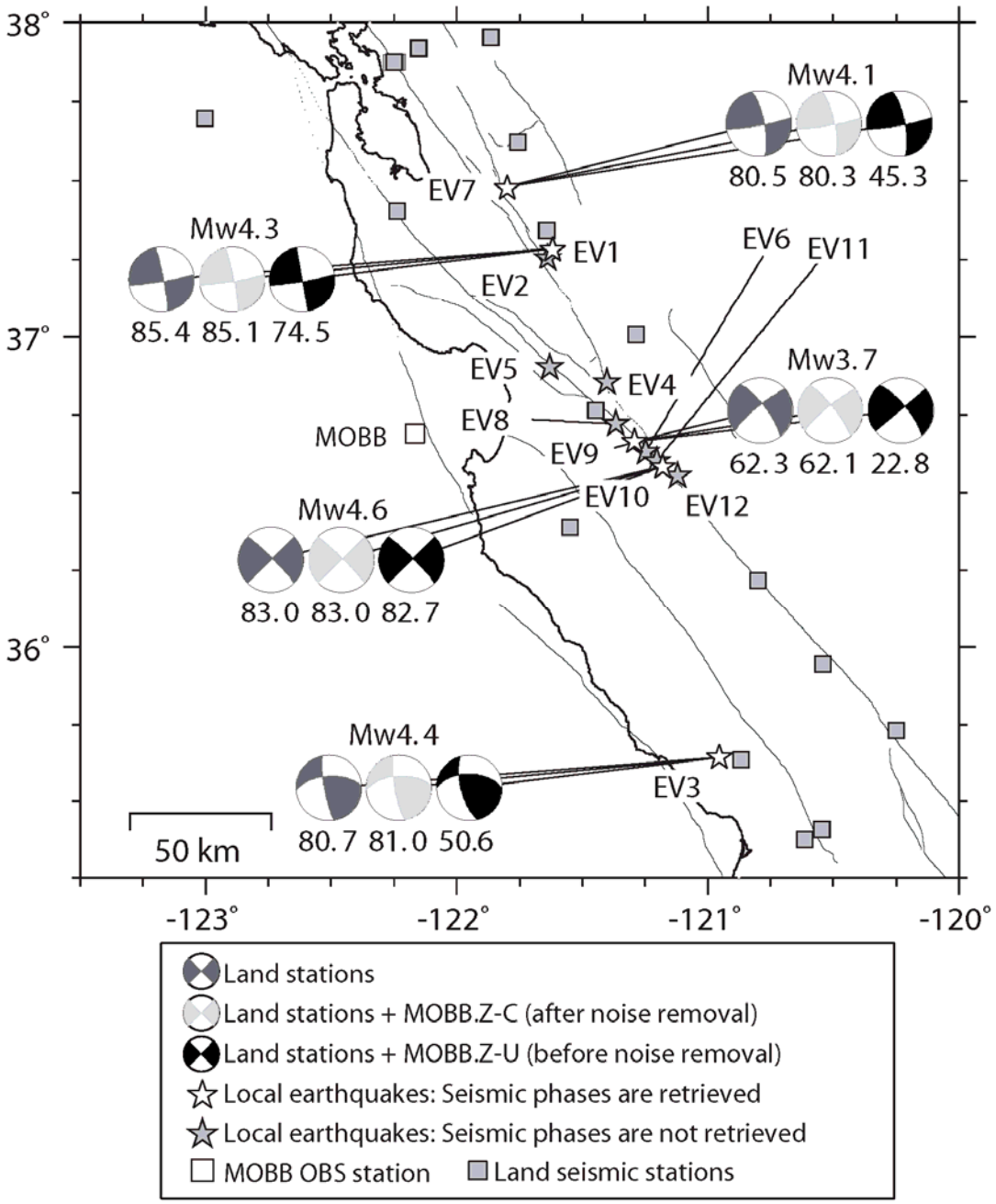

Figure 6.14. Summary plot of the moment tensor analysis for the five local earthquakes. Three moment tensor solutions are obtained for each local earthquake with different data sets. The number below each moment tensor mechanism is the total waveform VR as listed in Table 6.3.

Table 6.1. Twelve Local Earthquakes Analyzed in the Study*

Event ID	Origin Time (UTC)	Latitude	Longitude	Depth (km)	M_w	NCSS Event-ID
EV1	03/30/2009, 17:40:29.29	37.27932	-121.61906	8.0	4.3	40234037
EV2	04/30/2009, 22:50:54:82	37.25316	-121.63780	7.0	3.5	51220793
EV3	06/20/2009, 12:32:47.98	35.64212	-120.95430	6.0	4.4	40238431
EV4	09/06/2009, 09:47:15.38	36.85402	-121.40293	10.0	3.9	71271995
EV5	09/09/2009, 18:45:52.14	36.90356	-121.63114	5.0	3.6	71278336
EV6	11/01/2009, 14:55:34.21	36.63149	-121.24828	11.0	3.6	71303390
EV7	01/07/2010, 18:09:35.16	37.47645	-121.79864	11.0	4.1	71336726
EV8	02/08/2010, 19:56:23.88	36.72087	-121.36768	3.0	3.5	71350686
EV9	07/06/2011, 07:18:52.41	36.66374	-121.29158	8.0	3.8	71596420
EV10	08/27/2011, 07:18:21.25	36.58266	-121.18108	8.0	4.6	71627835
EV11	08/27/2011, 07:22:00.11	36.60092	-121.20477	7.0	3.6	71627850
EV12	04/06/2012, 03:16:20.02	36.55532	-121.12052	6.0	3.7	71759475

*Earthquake origin times and epicentral parameters from Waldhauser and Schaff (2008; see the Data and Resources section) while focal depths and seismic moment magnitudes (M_w) determined in our moment tensor analysis. Also listed are the Northern California Seismic System (NCSS) event ID.

Table 6.2. One-Dimensional Velocity, Density, and Attenuation Models for Computing Green's Function*

Thickness (km)	V_p (km/s)	V_s (km/s)	Density (kg/m^3)	Q_p	Q_s
1.0	3.20	1.50	2280	600	300
2.0	4.50	2.40	2280	600	300
1.0	4.80	2.78	2580	600	300
1.0	5.51	3.18	2580	600	300
12.0	6.21	3.40	2680	600	300
8.0	6.89	3.98	3000	600	300
-	7.83	4.52	3260	600	300

*One-dimentional seismic velocities for *P*-wave (V_p) and *S*-wave (V_s), as well as density from GIL7 model in Dreger and Romanowicz (1994). Seismic attenuation parameters for *P*-wave (Q_p) and *S*-wave (Q_s) were assumed to be 600 and 300, respectively.

Table 6.3. Variance Reduction (VR) for Double-Couple Source Model with Different Data Sets

	MOBB.Z waveform VR		Total waveform VR		
Event ID	**MOBB.Z-C**	**MOBB.Z-U**	**LAND**	**LAND+MOBB.Z-C**	**LAND+MOBB.Z-U**
EV1	63.2	9.2	85.4	85.1	74.5
EV3	87.6	-5.5	80.7	81.0	50.6
EV9	49.4	2.7	62.3	62.1	22.8
EV7	73.2	-3.5	80.5	80.3	45.3
EV10	87.3	75.5	83.0	83.0	82.7

*MOBB.Z waveform VR shows the variance reduction (VR) for the corrected (MOBB.Z-C) and un-corrected (MOBB.Z-U) MOBB vertical component data for the five local events (EV1, EV3, EV9, EV7, and EV10). Total waveform VR shows three different data sets: (1) land-station data (LAND), (2) land-station with MOBB.Z-C data (LAND+MOBB.Z-C), and (3) land-station with MOBB.Z-U data (LAND+MOBB.Z-U).

Chapter 7

Conclusions

We carry out a series of studies to refine the constraints on the seismic discontinuities (particularly the 410 and 660) and elastic structure in the Earth's upper mantle.

We propose a modification to speed up the Non-linear Asymptotic Coupling Theory (NACT), a normal mode coupling method used for synthesizing seismograms and computing sensitivity kernels in 3D Earth. The modified scheme is numerically validated. It allows NACT to meet the computational challenges when approaching higher frequencies as required for imaging finer scale heterogeneities in the Earth's upper mantle.

We present new constraints on the topography of the 410 and 660 discontinuities from a data type called the *SS* precursors. We first discuss the complexity in *SS* precursor observations cause by mantle heterogeneities. We show observations from one earthquake for which double "$S_{660}S$ precursors" are observed. In conventional notion, this would imply double 660 discontinuities in the precursor bounce point region. However, through careful 3D waveform modeling, we confirm that the double "precursors" are in fact artifacts produced by a large scale heterogeneity on the receivers' side (in particular the Rocky Mountain Front), away from the bounce point region. This new discovery challenges the above conventional notion and raises a caution for identifying and interpreting the *SS* (and perhaps *PP*) precursors in similar studies.

We then present high resolution images of 410 and 660 discontinuity topography across a large area of the Pacific Ocean, derived from a dataset of *SS* precursors recorded by the US Transportable Array. A new filtering tool called the Local Slant-Stack Filtered (LSSF) is employed to successfully remove interfering signals and random noise from the *SS* precursor record sections, leading to robust measurements of precursor travel times and discontinuity topography, with increased spatial resolution. Sensible agreements between our discontinuity images and a few fine-scale structures in the very recent mantle tomography model *SEMum2* are observed.

In the context of regional/continental scale full-waveform tomography, we propose a theoretical framework for a hybrid adjoint tomography for North America. In this hybrid framework, we solve the Gauss-Newton normal equation for model update, and the gradient of the misfit function is numerically computed using the adjoint method with the highly accurate Regional Spetral Element Method (RegSEM) code, whereas the Hessian (second derivative of the misfit function) is computed approximately using computationally fast NACT method. We present results from tests on a pre-existing North American tomography dataset, and discuss the next steps to fully implement this framework.

Finally, we investigate the infra-gravity wave induced long-period noise on an ocean bottom broadband seismometer, MOBB, deployed offshore in the Monterey Bay, California, using ~10 years' continuous recording data. Strong correlation between the vertical component seismogram and the pressure record is observed. We calculate the transfer function between the two channels, and demonstrate that the transfer function is stable over time. An average transfer function can therefore be pre-computed and stored, to allow near real-time noise removal for the MOBB data. We utilize the average transfer function to remove pressure-correlated noise from the vertical component seismogram, and show that the cleaned MOBB waveforms help to better constrain the moment tensors for near-shore seismicity on the San Andreas Fault system in Northern California.

Bibliography

Andrews J. and A. Deuss (2008), Detailed nature of the 660 km region of the mantle from global receiver function data, *J. Geophys. Res.*, **113**, B06304.

Araki, E., M. Shinohara, S. Sacks, A. Linde, T. Kanazawa, H. Shiobara, H. Mikada, and K. Suyehiro (2004), Improvement of seismic observation in the ocean by use of seafloor boreholes, *Bull. Seismol. Soc. Am.*, **94**, 678–690, doi:10.1785/0120020088.

Baba, T., K. Hirata, and Y. Kaneda (2004), Tsunami magnitudes determined from ocean-bottom pressure gauge data around Japan, *Geophys. Res. Lett.*, **31**, L08303, doi:10.1029/2003GL019397.

Bai L., Y. Zhang, and J. Ritsema (2012), An analysis of *SS* precursors using spectral-element method seismograms, *Geophys. J. Int.*, **188**, 293–300.

Barzilai, A., T. VanZandt, and T. Kenny (1998), Technique for measurement of the noise of a sensor in the presence of large background signals, *Review of Scientific Instruments*, **69**, 2767-2772.

Bassin, C., G. Lask and G. Masters (2000), The current limits of resolution for surface wave tomography in North America, *EOS, Trans. Am. Geophys. Un.*, **81**, F897.

Bécel, A., M. Laigle, J. Diaz, J.-P. Montagner, and A. Hirn (2011), Earth's free oscillations recorded by free-fall OBS ocean-bottom seismometers at the Lesser Antilles subduction zone, *Geophys. Res. Lett*., **38**, L24305.

Bendat, J. S., and A. G. Piersol (1986). *Random Data: Analysis and Measurement Procedures*, John Wiley and Sons, New York, 566 pp.

Bercovici, D. and S. Karato (2003), Whole-mantle convection and the transition-zone water filter, *Nature*, **425**, 39–44.

Bernardi, F., J. Braunmiller, U. Kradolfer, and D. Giardini (2004), Automatic regional moment tensor inversion in the European-Mediterranean region, *Geophys. J. Int.*, **157**, 703–716.

Bina, C. and G. Helffrich (1994), Phase transition Clapeyron slopes and transition zone seismic discontinuity topography, *J. Geophys. Res.*, **99**, 15853–15860.

Bohlen, T., S. Kugler, G. Klein and F. Theilen (2004), 1.5D inversion of lateral variation

of scholte-wave dispersion, *Geophysics*, **69**, 330–344.

Brandt, M. B. C., and I. Saunders (2011), New regional moment tensors in South Africa, *Seismol. Res. Lett*., **82**(1). 69–80.

Bromirski, P. D., O. V. Sergienko, and D. R. MacAyeal (2010), Transoceanic infragravity waves impacting Antarctic ice shelves, *Geophys. Res. Lett*., **37**, L02502.

Cammarano, F., B. Romanowicz, L. Stixrude, C. Lithgow-Bertelloni and W. Xu (2009), Inferring the thermochemical structure of the upper mantle from seismic data. *Geophys. J. Int.*, **179**(2), 1169-1185.

Cao, Q., P. Wang, R.D. van der Hilst, M.V. de Hoop and S.-H. Shim (2010), Imaging the upper mantle transition zone with a generalized Radon transform of *SS* precursors, *Phys. Earth Planet. Inter.*, **180**(1-2), 80–91.

Cao, Q., R.D. van der Hilst, M.V. de Hoop and S.-H. Shim (2011), Seismic Imaging of Transition Zone Discontinuities Suggests Hot Mantle West of Hawaii, *Science*, **332**, 1068–1071.

Capdeville, Y. (2005). An efficient Born normal mode method to compute sensitivity kernels and synthetic seismograms in the Earth. *Geophys. J. Int.*, **163**(2), 639-646.

Chaljub, E. and A. Tarantola (1997), Sensitivity of *SS* precursors to topography on the upper-mantle 660-km discontinuity, *Geophys. Res. Lett.*, **24**, 2613–2616.

Clinton, J. F., E. Hauksson, and K. Solanki (2006), An evaluation of the SCSN moment tensor solutions: Robustness of the M_W magnitude scale, style of faulting and automation of the method, *Bull. Seismol. Soc. Am*., **96**(5), 1689–1705.

Contenti, S., Y.J. Gu, A. Ökeler and M.D. Sacchi (2012), Shear wave reflectivity imaging of the Nazca-South America subduction zone: Stagnant slab in the mantle transition zone?, *Geophys. Res. Lett.*, **39**, L02310.

Cox, C., T. Deaton, and S. Webb (1984), A deep-sea differential pressure gauge, *J. Atmos. Oceanic Technol.,* **1**, 237-246.

Crawford, W. C., and S. C. Webb (2000), Identifying and removing tilt noise from low-frequency (<0.1 Hz) seafloor vertical seismic data, *Bull. Seismol. Soc. Am.*, **90**(4), 952–963, doi:10.1785/0119990121.

Crawford, W. C., Stephen, R. A., and Bolmer, S. T. (2006), A second look at low-frequency marine vertical seismometer data quality at the OSN-1 site off Hawaii for

seafloor, buried, and borehole emplacements, *Bull. Seismol. Soc. Am.,* **96**(5), 1952-1960.

Crotwell, H. P., T.J. Owens, and J. Ritsema (1999), The *TauP* Toolkit: Flexible seismic travel-time and ray-path utilities, *Seism. Res. Lett.*, **70**, 154–160.

Cupillard, P., E. Delavaud, G. Burgos, G. Festa, J.P. Vilotte, Y. Capdeville and J.P. Montagner (2012), RegSEM: a versatile code based on the spectral element method to compute seismic wave propagation at the regional scale. *Geophys. J. Int.*, **188**(3), 1203-1220.

Dahm, T., F. Tillmann, and J. P. Morgan (2006), Seismic broadband ocean-bottom data and noise observed with free-fall stations: Experiences from long-term deployments in the North Atlantic and the Tyrrhenian Sea, *Bull. Seismol. Soc. Am.*, **96**, 647–664, doi:10.1785/0120040064.

Deuss, A. and J.H. Woodhouse (2002), A systematic search for upper mantle discontinuities using *SS*-precursors, *Geophys. Res. Lett.* **29**, 901–904.

Deuss, A., S.A.T. Redfern, K. Chambers and J.H. Woodhouse (2006), The nature of the 660-km discontinuity in Earth's mantle from global seismic observations of *PP* precursors. *Science*, **311**, 198–201.

Deuss, A. (2009), Global observations of mantle discontinuities using *SS* and *PP* precursors, *Surv. Geophys.* **30**, 301-326.

Dolenc, D., B. Romanowicz, D. Stakes, P. McGill, and Neuhauser, D. (2005), Observations of infragravity waves at the Monterey ocean bottom broadband station (MOBB), *Geochem. Geophys. Geosyst.,* **6**, Q09002, doi:10.1029/2005GC000988.

Dolenc, D., B. Romanowicz, R. Uhrhammer, P. McGill, D. Neuhauser, and D. Stakes, (2007), Identifying and removing noise from the Monterey ocean bottom broadband seismic station (MOBB) data, *Geochem. Geophys. Geosys.,* **8**, Q02005, doi:10.1029/2006GC001403.

Dolenc, D., B. Romanowicz, P. McGill, and W. Wilcock (2008), Observations of infragravity waves at the ocean-bottom broadband seismic stations Endeavour (KEBB) and Explorer (KXBB). *Geochem. Geophys. Geosyst*., **9**, Q05007, doi:10.1029/2008GC001942.

Dreger, D., and D. Helmberger (1991), Source parameters of the Sierra Madre Earthquake from regional and local body waves, *Geophys. Res. Lett.,* **18**(11), 2015–2018, doi:10.1029/91GL02366.

Dreger, D., and B. Romanowicz (1994), Source Characteristics of Events in the San Francisco Bay Region, *USGS Open-file report* **94-176**, 301-309.

Dziewonski, A.M. and D.L. Anderson (1981), Preliminary reference Earth model, *Phys. Earth Planet. Inter.*, **25**, 297–356.

Edwards, M.O. (1989), *Global gridded elevation and bathymetry (ETOPO5) digital raster data on a 5-minute geographic (lat× lon) 2160× 4320 (centroid-registered) grid*, National Oceanic and Atmospheric Administration, Boulder, Colorado.

Fichtner, A., B.L. Kennett, H. Igel and H.P. Bunge (2009), Full seismic waveform tomography for upper-mantle structure in the Australasian region using adjoint methods. *Geophys. J. Int.*, **179**(3), 1703-1725.

Flanagan M.P. and P. Shearer (1998), Global mapping of topography on transition zone velocity discontinuities by stacking of *SS* precursors, *J. Geophys. Res.*, **103**(B2), 2673–2692.

Ford, S. R., D. S. Dreger and W. R. Walter (2010), Network sensitivity solutions for regional moment tensor inversions, *Bull. Seism. Soc. Am*., **100**, 1962-1970.

French, S., V. Lekic and B. Romanowicz (2013), Waveform tomography reveals channeled flow at the base of the oceanic asthenosphere, *Science*, **342**(6155), 227-230.

French S. (2014), *Global Full-Waveform Tomography Using the Spectral Element Method: New Constraints on the Structure of Earth's Interior*, PhD thesis, University of California, Berkeley, California.

Fukao, Y., M. Obayashi, T. Nakakuki and Deep Slab Project Group (2009), Stagnant slab: a review, *Annu. Rev. Earth Planet. Sci.*, **37**, 19–46.

Goldstein, P., and A. Snoke (2003), SAC availability for the IRIS community, DMS Electronic Newsletter, **VII**(1). http://www.iris.edu/news/newsletter/vol7no1/page1.htma

Gu, Y.J. and A.M. Dziewonski (2002), Global variability of transition zone thickness, *J. Geophys. Res.*, **107**, doi: 10.1029/2001JB000489.

Gu, Y.J., A.M. Dziewonski and G. Ekström (2003), Simultaneous inversion for mantle shear velocity and topography of transition zone discontinuities. *Geophys. J. Int.*, **154**(2), 559-583.

Gu, Y.J., A. Okeler and R. Schultz (2012), Tracking slabs beneath northwestern Pacific subduction zones, *Earth Planet. Sci. Lett.*, **331**, 269-280.

Guilhem, A., and D. S. Dreger (2011), Rapid detection and characterization of large earthquakes using quasi-finite-source Green's functions in continuous moment tensor inversion, *Geophys. Res. Lett.*, **38**, L13318, doi:10.1029/2011GL047550.

Harlan, W.S., J.F. Claerbout and F. Rocca (1984), Signal/noise separation and velocity estimation, *Geophysics*, **49**, 1869–1880.

Heit, B., X. Yuan, M. Bianchi, R. Kind and J. Gossler (2010), Study of the lithospheric and upper-mantle discontinuities beneath eastern Asia by *SS* precursors, *Geophys. J. Int.*, **183**, 252–266.

Herbers, T. H. C., S. Elgar, and R. T. Guza (1995), Generation and propagation of infragravity waves, *J. Geophys. Res.*, **100**, 24,863–24,872.

Herrmann, R. B. (2009), Computer programs in seismology, Version 3.30, http://www.eas.slu.edu/eqc/eqccps.html (last accessed January 2013).

Herzberg, C. and T. Gasparik (1991), Garnet and pyroxenes in the mantle: a test of the majorite fractionation hypothesis, *J. Geophys. Res.*, **96**, 16263–16274.

Hofmann, A.W. (1997), Mantle geochemistry: the message from oceanic volcanism, *Nature*, **385**, 219–229.

Houser, C., G. Masters, M. Flanagan and P. Shearer (2008), Determination and analysis of long-wavelength transition zone structure using *SS* precursors, *Geophys. J. Int.*, **174**, 178–194.

Houser, C. and Q. Williams (2010), Reconciling Pacific 410 and 660km discontinuity topography, transition zone shear velocity patterns, and mantle phase transitions. *Earth Planet. Sci. Lett.*, **296**(3), 255-266.

Ichinose, G. A., J. G. Anderson, K. D. Smith, and Y. Zeng, (2003), Source parameters of eastern California and western Nevada earthquakes from regional moment tensor inversion, *Bull. Seismol. Soc. Am.*, **93**, 61–84.

Ita J. and L. Stixrude (1992), Petrology, elasticity and composition of the mantle transition zone, *J. Geophys. Res.*, **97**(B5), 6849-6866.

Ito, E. and E. Takahasi (1989), Postspinel transformations in the system Mg_2SiO_4-Fe_2SiO_4 and some geophysical implications, *J. Geophys. Res.*, **94**, 10637–10646.

Ito E., M. Akaogi, L. Topor and A. Navrotsky (1990), Negative pressure-temperature slopes for reactions forming $MgSiO_3$ perovskite from calorimetry, *Science*, **249**,

1275–1278.

Ito, Y., T. Tsuji, Y. Osada, M. Kido, D. Inazu, Y. Hayashi, H. Tsushima, R. Hino, and H. Fujimoto (2011), Frontal wedge deformation near the source region of the 2011 Tohoku-Oki earthquake, *Geophys. Res. Lett.*, **38**, L00G05.

Kao, H., P. Jian, K. Ma, B. Huang, and C. Liu (1998), Moment-tensor inversion for offshore earthquakes east of Taiwan and their implications to regional collision, *Geophys. Res. Lett.,* **25**(19), 3619–3622.

Kim M.J. and J.F. Lawrence (2013), Global 3D mantle transition zone topography using finite frequency inversion of *SS* precursor travel time, *AGU Fall Meeting Abstracts*, Vol. **1**, p. 03.

Komatitsch, D. and J.P. Vilotte (1998), The spectral element method: An efficient tool to simulate the seismic response of 2D and 3D geological structures, *Bull. Seism. Soc. Am.*, **88**(2), 368-392.

Komatitsch, D. and J. Tromp (2002a), Spectral-element simulations of global seismic wave propagation—I. Validation, *Geophys. J. Int.*, **149**, 390–412.

Komatitsch, D. and J. Tromp (2002b), Spectral-element simulations of global seismic wave propagation—II. Three-dimensional models, oceans, rotation and self-gravitation, *Geophys. J. Int.*, **150**, 303–318.

Kubo, A., E. Fukuyama, H. Kawai, and K. Nonomura (2002), NIED seismic moment tensor catalogue for regional earthquakes around Japan: Quality test and application, *Tectonophysics*, **356**, 23–48, doi:10.1016/S0040-1951(02)00375-X.

Kustowski, B., G. Ekstrom and A.M. Dziewonski (2008), Anisotropic shear-wave velocity structure of the Earth's mantle: a global model, *J. Geophys. Res.*, **113**.

Laske, G., J. A. Collins, C. J. Wolfe, S. C. Solomon, R. S. Detrick, J. A. Orcutt, D. Bercovici, and E. H. Hauri (2009), Probing the Hawaiian hot spot with new Broadband Ocean Bottom instruments, *Eos Trans. AGU*, **90**(41), 362–363.

Laske G., G. Masters, Z. Ma and M. Pasyanos (2013), CRUST1.0: An updated global model of Earth's crust, *EGU General Assembly Conference Abstracts*, Vol. **14**, p.3743.

Lawrence, J.F. and P.M. Shearer (2008), Imaging mantle transition zone thickness with *SdS-SS* finite-frequency sensitivity kernels, *Geophys. J. Int.*, **174**, 143–158.

Le Stunff, Y., C.W. Wicks and B. Romanowicz (1995), P'P' precursors under Africa:

evidence for mid-mantle reflectors, *Science*, **270**, 74–77.

Lekic V. and B. Romanowicz (2011), Inferring upper-mantle structure by full waveform tomography with the spectral element method. *Geophys. J. Int.*, **185**(2), 799-831.

Li, C., R.D. van der Hilst, E.R. Engdahl and S. Burdick (2008), A new global model for P wave speed variations in Earth's mantle, *Geochem. Geophys. Geosyst.* **9**(5), doi: 10.1029/2007GC001806

Li, X.D. and T. Tanimoto (1993), Waveforms of long-period body waves in a slightly aspherical Earth model. *Geophys. J. Int.*, **112**(1), 92-102.

Li, X.D. and B. Romanowicz (1995), Comparison of global waveform inversions with and without considering cross-branch modal coupling, *Geophys. J. Int.*, **121**, 695-709.

Li, X.D. and B. Romanowicz (1996), Global mantle shear-velocity model developed using nonlinear asymptotic coupling theory, *J. Geophys. Res.*, **101**(B10), 22245-22272.

Maeda, T., T. Furumura, S. Sakai, and M. Shinohara (2011). Significant tsunami observed at the ocean-bottom pressure gauges at 2011 off the Pacific coast of Tohoku earthquake, *Earth Planets Space*, **63**, 803–808, doi:10.5047/eps.2011.06.005.

Marone, F., Y. Gung and B. Romanowicz (2007), Three-dimensional radial anisotropic structure of the North American upper mantle from inversion of surface waveform data, *Geophys. J. Int.*, **171**, 206–222.

Masson, Y., P. Cupillard, Y. Capdeville and B. Romanowicz (2014), On the numerical implementation of time-reversal mirrors for tomographic imaging, *Geophys. J. Int.*, **196**(3), 1580-1599.

Megnin, C. and B. Romanowicz (2000), The three-dimensional shear velocity structure of the mantle from the inversion of body, surface and higher-mode waveforms, *Geophys. J. Int.*, **143**(3), 709-728.

Minson, S., and D. Dreger (2008). Stable inversions for complete moment tensors, *Geophys. J. Int.*, **174**, 585– 592, doi:10.1111/j.1365-246X.2008.03797.x.

Munk, W. H. (1949), Surf beats, *Eos Trans. AGU*, **30**, 849–854.

Nettles, M. and A.M. Dziewonski (2008), Radially anisotropic shear velocity structure of the upper mantle globally and beneath North America, *J. Geophys. Res.*, **113**, B02303, doi:10.1029/2006JB004819.

Niazi, M. and D.L. Anderson (1965), Upper mantle structure of western North America from apparent velocity of P waves, *J. Geophys. Res.*, **70**, 4633–4640.

Obrebski, M., R.M. Allen, F. Pollitz and S.-H. Hung (2011), Lithosphere-asthenosphere interaction beneath the western United States from the joint inversion of body-wave traveltimes and surface-wave phase velocities, *Geophys. J. Int*., **185**, 1003-1021.

Ottolini, R. (1983), Signal/noise separation in dip space, *Stanford Exploration Project*-**37**, 143–149.

Panning, M. and B. Romanowicz (2006), A three dimensional radially anisotropic model of shear velocity in the whole mantle, *Geophys. J. Int.*, **167**, 361-379.

Pasyanos, M. E., D. S. Dreger, and B. Romanowicz (1996), Toward real-time estimation of regional moment tensors, *Bull. Seismol. Soc. Am*., **86**(5), 1255–1269.

Pasyanos, M. E. (2005), A variable resolution surface wave dispersion study of eurasia, North Africa and surrounding regions, *J. Geophys. Res.*, **110**, B12301.

Peterson, J. (1993), Observation and modeling of seismic background noise, *U.S. Geol. Surv. Tech. Rep.*, **93-322**, 95 pp.

Revenaugh J. and T.H. Jordan (1991), Mantle layering from ScS reverberations 2. The transition zone, *J. Geophys. Res.*, **96**(B12),19736–19780.

Ringwood, A.E. (1975), *Composition and petrology of the Earth's mantle*, McGraw-Hill, New York.

Ringwood, A. E. (1994), Role of the transition zone and 660 km discontinuity in mantle dynamics, *Phys. Earth Planet. Inter.*, **86**, 5–24

Ritzwoller, M. H., N. M. Shapiro, M. P. Barmin, and A. L. Levshin (2002), Global surface wave diffraction tomography, *J. Geophys. Res*., **107**(B12), 2335, doi:10.1029/2002JB001777.

Romanowicz, B., D. Dreger, M. Pasyanos, and R. Uhrhammer (1993), Monitoring of Strain Release in Central and Northern California Using Broadband Data, *Geophys. Res. Lett.*, **20**, 1643-1646.

Romanowicz, B., D. Stakes, R. Uhrhammer, P. McGill, D. Neuhauser, T. Ramirez, and D. Dolenc (2003), The MOBB experiment: A prototype permanent off-shore ocean bottom broadband station, *Eos Trans., AGU*, **84**(34), 325.

Romanowicz, B., D. Stakes, D. Dolenc, D. Neuhauser, P. McGill, R. Uhrhammer, and T.

Ramirez (2006), The Monterey Bay broadband ocean bottom seismic observatory. *Ann. Geophys.*, **49**, 607-623.

Romanowicz, B., M.P. Panning, Y. Gung and Y. Capdeville (2008), On the computation of long period seismograms in a 3-D earth using normal mode based approximations, *Geophys. J. Int.*, **175**(2), 520-536.

Romanowicz, B., P. McGill, D. Neuhauser, and D. Dolenc (2009), Acquiring real time data from the broadband ocean bottom seismic observatory at Monterey Bay (MOBB), *Seismol. Res. Lett.,* **80**(2), 197-202.

Saikia, A., D. Frost and D. Rubie (2008), Splitting of the 520-kilometer seismic discontinuity and chemical heterogeneity in the mantle, *Science*, **319**, 1515–1518.

Saito, T., T. Matsuzawa, K. Obara, and T. Baba (2010), Dispersive tsunamis of the 2010 Chile earthquake recorded by the high-sampling-rate ocean-bottom pressure gauges, *Geophys. Res. Lett.*, **37**, L23303, doi:10.1029/2010GL045290.

Saito, T., Y. Ito, D. Inazu, and R. Hino (2011), Tsunami source of the 2011 Tohoku-Oki earthquake, Japan: Inversion analysis based on dispersive tsunami simulations, *Geophys. Res. Lett.*, **38**, L00G19, doi:10.1029/2011GL049089.

Schmerr, N. and E. Garnero (2006), Investigation of upper mantle discontinuity structure beneath the central Pacific using *SS* precursors, *J. Geophys. Res.*, **111**. doi:10.1029/2005JB004,197

Schmerr, N. and E. Garnero (2007), Upper mantle discontinuity topography from thermal and chemical heterogeneity, *Science*, **318**(5850), 623–626.

Schmerr, N. and C. Thomas (2011), Subducted lithosphere beneath the Kuriles from migration of *PP* precursors, *Earth Planet. Sci. Lett.*, **311**, 101-111.

Schmerr, N. (2012), The Gutenberg discontinuity: Melt at the lithosphere-asthenosphere boundary, *Science*, **335**(6075), 1480-1483.

Schubert, G., D.L. Turcotte and P. Olsen (2001), *Mantle convection in the Earth and Planets*, Cambridge University Press, Cambridge.

Schultz, R. and Y.J. Gu (2013a), Multiresolution imaging of mantle reflectivity structure using SS and P′ P′ precursors. *Geophys. J. Int.*, **195**(1), 668-683.

Schultz, R. and Y.J. Gu (2013b), Flexible, inversion-based Matlab implementation of the Radon transform. *Computers & Geosciences*, **52**, 437-442.

Shearer, P.M. (1991), Constraints on upper mantle discontinuities from observations of long-period reflected and converted phases, *J. Geophys. Res.*, **96**, 18147-18182.

Shlivinski, A., E. Heyman and A. Boag (2005), A pulsed beam summation formulation for short pulse radiation based on windowed Radon transform (WRT) frames: *IEEE Transactions on Antennas and Propagation*, **53**, 3030–3048.

Simmons, N.A. and H. Gurrola (2000), Multiple seismic discontinuities near the base of the transition zone in the Earth's mantle, *Nature*, **405**, 559–562, doi:10.1038/35014589.

Sipkin, S. A. (1982), Estimation of earthquake source parameters by the inversion of waveform data: synthetic waveforms, *Phys. Earth Planet. Int.*, **30**(2), 242-259.

Snodgrass, F. E., G. W. Groves, K. F. Hasselmann, G. R. Miller, W. H. Munk, and W. H. Powers (1966), Propagation of ocean swell across the Pacific, *Philosophical Transactions of the Royal Society of London. Series A, Mathematical and Physical Sciences*, **259**(1103), 431-497.

Stich, D., C. J. Ammon, and J. Morales (2003), Moment tensor solutions for small and moderate earthquakes in the Ibero-Maghreb region, *J. Geophys. Res.*, **108**(B3), 2148, doi:10.1029/2002JB002057.

Sutton, G. H., W. G. McDonald, D. D. Prentiss, and S. N. Thanos (1965), Ocean-bottom seismic observatories, *Proc. IEEE*, **53**, 1909–1921.

Taira T., Z. Zheng and B. Romanowicz (2014), On the systematic long-period noise reduction on ocean floor broadband seismic sensors collocated with differential pressure gauges, *Bull. Seism. Soc. Am.*, **104**(1), doi: 10.1785/0120130015

Tajima, F., C. Megnin, D. S. Dreger, and B. Romanowicz (2002), Feasibility of real-time broadband waveform inversion for simultaneous moment tensor and centroid location determination, *Bull. Seismol. Soc. Am.*, **92**, 739–750.

Tanimoto, T. (1984), A simple derivation of the formula to calculate synthetic long-period seismograms in a heterogeneous earth by normal mode summation, *Geophys. J. Int.*, **77**, 275-278.

Tarantola, A. (1984), Inversion of seismic reflection data in the acoustic approximation, *Geophysics*, **49**, 1259-1266.

Thomas, C. and M.I. Billen (2009), Mantle transition zone structure along a profile in the SW Pacific: thermal and compositional variations, *Geophys. J. Int.*, **176**, 113–125.

Tromp, J., C. Tape and Q. Liu (2005), Seismic tomography, adjoint methods, time reversal and banana-doughnut kernels. *Geophys. J. Int.*, **160**(1), 195-216.

Tromp, J., D. Komatitsch, V. Hjörleifsdóttir, Q. Liu, H. Zhu, D. Peter, E. Bozdag, D. McRitchie, P. Friberg, C. Trabant and A. Hutko (2010), Near real-time simulations of global CMT earthquakes, *Geophys. J. Int.*, **183**, 381-389.

Tucker, M. J. (1950), Surf beats: Sea waves of 1 to 5 min. period, *Proc. R. Soc. London, Ser. A*, **202**, 565–573.

Vacher, P., A. Mocquet and C. Sotin (1998), Computations of seismic profiles from mineral physics: the importance of the non-olivine components for explaining the 660 km depth discontinuity, *Phys. Earth Planet. Inter.*, **106**, 275–298.

Van der Lee, S. and A. Frederiksen (2005), SurfaceWave Tomography applied to the North American Upper Mantle, in *Seismic Earth: Array Analysis of Broadband Seismograms*, eds G. Nolet and A. Levander, pp. 67–80, Geophysical Monograph Series 157, American Geophysical Union.

Ventosa, S., C. Simon and M. Schimmel (2012), Window length selection for optimum slowness resolution of the local-slant-stack transform. *Geophysics*, **77**(2), V31-V40.

Vinnik, L. (1997), Detection of waves converted from *P* to *SV* in the mantle. *Phys. Earth Planet. Inter.*, **15**, 39-45.

Waldhauser, F. and D. P. Schaff (2008), Large-scale relocation of two decades of Northern California seismicity using cross-correlation and double-difference methods, *J. Geophys. Res.,* **113**, B08311, doi:10.1029/2007JB005479.

Webb, S., X. Zhang, and W. Crawford (1991), Infragravity waves in the deep ocean, *J. Geophys. Res*., **96**(C2), 2723–2736, doi:10.1029/90JC02212.

Webb, S. C. (1998), Broadband seismology and noise under the ocean, *Rev. Geophys*. **36**(1), 105–142, doi:10.1029/97RG02287.

Webb, S. C., and W. C. Crawford (1999), Long period seafloor seismology and deformation under ocean waves, *Bull. Seis. Soc. Am.*, **89**, 1535-1542.

Webb, S. C., and W. C. Crawford (2010), Shallow-water broadband OBS seismology, *Bull. Seismol. Soc. Am*., **100**(4), 1770–1778, doi:10.1785/0120090203.

Weidner, D. J. and Y. Wang (1998), Chemical- and Clapeyron-induced buoyancy at the 660 km discontinuity, *J. Geophys. Res.*, **103**, 7431–7441.

Wessel, P., and W. H. F. Smith (1998), New, improved version of the Generic Mapping Tools released, *EOS Trans. AGU*, **79**, 329.

Woodhouse, J.H. and T.P. Girnius (1982), Surface waves and free oscillations in a regionalized earth model, *Geophys. J. R. Astr. Soc.*, **68**(3), 653-673.

Woodhouse, J.H. and A.M. Dziewonski (1984), Mapping the Upper Mantle: Three-Dimensional Modeling of Earth Structure by Inversion of Seismic Waveforms, *J. Geophys. Res.*, **89**(B7), 5953-5986.

Yang, Z., A. F. Sheehan, J. A. Collins, and G. Laske (2012), The character of seafloor ambient noise recorded offshore New Zealand: Results from the MOANA ocean bottom seismic experiment, *Geochem. Geophys. Geosyst*., **13**, Q10011, doi:10.1029/2012GC004201.

Yuan H. and B. Romanowicz (2010), Lithospheric layering in the North American craton, *Nature*, **466**(7310), 1063-1068.

Yuan, H., B. Romanowicz, K.M. Fischer and D. Abt (2011), 3-D shear wave radially and azimuthally anisotropic velocity model of the North American upper mantle, *Geophys. J. Int.*, **184**, 1237–1260.

Yuan H., S. French, P. Cupillard and B. Romanowicz (2013), Lithospheric expression of geological units in central and eastern North America from full waveform tomography, *Earth Planet. Sci. Lett.*, in press, http://dx.doi.org/10.1016/j.epsl.2013.11.057

Zahradník, J., and S. Custódio (2012), Moment tensor resolvability: Application to southwest Iberia. *Bull. Seism. Soc. Am.*, **102**, 1235-1254, doi: 10.1785/0120110216.

Zhao, L. and S. Chevrot (2003), *SS*-wave sensitivity to upper mantle structure: implications for the mapping of transition zone discontinuity topographies, *Geophys. Res. Lett.*, **30**(11), 1590, doi:10.1029/2003GL017223.

Zheng Z. and B. Romanowicz (2012), Do double 'SS precursors' mean double discontinuities?, *Geophysical Journal International*, **191**(3), 1361-1373.

Zhu, H., E. Bozdag, D. Peter and J. Tromp (2012), Structure of the European upper mantle revealed by adjoint tomography. *Nature Geoscience*, **5**(7), 493-498.

Zhu, H., E. Bozdag, T.S. Duffy and J. Tromp (2013), Seismic attenuation beneath Europe and the north Atlantic: implications for water in the mantle. *Earth Planet. Sci. Lett*, **381**, 1-11.